Part 1. Two Radiative Transfer Models with Terrestrial Applications

Part 2. Testing the Porcupine Plate Hypothesis

Thesis by

Marguerite F. Gerstell

In partial fulfillment of the requirements

for the degree of

Doctor of Philosophy

California Institute of Technology

Pasadena, California

1995

Submitted October 10, 1994

Acknowledgements

Some specific acknowledgements appear within each paper. The one person whose help was most critical to my finishing this thesis was Dr. Janusz Eluszkiewicz. In addition, for their direct participation in the papers of this thesis, I thank Joann Stock, Joy and David Crisp, Richard Goody and Bob West.

For general support, goodwill, and advice, I thank Yuk Yung, Andy Ingersoll, Tony Clough, Joann Stock, Costas Papaliolios, Mark Allen, Kay Campbell, Brian Farrell, and the manager of the Harvard High Energy Physics Laboratory's VAX/VMS. Special thanks to Jim Westphal for offering access to satellite maps of the Kuroshio area, even though I didn't succeed in putting them to productive use.

For the most interesting and useful of my 25 courses in science, I thank Dave Stevenson, Brian Farrell, Richard Goody, Andy Ingersoll, and Fred Abernathy. For the opportunity to teach science before I had to learn it, I thank Bill Gehring, Gene Greenwood, and Nancy Alberto.

For amusement around the office, I thank Stephen Leroy, Rich Dissly, Albert Yen, Frank Mills, Laszlo Keszthelyi, Hari Nair, and Dave Kass. What number, divided by a third of itself, equals 9?

For solvency and serenity I thank Halina Mierzejewska of Merrill Lynch, Jim Lowell, formerly of Scudder, Stevens and Clark Investment Counsel, everyone at First American Title of Pinal, Marty Zweig's newsletter, and Fed chairman Alan Greenspan.

Abstract

Paper I: Goody's convolution theorem for obtaining the cumulative k-distribution of a gas mixture requires stronger assumptions than the multiplicative property of band transmission; thus new experimental investigations of its effectiveness were undertaken. The convolution was found to be a useful speed optimization of k-distribution calculations at high pressures. For low pressures a variety of mixing methods were compared, all taking advantage of the idea that stratospheric lines are too narrow to overlap.

Appendix I discusses the context and application of k-distribution calculations.

Paper II: We used a "quasi-random" radiative transfer model to estimate stratospheric radiative perturbations produced by SO_2 gas, silicate ash, and H_2SO_4 aerosols after the 1982 El Chichon eruptions. One week after the last eruption, net radiative heating perturbations exceeding 20 K/day were modeled at altitudes near 26 km. Silicate ash heating may have been balanced by global enhancement of stratospheric meridional circulation, with upward velocities of 1 cm/s near Chichon's latitude. Radiative forcing by silicate ash and SO_2 gas should be included in more comprehensive models of plume evolution. Particle size distributions inferred from ash fallout rates could be wrong if radiative heating is neglected.

Paper III: Uncertainties in the solar spectrum can affect modeled net heating rates in the upper stratosphere by a factor of several. Variation among Antarctic surface albedo values in common use can affect modeled net heating rates in the lower stratosphere by

tens of percent. Large uncertainties in polar cloud cover are less important to stratospheric heating models. I join Marcel Nicolet in urging support for a continuous solar observation program, and recommend that future intercomparisons of stratospheric radiation models prescribe a solar spectrum, to reveal other differences.

Appendix 2 gives the details of some further validation and sensitivity tests for the quasi-random model.

Paper IV: The Porcupine Plate was postulated in 1986 to explain difficulties in reconstructing anomalies 21 and 24 in the North Atlantic. Its main feature was thought to be a transpressive Eocene plate boundary along Charlie-Gibbs Fracture Zone. Eliminating data that could have been affected by subsequent movements of Greenland relative to North America leads to a picture that casts doubt on the Porcupine Plate hypothesis.

Contents

Introduction

This thesis consists of three papers, a short note, and two appendices. The major topic is radiative transfer in the terrestrial atmosphere. This subject is obviously relevant to society's current concerns about climatic and environmental change.

Paper I develops a particular technical aspect of the "correlated-k" method of radiative transfer calculations, a method that uses the cumulative probability distributions of absorption coefficients. The paper compares various computational methods for finding the k-distributions of gas mixtures, when only the statistics of the components' spectra are known. The most successful of these devices had not been previously suggested. Appendix 1 is a more general commentary on the applicability and limitations of the correlated-k method, and recent progress by Dr. Xun Zhu, who treats part of Paper I as a resolvable paradox. I then apply correlated-k to a radiative problem suggested by Dr. Laszlo Keszthelyi, namely, the heating immediately above a lava flow.

Paper II explores the possible effects on stratospheric circulation of some short-lived products of a large volcanic eruption. This should be important to modelers of plume evolution, and the possible radiative effects of silicate ash appear so startling that they seem to invite new speculation on many of the poorly-understood aspects of volcano-climate interactions. The results are derived from Caltech's "quasi-random" radiative transfer model. A point not expressed in Paper II is that the model has been significantly debugged since the last publication based thereon. Also, my personal contribution to Paper

II lay partly in assembling a background climatology whose modernity and latitudinal extent are unusual.

Paper III is a short note exhorting the modeling community to agitate for ongoing observation of the solar spectrum, and to prescribe a solar spectrum when planning model intercomparisons. Sensitivity of polar stratospheric heating to several conditions near the earth's surface is also treated here. Appendix 2 describes a set of experiments exploring similarities and differences between outputs of the quasi-random model and various published and unpublished outputs of other models.

Prof. Yuk Yung and I have had many recent conversations about future possibilities for the correlated-k model. The last decade's experiments with such models were received first with possibly excessive optimism, later with possibly excessive pessimism. Whether the (moderate) superiority of the quasi-random model is inherent in the principle, or only in the implementation, remains uncertain. The quasi-random model stores more physical information, but the correlated-k model stores more empirical spectral information.

Paper IV has nothing to do with radiation or the atmosphere. It challenges a hypothesis that had been floating around in the literature of North Atlantic plate tectonics for about a decade. Paper IV suits my temperament because it could be summarized by the single word "no," and a single graph (Fig. 3b) speaks the "no" very plainly. The question was whether Charlie-Gibbs Fracture Zone had been a plate boundary in the late Eocene, as suggested by some investigators; the "no" for times more recent than Anomaly 21 was obtained simply by excluding data that might have been altered when Greenland was moving relative to North America.

Paper I: Obtaining the cumulative k-distribution of a gas mixture from those of its components

Abstract

The convolution theorem for obtaining the cumulative k-distribution of a gas mixture requires stronger assumptions than the multiplicative property of band transmission; thus new experimental investigations of its effectiveness are undertaken. The convolution is found to be a useful speed optimization of k-distribution calculations at high pressures. For low pressures a variety of mixing methods are compared, all taking advantage of the idea that stratospheric lines are too narrow to overlap. The optimal altitude for changing over from the convolution to one of these other methods is strongly correlated with the logarithm of the ratio of (STP) linewidth to line spacing. Some spectrally-integrated outputs of the resulting split-level method are compared with another method requiring much less computation.

1. Introduction

The correlated k-distribution technique for radiative calculations has been discussed by Lacis and Oinas (1) and by Goody, West, Chen, and Crisp (2; hereinafter, GWCC). Given a set of absorption coefficients for perhaps ten million frequencies in the thermal spectrum of the terrestrial atmosphere, one could use the correlated-k method to reduce the data by a factor of ten thousand before carrying out radiative transfer calculations.

The essential trick is to sort absorption coefficients within each narrow band. The resulting smooth monotonic function can then be represented by a few tens of points, instead of the original several hundred thousand.

A question that arises is whether a thermal or chemical change in the model atmosphere requires recalculation of the original large set of spectral absorption coefficients, before construction of the new cumulative k-distribution. Lacis and Oinas (1) suggested that a change in mixing ratios for gases with overlapping absorption bands be accommodated by fitting the k-distributions to a Malkmus model, then using the mean line strength and mean halfwidth parameters for the two separate gases to deduce a mean strength and halfwidth for the k-distribution of the mixture, also assumed to follow a Malkmus model. GWCC pointed out that the product of two Malkmus bands is not a Malkmus band, and they proposed that overlapping bands be handled by a convolution algorithm which is reviewed in Sec. 2 of the present paper. In a prototype experiment, GWCC showed that the convolution was effective for mixing water and CO_2 in the 5000-5050 cm^{-1} band, in a scattering atmosphere that extended upward to 75 mb. The present investigation grew out of an effort to turn that prototype into a production code for climate studies. Besides showing the practical strengths and weaknesses of the method, this led to some theoretical refinements.

A third way of dealing with gas mixtures in the context of k-distributions is to consider the lines of only one gas, and to augment each absorption coefficient by some constant (constant over a wide band), representing a continuum or background absorption value for the other gas. Hereinafter, I shall call this the method of principal absorbers. A principled

objection to this method is that its *a priori* selection of the principal absorber presupposes a limited range of mixing ratios, and requires a complicated specification of what that range is. But the method of principal absorbers is so much simpler than the convolution method that it is worth quantifying the difference in accuracy.

A fourth method involves using lines of both gases but assuming that no strong line of either gas coincides spectrally with any strong line of the other gas. The efficacy of this assumption at low pressures will be demonstrated.

Section 2 of the present paper includes a review of the convolution theorem proven in GWCC and a discussion of its application to natural spectra. Section 3 introduces computational optimizations for use in analyzing high-altitude gas mixtures. Section 4 shows comparisons of the results of the optimizations, and criteria for deciding what altitudes are "high" in this context. Section 5 covers a few relevant features of the testing support software. Section 6 shows some spectrally-integrated results, and examines what circumstances might permit substituting the method of principal absorbers.

2. The Convolution Theorem and its Application

(a) Derivation of the theorem

Equations (1)–(7) below follow GWCC. Consider a band bounded by frequencies ν_1 and ν_2, and the spectral absorption coefficients k_ν within the band. Let $f(k)dk$ be the fraction of these k_ν having values between k and $k+dk$. If we sort the k values in ascending order, we can construct their cumulative distribution function

$$g(k) = \int f(k')\, dk'. \tag{1}$$

One can define analogous distributions of τ_ν, the spectral optical thicknesses of the layer.

Let $F(\tau)d\tau$ denote the fraction of optical thicknesses having values between τ and $\tau + d\tau$. Here $\tau = km$, where m is the amount of absorber in the layer, requiring

$$F(\tau)d\tau = f(k)dk, \tag{2}$$

which together with $d\tau = m\ dk$, implies that

$$F(\tau) = f(k)/m. \tag{3}$$

One can define cumulative τ-distributions by

$$G(\tau) = \int_0^\tau F(\tau')d\tau'. \tag{4}$$

Consider a mixture of two gases, and append subscripts 1, 2, and 12 to denote gas 1, gas 2 and the mixture, respectively. For a particular τ_{12}, if gas 2 contributes τ_2, then gas 1 must contribute $(\tau_{12} - \tau_2)$, and τ_2 must not exceed τ_{12}. If the spectra are treated as statistically independent, we have

$$dF_{12}(\tau) = F_2(\tau_2)F_1(\tau - \tau_2)d\tau_2, \tag{5}$$

and the total distribution function would be

$$F_{12}(\tau) = \int_0^\tau F_2(\tau_2)F_1(\tau - \tau_2)d\tau_2. \tag{6}$$

We shall return in a moment to the question of statistical independence, that is, whether the probability of the coincidence is just the product of the probabilities. GWCC found computational difficulties with Eq. (6) and replaced it with the equivalent

$$G_{12}(\tau) = \int_0^{G_2(\tau - \tau_{1\min})} G_1(\tau - \tau_2)dG_2(\tau_2). \tag{7}$$

Here $\tau_{1\min}$ is the smallest optical thickness in the spectrum of gas 1; clearly $\tau - \tau_{1\min}$ is the largest value τ_2 can assume. The subscripts can be interchanged without effect. Straightforward application of Eq. (7) is convenient if the component probability distributions are given numerically; if they are instead given analytically, a pair of explicit decompositions may prove convenient: For $\tau > \tau_{1\max}$,

$$G_{12}(\tau) = G_2(\tau - \tau_{1\max}) + \int_{G_2(\tau-\tau_{1\max})}^{G_2(\tau-\tau_{1\min})} G_1(\tau - \tau_2) dG_2(\tau_2). \tag{8a}$$

For $\tau < \tau_{1\max}$,

$$G_{12}(\tau) = G_1(\tau)G_2(0) + \int_{G_2(0)}^{G_2(\tau-\tau_{1\min})} G_1(\tau - \tau_2) dG_2(\tau_2). \tag{8b}$$

(b) Example of statistically dependent spectra exhibiting the multiplication property of band transmission

The convolution theorem holds only if each τ_1 in the spectrum of gas 1 can and does spectrally coincide (somewhere in the band) with each τ_2 in the spectrum of gas 2. The probability of each such coincidence is assumed to be the product of the probability of τ_1 in spectrum 1 with the probability of τ_2 in spectrum 2. This would be true if the bands were not only random but also infinitely wide.

GWCC presented the convolution theorem as a correlated-k version of the multiplication property of band transmission. Kaplan's derivation (3) of this property involved infinite Elsasser bands with incommensurate line-spacings. Burch, Howard, and Williams (4) demonstrated that natural spectra exhibit a multiplication property for narrow bands corresponding to the slit width of a spectrometer.

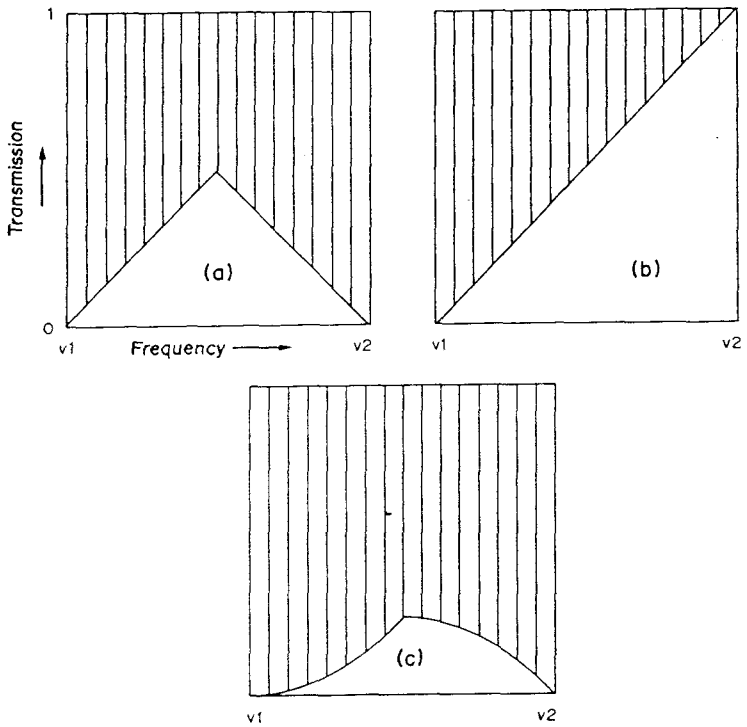

Fig. 1. Spectral multiplication of the transmissions of the imaginary gases (a) and (b) gives the transmission of the mixture (c). The unshaded area is proportional to the band transmission.

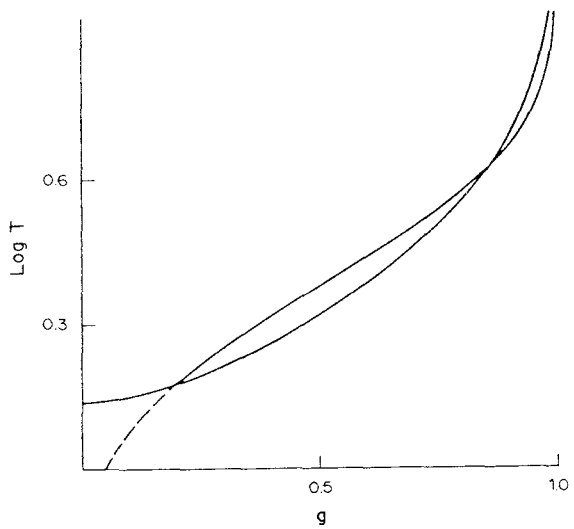

Fig. 2. The ordinate is the decimal log of transmission. The concave curve corresponds to the cumulative tau-distribution of Fig. 1(c); the inflected curve results when the mixture is approximated by convolving the tau-distributions of the components. (- - -) indicates spurious tau's that arise from the convolution but not from the mixture.

The convolution theorem would also hold for Kaplan's infinite Elsasser spectrum. But the following example demonstrates that the multiplication property does not automatically imply the convolution theorem. Consider as "spectra" the two analytic functions shown in Figs. 1(a) and 1(b). The multiplication property applies, as follows. The band transmission for gas 1 is 1/2 and, for gas 2, 1/2. The spectral optical thicknesses for the mixture are

$$\tau_{12} = 2\ \ln[(\nu_2 - \nu_1)/(\nu - \nu_1)] \text{ for } \nu \leq (\nu_1 + \nu_2)/2 \tag{9a}$$

and

$$\tau_{12} = \ln[(\nu_2 - \nu_1)^2/(\nu - \nu_1)(\nu_2 - \nu)] \text{ for } \nu \geq (\nu_1 + \nu_2)/2, \tag{9b}$$

so the band transmission for the mixture is

$$\int_0^{1/2} x^2 dx \ + \ \int_{1/2}^{1} (x - x^2) dx = 1/8. \tag{10}$$

Here x denotes $(\nu - \nu_1)/(\nu_2 - \nu_1)$. Since 1/2 x 1/4 = 1/8, the multiplication property is satisfied.

But the convolution theorem fails, as follows. The cumulative distribution functions for the two separate gases are

$$G_1(\tau) = 1 - 2\mathrm{e}^{-\tau}, \tag{11}$$

$$G_2(\tau) = 1 - \mathrm{e}^{-\tau}, \tag{12}$$

and for the mixture formed by spectral addition of optical thicknesses, we have

$$G_{12}(\tau) = 0.5[1 + (1 - 4\mathrm{e}^{-\tau})^{1/2}] - \mathrm{e}^{-\tau/2}. \tag{13}$$

Calculating the convolution from Eqs. (7), (11) and (12) yields

$$G_{12}(\tau) = 1 - 2\mathrm{e}^{-\tau}(\tau + 1 - \ln 2). \tag{14}$$

The two cumulative τ-distributions in Eqs. (13) and (14) are shown in Fig. 2. At $G = 1$, both τ's go to infinity, but the error is considerable as τ shrinks. The dashed line indicates τ_{12} values in the convolved distribution that do not exist in the real distribution. This occurs because minimum τ_i values for the two gases do not spectrally coincide anywhere in the band.

An obvious peculiarity of the example is that the linear correlation coefficient (5) in each half of the band has absolute value unity, while the same coefficient for the whole band is zero. Although Ref. 3 does not note it, the multiplicative property of band transmission is exactly equivalent to a band-wide linear correlation of zero, a much less restrictive condition than statistical independence. Natural spectra always have non-zero piecewise correlations, but we shall see in the next subsection that the condition of statistical independence is often met well enough for heating-rate calculations.

(c) Criteria for band selection

Figure 3 exhibits thermal cooling or solar heating rates calculated by the correlated-k technique, from the atmosphere in Table 1, which is derived from a mid-latitude summer model of Ridgway (6). Figure 3 was constructed by sorting the spectral absorption coefficients of the mixed gas.

Table 1. Model atmosphere: number of molecules per square centimeter for each layer and species. N(BROAD) denotes number of non-absorbing molecules contributing to pressure-broadening.

p (mb)	T (K)	z (km)	N(H_2O)	N(CO_2)	N(O_3)	N(N_2O)	N(CH_4)	N(O_2)	N (BROAD)
1001.1	293.59	0.20	9.137E21	1.667E20	1.539E16	1.616E17	8.585E17	1.055E23	3.902E23
977.33	292.76	0.41	8.602E21	1.671E20	1.578E16	1.620E17	8.609E17	1.058E23	3.918E23
953.56	291.91	0.63	8.095E21	1.678E20	1.618E16	1.627E17	8.643E17	1.063E23	3.939E23
929.78	291.03	0.85	7.614E21	1.686E20	1.660E16	1.635E17	8.686E17	1.068E23	3.964E23
906.03	290.12	1.07	7.091E21	1.682E20	1.693E16	1.631E17	8.663E17	1.065E23	3.958E23
882.23	289.14	1.30	6.526E21	1.675E20	1.727E16	1.625E17	8.630E17	1.061E23	3.949E23
858.46	288.07	1.54	6.009E21	1.678E20	1.771E16	1.627E17	8.643E17	1.063E23	3.960E23
834.68	286.86	1.78	5.546E21	1.688E20	1.825E16	1.637E17	8.698E17	1.069E23	3.990E23
810.96	285.53	2.03	5.059E21	1.683E20	1.866E16	1.632E17	8.671E17	1.066E23	3.982E23
787.13	284.10	2.28	4.460E21	1.642E20	1.876E16	1.592E17	8.456E17	1.040E23	3.888E23
763.35	282.59	2.53	4.021E21	1.651E20	1.951E16	1.601E17	8.505E17	1.046E23	3.915E23
739.58	281.03	2.80	3.606E21	1.657E20	2.028E16	1.607E17	8.538E17	1.050E23	3.935E23
715.82	279.42	3.07	3.221E21	1.664E20	2.110E16	1.614E17	8.573E17	1.054E23	3.955E23
692.03	277.76	3.35	2.831E21	1.668E20	2.194E16	1.617E17	8.589E17	1.056E23	3.968E23
668.25	276.05	3.64	2.475E21	1.677E20	2.291E16	1.626E17	8.632E17	1.062E23	3.993E23
644.47	274.29	3.94	2.152E21	1.685E20	2.394E16	1.634E17	8.670E17	1.067E23	4.016E23
620.74	272.48	4.25	1.829E21	1.671E20	2.472E16	1.621E17	8.589E17	1.058E23	3.986E23
596.92	270.61	4.57	1.547E21	1.672E20	2.580E16	1.622E17	8.579E17	1.059E23	3.991E23
573.15	268.67	4.90	1.309E21	1.687E20	2.718E16	1.636E17	8.638E17	1.068E23	4.029E23
549.44	266.66	5.23	1.092E21	1.665E20	2.810E16	1.615E17	8.508E17	1.055E23	3.979E23
525.60	264.58	5.59	9.541E20	1.666E20	2.959E16	1.615E17	8.485E17	1.055E23	3.981E23
501.82	262.40	5.95	8.379E20	1.679E20	3.149E16	1.628E17	8.526E17	1.064E23	4.015E23
478.09	260.12	6.33	7.095E20	1.640E20	3.271E16	1.590E17	8.291E17	1.038E23	3.921E23
454.27	257.70	6.72	6.152E20	1.647E20	3.535E16	1.597E17	8.285E17	1.043E23	3.940E23
430.52	255.15	7.13	5.299E20	1.657E20	3.840E16	1.607E17	8.291E17	1.050E23	3.966E23
406.72	252.44	7.56	4.411E20	1.660E20	4.128E16	1.609E17	8.260E17	1.051E23	3.972E23
382.95	249.57	8.02	3.643E20	1.679E20	4.488E16	1.626E17	8.311E17	1.064E23	4.020E23
359.16	246.54	8.50	2.918E20	1.669E20	4.856E16	1.612E17	8.222E17	1.057E23	3.996E23
335.39	243.33	9.01	2.346E20	1.689E20	5.416E16	1.623E17	8.282E17	1.069E23	4.043E23
311.61	239.94	9.55	1.799E20	1.664E20	5.856E16	1.585E17	8.092E17	1.054E23	3.984E23
287.87	236.32	10.12	1.376E20	1.681E20	6.481E16	1.582E17	8.073E17	1.064E23	4.025E23
264.05	232.45	10.74	8.548E19	1.683E20	7.638E16	1.555E17	7.969E17	1.066E23	4.030E23
240.38	228.29	11.41	4.561E19	1.675E20	9.210E16	1.516E17	7.814E17	1.061E23	4.012E23
216.55	223.79	12.14	2.178E19	1.677E20	1.079E17	1.498E17	7.703E17	1.062E23	4.017E23
192.76	219.16	12.93	8.942E18	1.678E20	1.319E17	1.472E17	7.587E17	1.062E23	4.019E23
169.04	216.24	13.83	3.900E18	1.682E20	1.792E17	1.446E17	7.486E17	1.065E23	4.030E23
145.29	215.77	14.84	3.191E18	1.628E20	2.264E17	1.369E17	7.110E17	1.031E23	3.899E23
121.39	215.75	16.08	3.239E18	1.662E20	2.738E17	1.346E17	7.091E17	1.053E23	3.983E23
97.691	215.77	17.65	3.286E18	1.686E20	3.595E17	1.248E17	6.957E17	1.068E23	4.040E23
73.889	216.66	19.74	3.268E18	1.677E20	6.658E17	1.000E17	6.576E17	1.062E23	4.018E23
53.115	219.10	21.93	2.439E18	1.252E20	8.779E17	5.323E16	4.424E17	7.927E22	2.999E23
37.901	221.75	24.14	1.740E18	8.930E19	9.214E17	2.835E16	2.639E17	5.656E22	2.140E23
26.988	224.60	26.40	1.248E18	6.404E19	9.357E17	1.732E16	1.536E17	4.056E22	1.534E23
19.237	228.70	28.69	8.860E17	4.546E19	8.197E17	1.097E16	9.725E16	2.879E22	1.089E23
13.697	233.75	31.04	6.362E17	3.264E19	6.837E17	6.672E15	6.301E16	2.067E22	7.821E22
9.7894	238.96	33.44	4.550E17	2.335E19	5.605E17	3.666E15	4.026E16	1.479E22	5.594E22
6.9648	244.32	35.86	3.181E17	1.632E19	4.307E17	1.920E15	2.524E16	1.034E22	3.911E22
4.9686	250.12	38.37	2.297E17	1.179E19	3.102E17	9.725E14	1.626E16	7.465E21	2.824E22
3.5420	256.44	40.94	1.639E17	8.412E18	1.962E17	4.736E14	1.020E16	5.328E21	2.015E22
2.5247	262.94	43.59	1.172E17	6.013E18	1.110E17	2.237E14	6.286E15	3.808E21	1.441E22

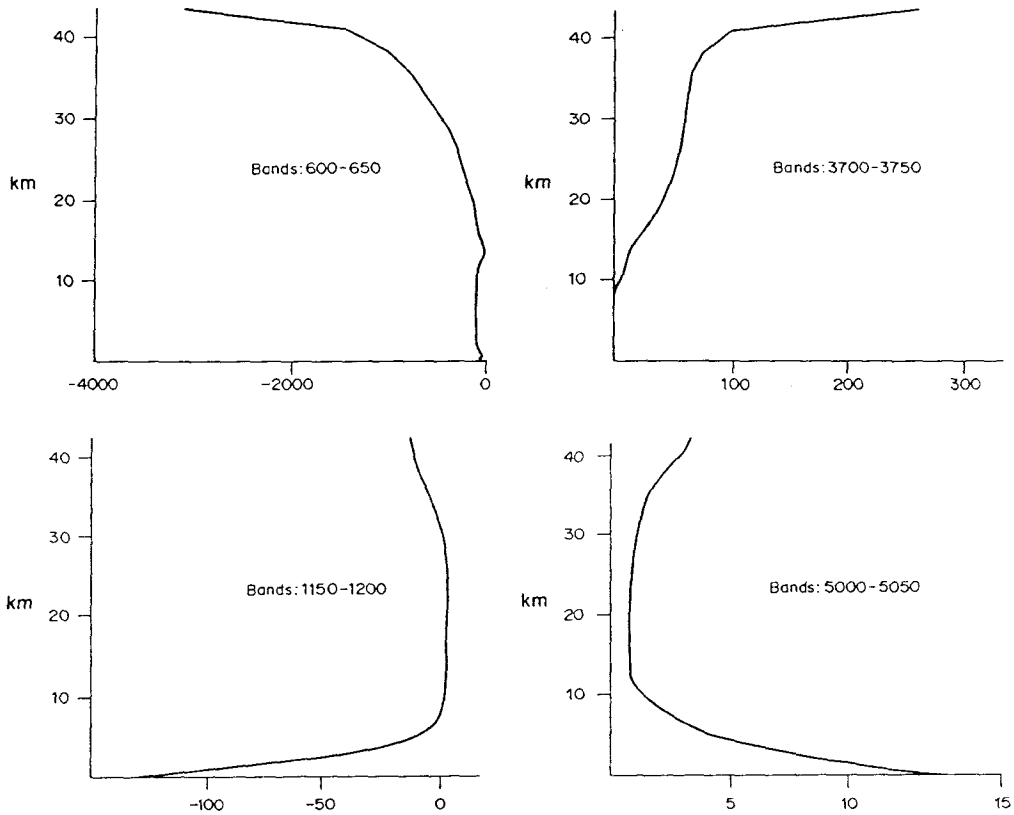

Fig. 3. Thermal cooling (for the 600–650 and 1150–1200 wavenumber bands) or solar heating (for the 3700–3750 and 5000–5050 wavenumber bands) was calculated from the cumulative k-distribution of the gas mixture in Table 1. The horizontal scale is mK/day.

Among the criteria for selecting these bands was that they should not respond well to the method of principal absorbers, given the plausible humidities of Table 1. Figure 4 exhibits the relative errors introduced by the method of principal absorbers, in the heating rates of Fig. 3. In two of these bands (600-650 and 3700-3750 cm^{-1}), the optical thicknesses of the dry part of the gas mixture were augmented by a constant representing the median absorption of the water. In the other two (1150-1200 and 5000-5050 cm^{-1}), water was treated as the principal absorber at pressures higher than 300 mb, and its optical thicknesses augmented by a constant representing the median absorption of the dry gas; while the dry gas mixture was treated as the principal absorber at pressures less than 300 mb. In an experiment not shown, I found that using water as a principal absorber all the way up the column in the 1150-1200 and 5000-5050 cm^{-1} bands gives O(1) error in the stratospheric heating rates.

A second consideration in selecting the bands for further examination was that they should fairly represent the range of response to the methods of the present paper, which often proved useful but occasionally did not.

A third consideration in selecting bands was that 5000-5050 cm^{-1} was the band used in the GWCC prototype experiment, and that 600-650 cm^{-1} is a band under extensive study by other investigators. GWCC explains why the spectral characteristics of the 5000-5050 cm^{-1} band should provide a strong test case for the convolution.

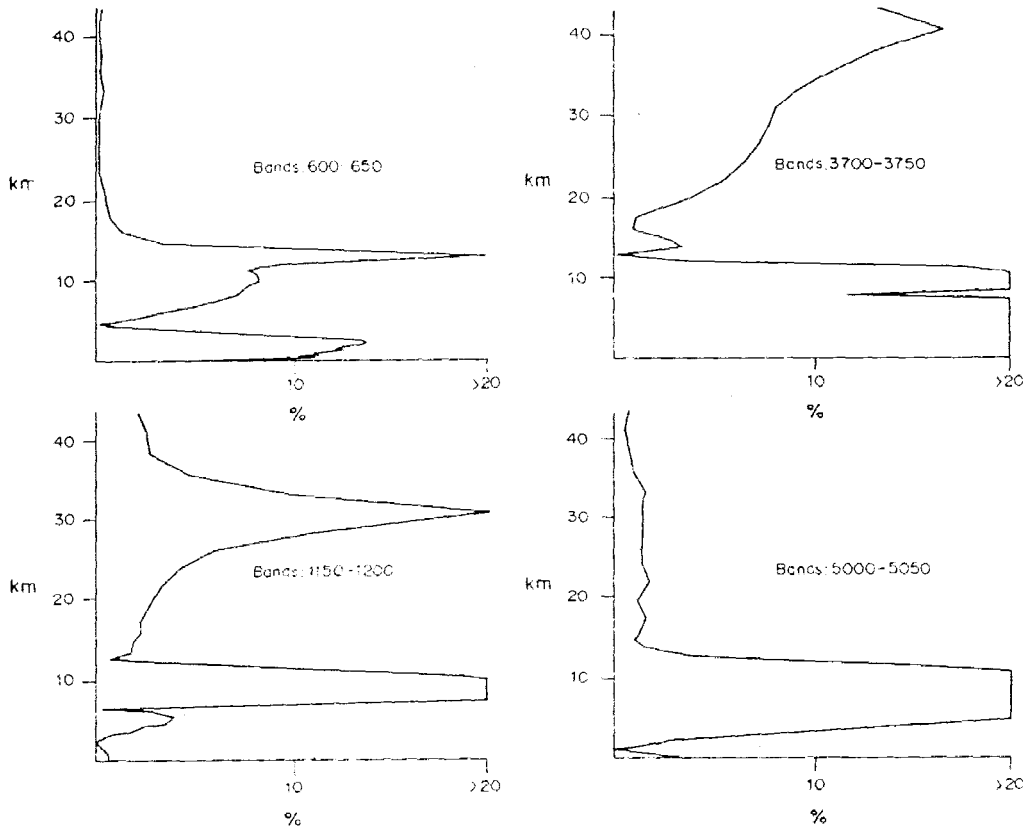

Fig. 4. When the method of principal absorbers is used to find the heating rates of Fig. 3, it introduces relative errors whose absolute value is the abscissa here. For the top two panels, the principal absorber was the dry gas that would result if water were deleted from Table 1. For the bottom two panels, the principal absorber from 300 to 1000 mbar was water, and from 1 to 300 mbar, the aforementioned dry gas.

(d) Application of the convolution to natural spectra

Figure 5 shows the relative error in the heating rates, arising from the convolution. Here the spectral absorption coefficients of the dry part of the mixture are sorted, separately from those of the water vapor. The two cumulative k-distributions are convolved, and heating rates calculated from the resulting k-distribution. Errors are relative to Fig. 3. The convolution works well, if we use a large enough number of points of $G_1(\tau)$ and $G_2(\tau)$ in performing the integration of Eq. (7). Figure 5 compares the error introduced by the GWCC convolution, when 1000 Gaussian quadrature points are stored initially, against the error introduced when 100 Gaussian quadrature points are used in Eq. (7). In the curves marked "n=1000", the median error for all layers in all panels is 1.25%, even including the layers where the heating nearly vanished. But in the initial implementation, these 1000-point convolutions took far longer than repeating the line-by-line calculation of the k-distribution of the mixture. Thus, their execution would be useless unless further optimized. The 100-point convolutions were, on average, ten times faster than the line-by-line recalculation of the k-distribution of the mixture; but the high-altitude errors are unacceptable.

It should be emphasized at this point that the 1000-point curves in Fig. 5 demonstrate that even for these fairly narrow bands, statistical independence of two component spectra is a reasonable assumption for radiative transfer calculations. We shall see that large errors in the convolved distributions are typically confined to the upper extremity of the distribution, and that this will cause trouble only if the peak optical thicknesses of the two components are comparable in the uppermost layers of the model atmosphere.

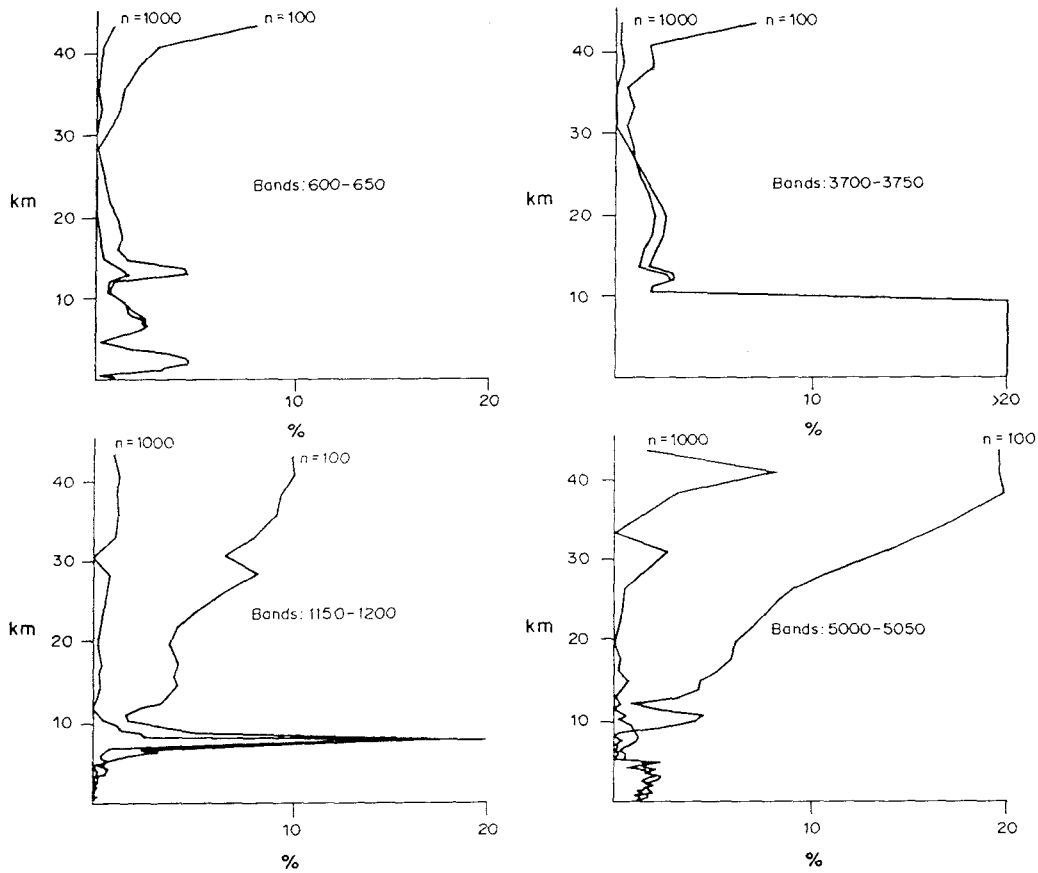

Fig. 5. When the GWCC convolution is used to find the heating rates of Fig. 3, it introduces relative errors whose absolute value is the abscissa here. The "n" is the number of points of the components' tau-distributions that were used in integrating Eq. (7).

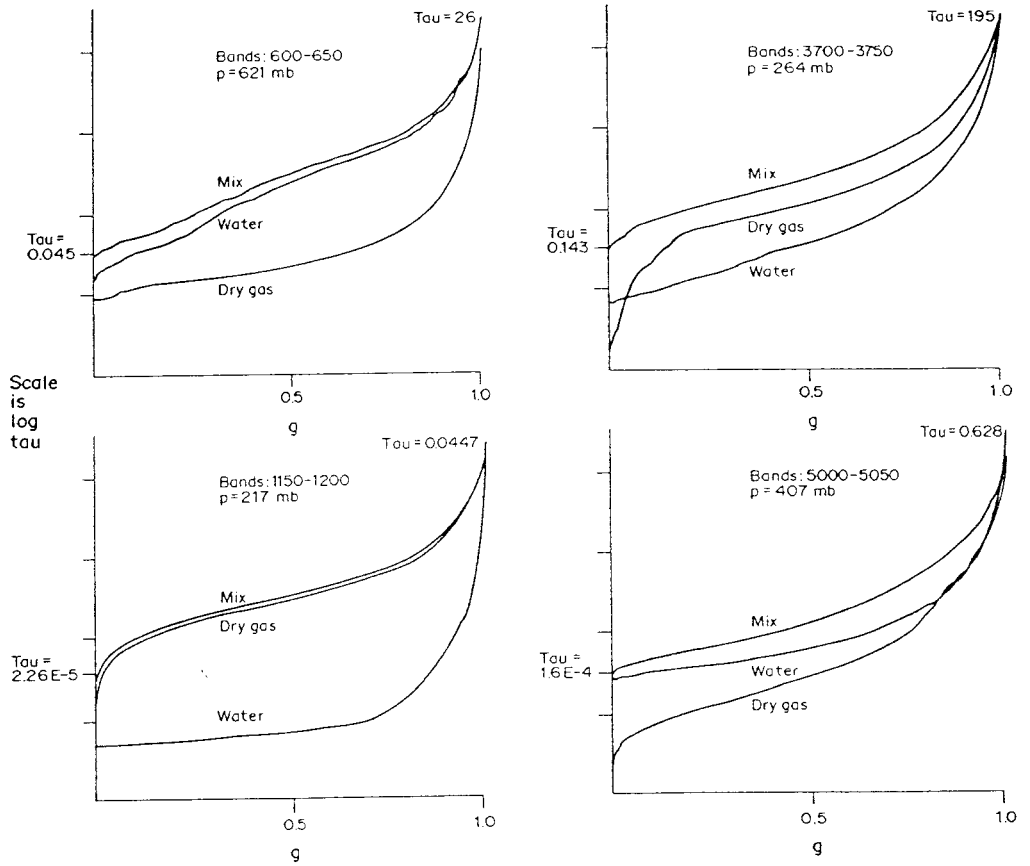

Fig. 6. These tau-distributions arise from Table 1, for water, dry gas, and the spectrally-mixed gas (not the convolution). The indicated pressure levels were chosen so that the optical thickness of the strongest water lines would be comparable to that of the strongest dry-gas lines.

There are two reasons why the sparse convolution works better near the ground than at high altitudes. One is that pressure-broadening prevents the strongest lines from being missed, or grossly misshapen, by the coarse resolution of the $\tau(G)$ function. A second is that the heating and cooling of the lowest atmospheric layers is affected by a relatively wide fraction of the cumulative distribution of spectral optical thicknesses, while the narrow-band heating and cooling of a stratospheric layer are typically dominated by the few largest τ's in the band. Since these few largest τ's are among the ones that the sparse convolution is most likely to get wrong, heating and cooling rates at higher altitudes can be wrong even when a sparse convolution has done a good job over much of the range of τ.

Figures 6, 7, and 8 support these explanations for the success of the sparse convolution at low altitudes. Figure 6 shows the $\tau(G)$ functions for water, dry gas, and the mixture (not the convolution). For each band, the layer shown is a tropospheric layer in which the peak absorption by water vapor is comparable in magnitude to the peak dry-gas absorption, after applying the concentrations of Table 1. Figure 7 shows that the relative error in the $\tau_{12}(G)$ functions for sparsely-convolved pairs of real spectra may be only a few percent for most τ's in the range, but then rises to between 25% and 78% near G=1, where the few strongest, narrow lines are incorrectly treated by the convolution. This is not just a matter of insufficient numerical resolution. The 1000-point convolutions show errors nearly as large, at G=1. For instance, the 78% becomes 75%. All the errors at G=1 are positive, showing that the convolution assumed some probability that the maxima of the two spectra would coincide...while in a finite band they really do not coincide. But at the altitudes shown here, the heating or cooling is not controlled by $\tau_{\max}$, so this intrinsic

weakness of the convolution turns out to be unimportant for practical purposes.

To understand the error spikes in Fig. 7 more clearly, consider a band of width 1, and suppose that for each of the two gases, this band contains exactly one triangular line of basewidth $\epsilon \ll 1$ and a peak optical thickness of 1. Assume there no absorption outside the triangles. If the relative position of the two lines is random, the expected value of $\tau_{\max}$ for the gas mixture is $1 + \epsilon/2$. But the convolution always predicts the maximum spectral absorption of the mixture to be the sum of the component maxima, in this case 2. More generally, the error in the convolved distribution in the neighborhood of $\tau_{\max}$ will approach

$$\frac{\Delta(\tau_{\max})}{\tau_{\max}} = \frac{\min(\tau_{1\max}, \tau_{2\max})}{\max(\tau_{1\max}, \tau_{2\max})} \tag{15}$$

whenever strong lines are few and narrow. Comparing Figs. 6 and 7 shows that this crude estimate has the right order of magnitude for the natural spectral bands of width 50 cm^{-1} that are considered here. The peak error in the 3700-3750 cm^{-1} panel is greatest because the component maxima are most nearly equal. Most of the panels do not show peaks on the left because natural spectra at low pressures consist of narrow peaks against a diffuse background. The large error at the optically-thin end of the 3700-3750 cm^{-1} panel may be due to a random anticorrelation: the smallest 5% of the dry-gas spectral absorptions all occur quite near the blue end of the band, while the smallest of the spectral absorptions for water all occur nearer the red end of the band.

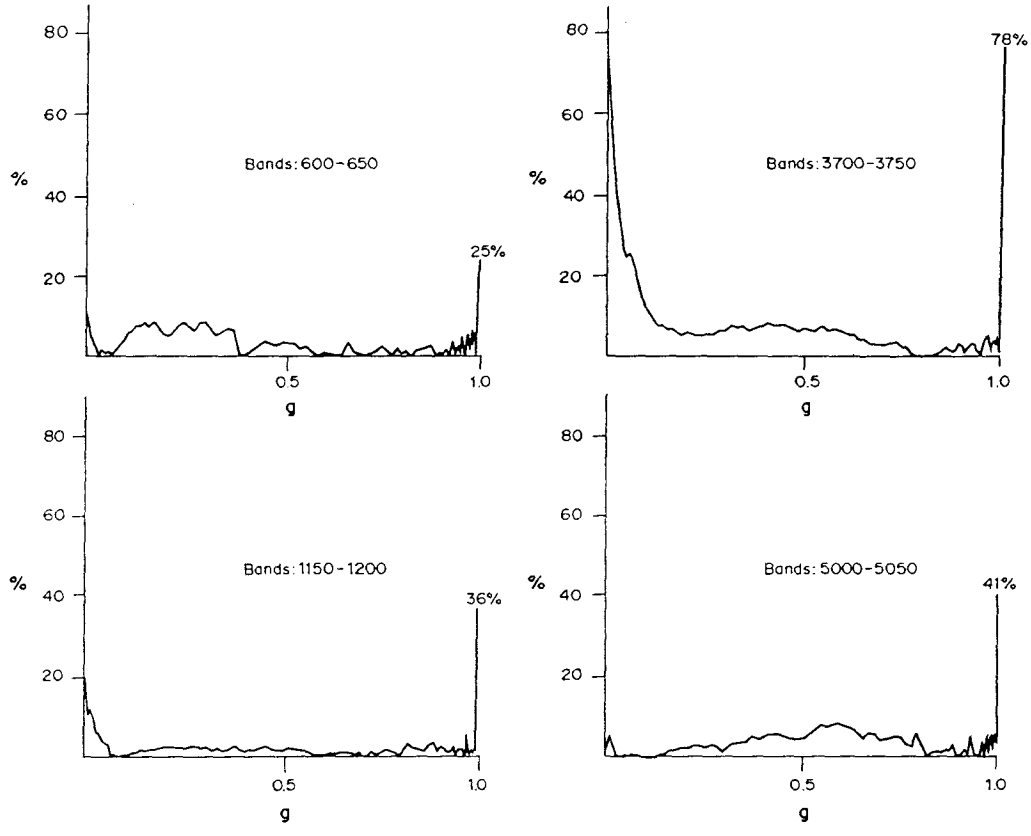

Fig. 7. When 100 Gaussian-quadrature points are used to integrate Eq. (7), the tau-distribution of the mixture exhibits relative errors whose absolute value is the ordinate here. The pressure levels were chosen as in Fig. 6.

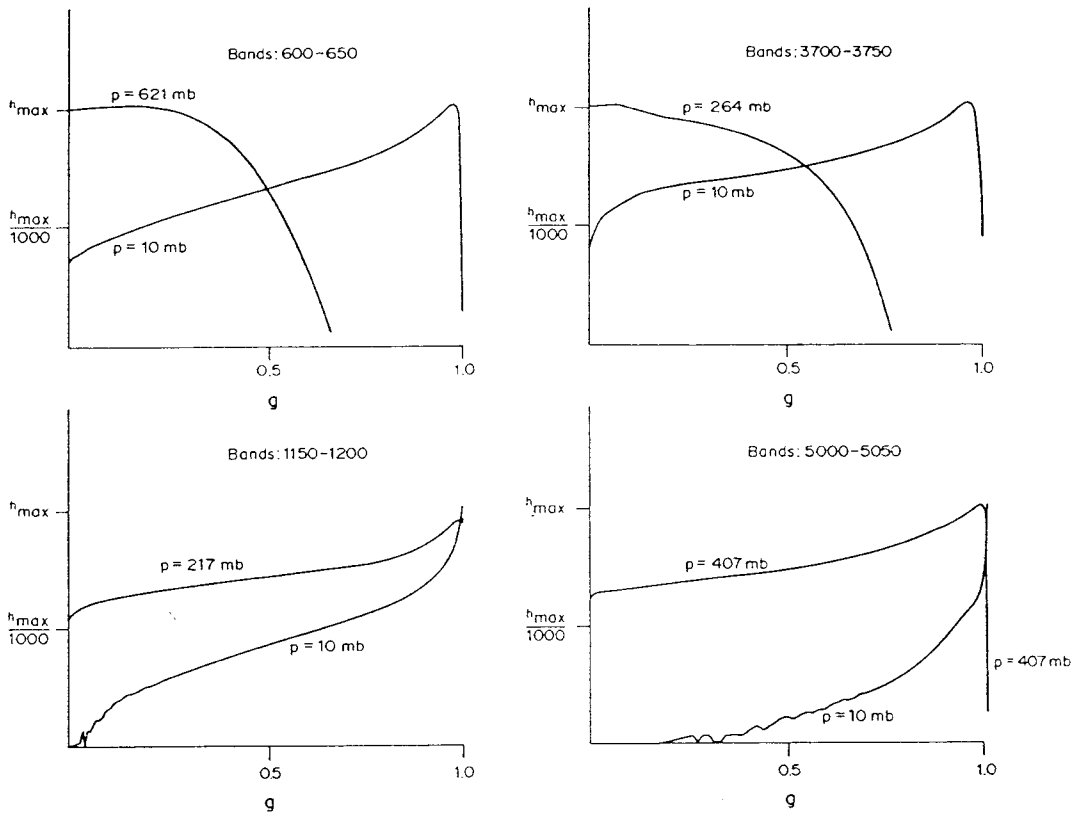

Fig. 8. Heating and cooling rates can be calculated as if the tau-distribution were a spectrum of optical thicknesses. In that sense, this figure displays "spectral" heating or cooling rates. A high peak on the right means most heating is due to the few largest tau's. The two curves in each panel do not have the same peak value; in each case, one has been translated upward so the shapes can be compared.

Figure 8 then shows that the heating or cooling of the gas mixture from Figs. 6 and 7 is due mainly to the few largest τ in each band, at high altitudes. For the layers of Figs. 6 and 7, two of the four bands have maximum heating or cooling near $G = 0$; the other two have fairly flat distributions of the heating across the domain of G. But for the 10 mb layer (near 32 km), the peaks of the heating or cooling curves have shifted dramatically toward the high end of the τ-distribution. This remains true even for the 600-650 and 3700-3750 cm^{-1} bands, where τ_{max} absorbs so much that the wings become the main absorbers in the middle layers. For the 3700-3750 cm^{-1} band, we see the sparse convolution working reasonably well in the 15-40 km strata, because for this band, τ_{max} does not control the heating rates even in the upper stratosphere.

Figure 9 shows how the 1000-point resolution removes some of the error at high altitudes. For the 10-mb layer, Fig. 9 shows errors in the large τ's, arising from the sparse and dense convolutions, which now give distinctly different results. At these altitudes, the sparse convolution does not give the spurious spike at the very largest τ, because the optical thickness of the water is much less than that of the dry gas, so that the sum of the two spectral maxima is not very different from the maximum of the dry-gas absorption alone. But the sparse convolution does give large errors in τ, spread over a larger number of the high G's, since the lines are narrower at low pressures, and are not well resolved by the sparse data. This computational problem implies nothing about the theoretical properties of the convolution. The computational problem could perhaps be reduced by a more judicious selection of the points for the numerical integration; in Sec. 3 a more radical simplification is suggested.

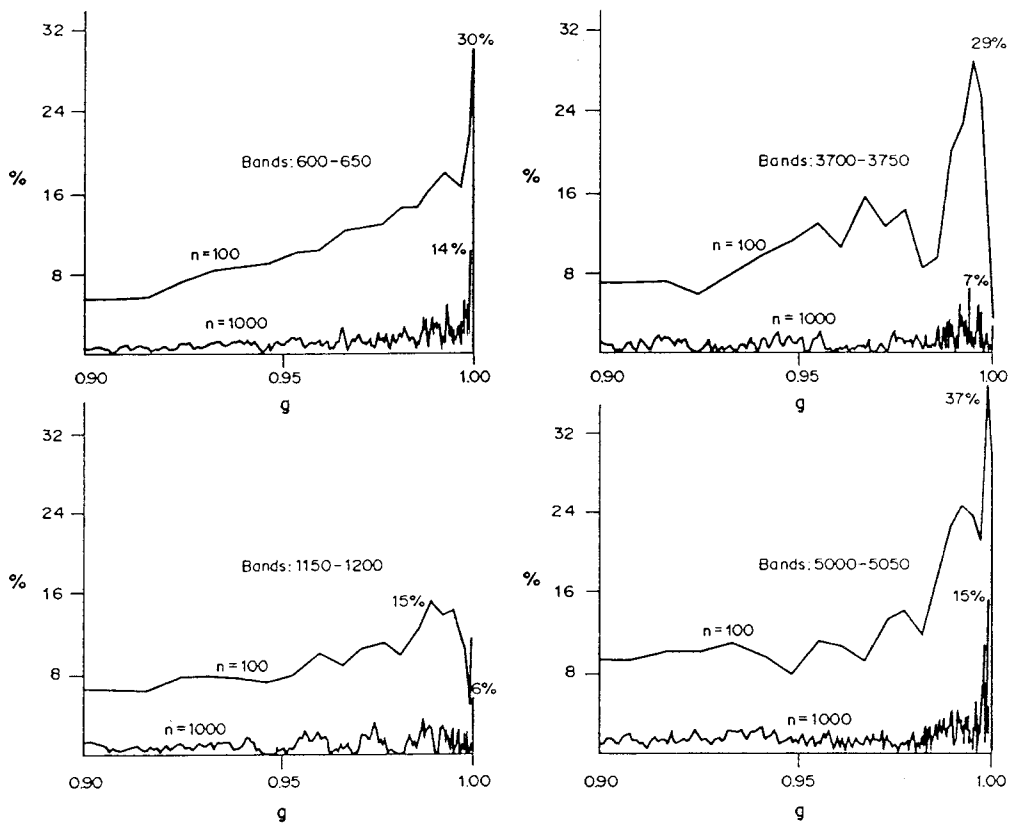

Fig. 9. When the GWCC convolution is used to obtain the tau-distribution of the mixture, it introduces relative errors (in tau) whose absolute value is the ordinate here. The "n" is the number of points of the components' tau-distributions that were used in integrating Eq. (7).

3. Simplifications for the Low-Pressure Regime

If only the few largest τ are important in the high-altitude layers, then a very simple optimization comes to mind. One could assume that each of the two spectra is dominated by a few narrow lines, and that the probabilistic overlap calculated by the convolution can be reasonably replaced by no overlap at all. Indeed, the spikes at $G = 1$ in Fig. 6 are all positive errors, and all attest to the manner in which the convolution overestimates the maximum τ_{12}. Several different implementations of a no-overlap assumption are possible, depending on whether the line-by-line program that generates the component $\tau_i(G)$ distributions can conveniently deliver spectral absorption coefficients for line cores separately from those for the far wings, or any other absorption behaving like a continuum.

As a first case, let us assume that the background continuum has been subtracted away, so that the distribution for each gas is mostly zero, with a few positive τ's representing strong, thin lines. In this case, a number of $\tau_i(G)$ distributions can be combined very simply via

$$\{\tau_{12\ldots n}\} = \bigcup_{i=1}^{n} \{\tau_i(G > 1 - 1/n)\} \tag{16a}$$

or, for two gases,

$$\{\tau_{12}\} = \{\tau_1(G > 0.5)\} \cup \{\tau_2(G > 0.5)\}. \tag{16b}$$

After effecting the set union, one repeats the sorting operation and calculates G_{12}, the cumulative distribution function for the set $\{\tau_{12}\}$. Finally, one adds to each τ_{12} some constant (independent of G) representing the sum of the two continua that had been subtracted away.

An alternative formulation in terms of the cumulative distribution functions them-

selves is

$$G_{12}(\tau) = G_1(\tau) + G_2(\tau) - 1. \tag{17}$$

In Eq. (17), as in Eq. (16), one assumes that any background continua have been subtracted out before the two gases are combined. Therefore the range of τ_{12} is from 0 to the larger of $\tau_{1\max}, \tau_{2\max}$. The zero presents a slight awkwardness in that the program cannot now select sample values of τ at equal logarithmic intervals, but to evade this difficulty it can replace the zero by something like $\tau_{\max}/10000$. Again, the final step is restoring the continuum.

To see the meaning of Eq. (17), consider a pair of $\tau_i(G)$ distributions that are narrow triangular spikes:

$$G_1(\tau) = \epsilon_1 \tau/h_1 + 1 - \epsilon_1 \quad \text{for } 0 < \tau < h_1, \tag{17a}$$

$$G_2(\tau) = \epsilon_2 \tau/h_2 + 1 - \epsilon_2 \quad \text{for } 0 < \tau < h_2. \tag{17b}$$

Assume that ϵ_1 and ϵ_2 are both small compared to unity. Without loss of generality, assume $h_1 < h_2$. Then, if the spectral overlap is actually nil, the exact distribution of optical thicknesses for the mixed gas must be the same as G_2 for values of τ_{12} exceeding h_1. Thus $G_{12}(h_1)$ is $1 - \epsilon_2 + \epsilon_2 h_1/h_2$. Furthermore, for $0 < \tau_{12} < h_1$, G will be a linear function. It must reach $\tau = 0$ at $G = 1 - \epsilon_1 - \epsilon_2$, because we have assumed that no absorption of gas 1 coincides spectrally with any absorption of gas 2. Next, constructing the straight line between the two points just mentioned gives $G_{12}(\tau) = (\epsilon_1 + \epsilon_2 h_1/h_2)\tau/h_1 + 1 - \epsilon_1 - \epsilon_2$. But this is exactly $G_1 + G_2 - 1$, for the range $0 < \tau_{12} < h_1$; the correctness of Eq. (17) in the other ranges is trivial.

In case the line-by-line program, from which the component $\tau_i(G)$ datasets are produced, does not provide an easy way to define and subtract a background continuum absorption, one can define

$$\bar{\tau}_1 = (1/a)\int_0^a \tau_1(G_1)dG_1, \tag{18}$$

and a similar expression for $\bar{\tau}_2$. The "a" is just some constant between 0 and 1; I found $a = 0.4$ to be about right for the application at hand, but the best value clearly depends on the shape of $\tau(G)$, and might increase or decrease with pressure. Next, one uses $\bar{\tau}_1$ and $\bar{\tau}_2$ to modify Eq. (17) as follows:

$$G_{12}(\tau) = G_1[\tau - \bar{\tau}_2(a)] + G_2[\tau - \bar{\tau}_1(a)] - 1. \tag{19}$$

Now the range of τ_{12} is from $\bar{\tau}_1 + \bar{\tau}_2$ to the larger of $\bar{\tau}_1 + \tau_{2\max}$ or $\bar{\tau}_2 + \tau_{1\max}$. Within this domain, I chose to calculate $G(\tau)$ on a set of τ's at equal logarithmic intervals because $G(\log \tau)$ is roughly linear for many spectra; this implementation proved successful.

An analogue of Eq. (16b) for the case where the continuum has not been stripped away beforehand is

$$\{\tau_{12}\} = \{\tau_1(G > 0.5) + \bar{\tau}_2(a)\} \cup \{\tau_2(G > 0.5) + \bar{\tau}_1(a)\}. \tag{20}$$

There is no guarantee that $\tau_2(G = 0.6) > \tau_1(G = 0.4)$, for instance. In case errors arise from this fact, Eq. (16b) can be amended to:

$$\{\tau'\} = \{\tau_1\} \cup \{\tau_2\} \text{ and } \{\tau_{12}\} = \{\tau'(G > 0.5)\}, \tag{21}$$

where G is the cumulative distribution of the union $\{\tau'\}$. So we are considering all the optical thicknesses of both components, and selecting the half of them that have the largest τ_i values.

It is to be expected that these no-overlap methods will work very well at high altitudes, while the 100-point convolution works well near the ground. A plausible algorithm for middle altitudes is the even simpler

$$G_{12}(\tau) = G_1(\tau)G_2(\tau). \tag{22}$$

Like Eq. (17), this assumes that only line-cores are included, so that each $\tau_i(G)$ has a narrow spike near $G = 1$, and τ_i is near zero elsewhere. The range of τ_{12} is as in Eq. (17). The relation between Eqs. (17) and (22) can be seen by returning to the simplified case where both spikes are triangular. Multiplying the G_1 and G_2 from Eqs. (17a) and (17b), we obtain

$$G_1(\tau)G_2(\tau) = 1 - \epsilon_1 - \epsilon_2 + \epsilon_1\tau/h_1 + \epsilon_2\tau/h_2 \quad \text{plus terms of the order } \epsilon_1\epsilon_2. \tag{22a}$$

But omitting the second-order terms, this is just $G_1 + G_2 - 1$. At high altitudes, where a narrow spike is a reasonable representation of each $\tau_i(G)$ function, Eq. (22) restores the probabilistic overlap that was eliminated by Eq. (17). Note that $G_1(0) = 1 - \epsilon_1$, and $G_2(0) = 1 - \epsilon_2$. The probabilistic overlap of the spectral lines is $\epsilon_1\epsilon_2$, and the product $G_1(0)G_2(0)$ is the same as $G_1(0) + G_2(0) - 1 + \epsilon_1\epsilon_2$, so that Eq. (22) gives the probabilistically correct value of $G_{12}(0)$. An analog of Eq. (22) for the case where continua have not been stripped away is

$$G_{12}(\tau) = G_1[\tau - \bar{\tau}_2(a)]G_2[\tau - \bar{\tau}_1(a)]. \tag{23}$$

The physical and computational assumptions connected with the algorithms of this section are summarized in Table 2.

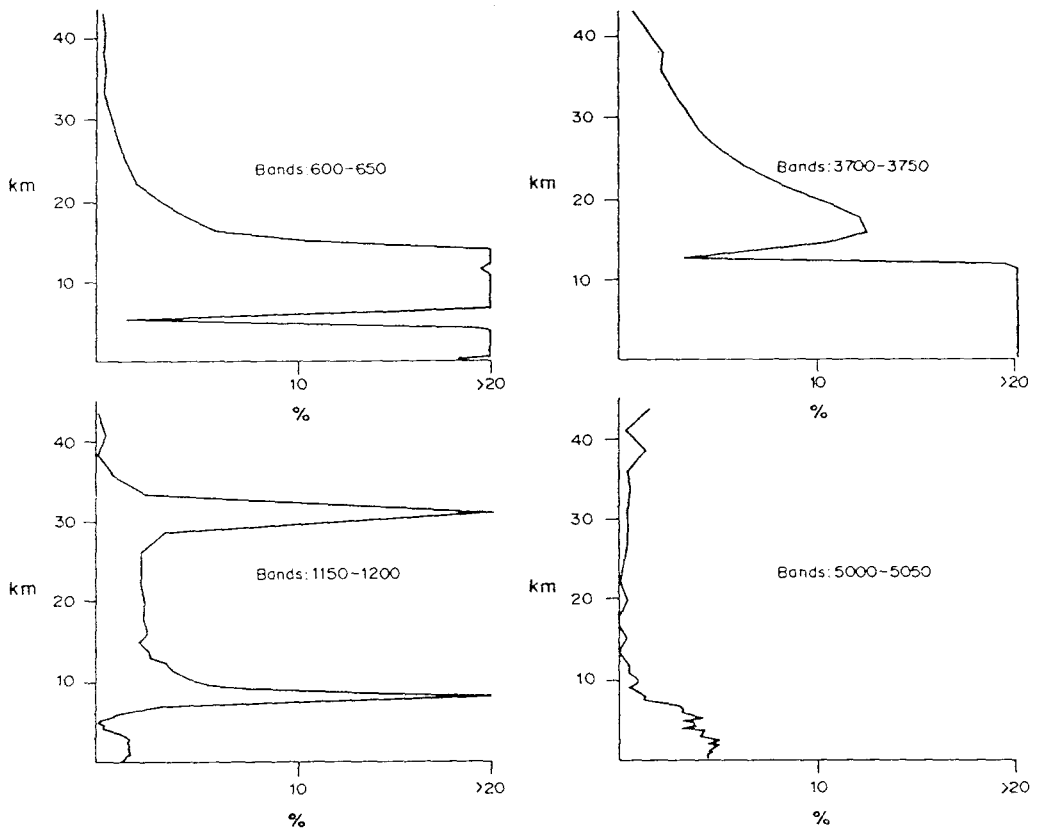

Fig. 10. When Eq. (19) is used to mix gases and recalculate the heating rates of Fig. 3, it introduces relative errors whose absolute value is the abscissa here. Comparison of Fig. 10 against Fig. 5 leads to the choice of cutoff levels in Fig. 11.

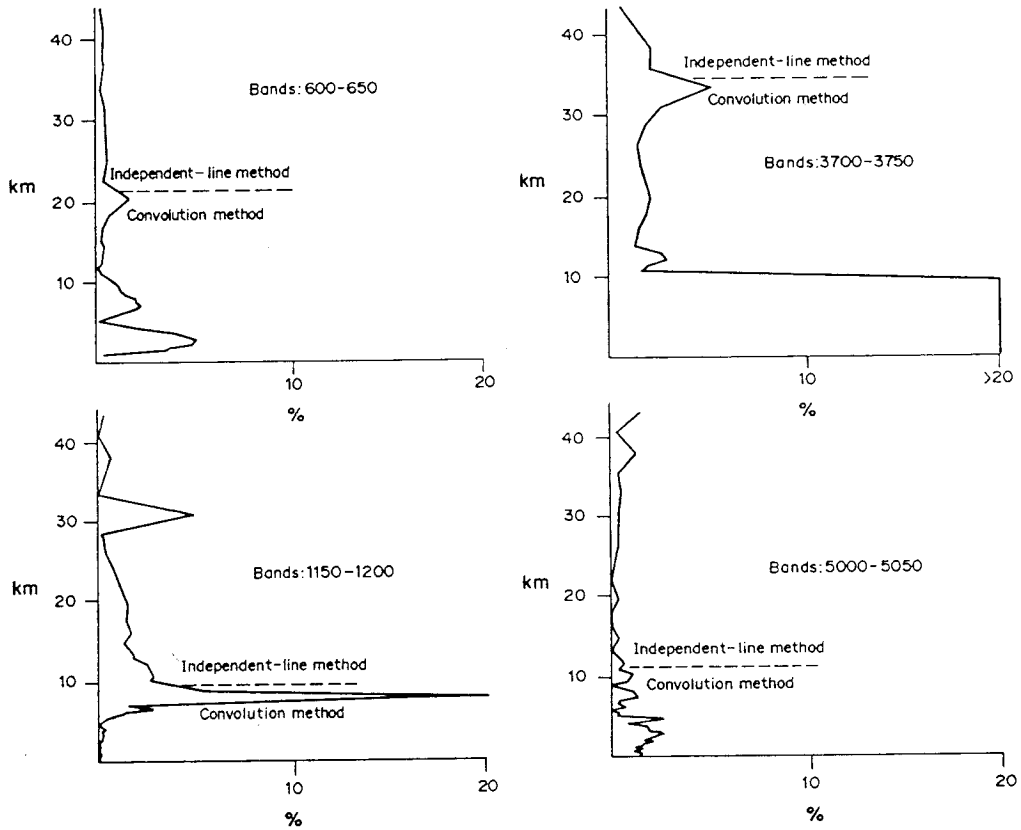

Fig. 11. When the GWCC convolution on 100 points is used at low altitudes, and Eq. (19) at high altitudes, the relative errors in the heating or cooling rates are reduced. (Compare against Figs. 5 and 10.)

4. Application of the Speed-Optimized Methods

(a) Comparisons of accuracy

As a first illustration of the efficacy of the independent-line methods defined by Eqs. (16)–(21), the reader should compare Fig. 11 against Figs. 4 and 5. In Fig. 11, the sparse data were handled by Eq. (19) at low pressures and by Eq. (7) at high pressures. The result is not as good as the 1000-point convolution, but the method is two orders of magnitude faster.

Figure 10 shows what happens if Eq. (19) is used throughout the column. The only intent of this figure is to provide a preliminary rationale for the choice of locating the interface, the dashed line in Fig. 11.

Next, we want to compare the nuances of the various methods of Eqs. (16)–(23). All of Figs. 3 through 11 involved absorption spectra in which the lines and background continuum were not computationally separated, since separating them does not improve the accuracy of the convolution method.

A sensitive comparison of the various independent-line methods, and the related simplification Eq. (22), is better executed on the lines only. For the range $G = 0.9$–1.0, Fig. 12 shows the small errors in $\tau_{12}(G)$ arising from Eqs. (16), (17) and (22). The accuracy of Eqs. (17) and (22) becomes indistinguishable in the limit $G = 1$, as one would expect from the argument following Eq. (22). For $G > 0.9$, method (16) does not appear appreciably more or less accurate, but in our implementation it was seven times faster. This is because directly implementing Eq. (17) or (22) requires searches and interpolations, as the $\tau_i(G)$ distributions for the two component gases were stored for a standard set of G values. One

could imagine an implementation in which the τ values rather than the G values are a standard set, but then one has the further problem of predetermining the range of τ. So far, I have shown no compelling reason to recommend any of Eqs. (16), (17) or (22) over any other.

However, Fig. 13(a) compares the accuracy of heating rates calculated by Eqs. (16), (17), and (22) all the way down to the ground. One should not try to use any of these methods in that way, but the comparison shows that even in the upper layers, (16) is by far the least accurate. Farther down, Eq. (22) begins to show an advantage over (17), as the assumption that lines do not overlap begins to fail.

The difference between Figs. 13(a) and 13(b) can be understood by referring back to Fig. 8. We see Eq. (16) doing very badly in the 600-650 cm^{-1} band because the domain of small G values, which (16) misrepresents, contributes importantly to the cooling in that band. For the 5000-5050 cm^{-1} band, on the other hand, the heating is strongly dominated by the largest G values, so that Eq. (16) produces no heating-rate errors of more than 1.5% until we get to pressures higher than 600 mb. Near the ground, small G's do contribute significantly to the heating. (Recall Fig. 8.)

Wanting to retain the performance advantage of Eq. (16), I modified it very slightly to achieve the effect of (21). Figures 14(a) and 14(b) confirm that this method is more accurate than the methods that emulate continuous functions, except in the lowest 5 km of the atmosphere, where one would not choose to apply any of the methods introduced in Sec. 3.

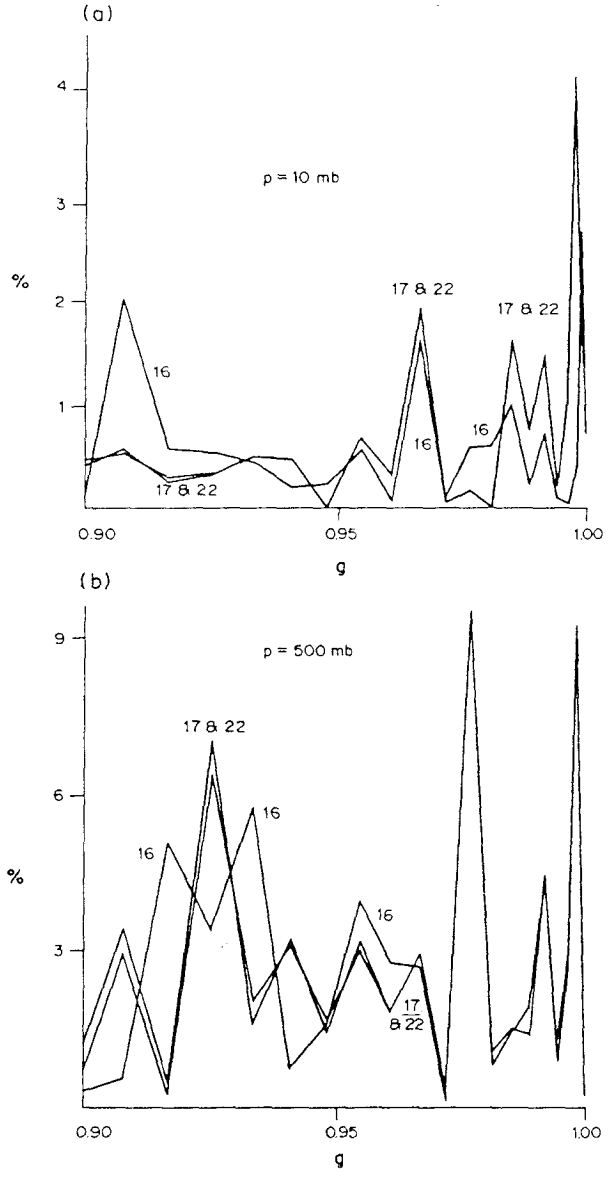

Fig. 12. Errors introduced in the tau-distribution by several mixing methods are compared. See Eqs. (16), (17), and (22). The spectral domain in both panels is 600–650 wavenumbers. The ordinate is the absolute value of the relative error in log(tau). Only the largest 10% of the optical thicknesses ($g > 0.9$) are shown.

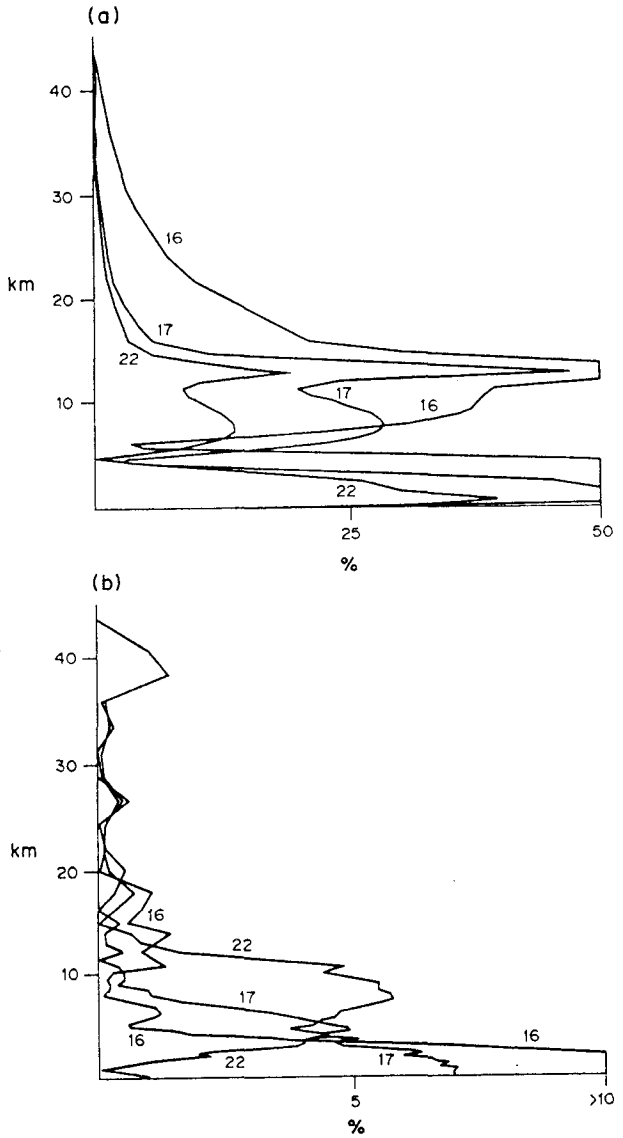

Fig. 13. Errors introduced in heating rates by several mixing methods are compared. See Eqs. (16), (17), and (22). The spectral domain in the upper panel is 600–650 wavenumbers; in the lower panel, 5000–5050. The abscissa is the absolute value of the relative error.

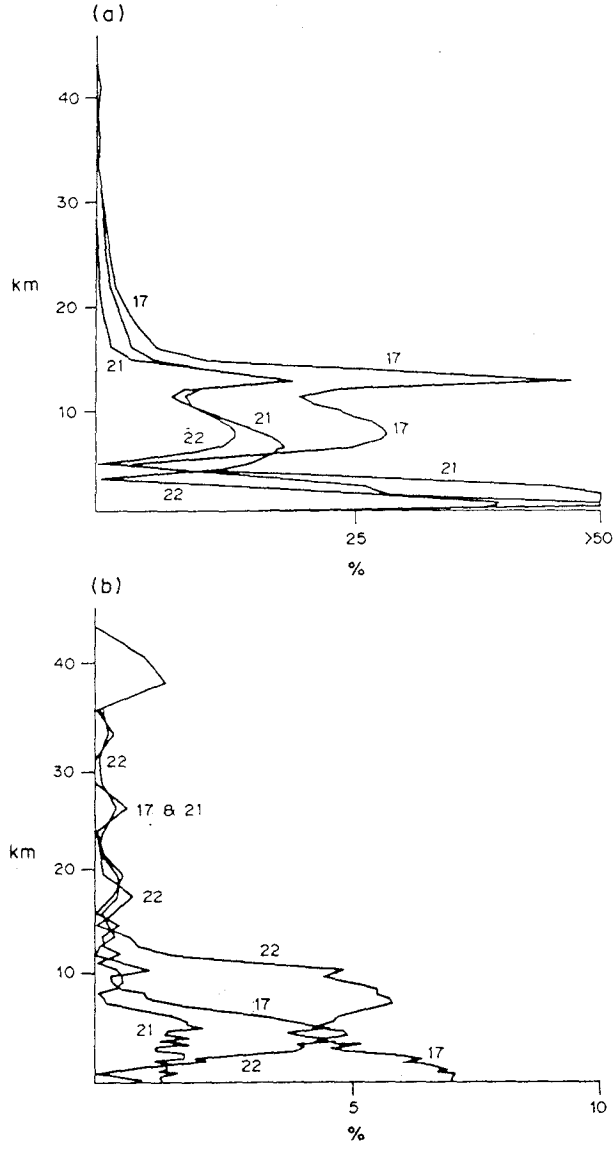

Fig. 14. The large errors associated with Eq. (16) in Fig. 13 suggest replacing it with Eq. (21), which proves superior to both of the "continuous" Eqs. (17) and (22). Spectral domains are as in Fig. 13.

Physically, Eq. (22) might be expected to be more accurate, but the convenience of storing optical thicknesses for a standard set of G values rather than a standard set of τ values is a likely source of the observed advantage of Eq. (21). The number of sample τ's selected from the domain of Eqs. (17) and (22) would have to be much greater than the number of stored τ's used in Eq. (21), to eliminate the undesirable effect of the interpolation. The more general conclusion suggested by Figs. 14(a) and 14(b) is that the differences in accuracy between the approaches of Eqs. (17), (21), and (22) are quite small at the altitudes of interest, so that computational speed and convenience become the criteria for choosing among them.

(b) Finding the interface level

If we have satisfied ourselves that sufficiently accurate cumulative k-distributions for a multi-layered gas mixture can be obtained by using the convolution in each low-altitude layer and some no-overlap algorithm in each high-altitude layer, then we have the problem of deciding how to predict the level where the change from the one algorithm to the other should be imposed. There is the unpleasant possibility that this depends on the chemical profile.

However, we have also observed that even for a fixed chemical profile, the optimal interface level varies sharply from band to band. I shall treat this variation first. We have observed some bands where one needs to abandon the convolution above 6 km, and others where it seems viable to 30 km or more. It is possible that the optimal interface level is related to some parameter measuring the ratio of linewidth to line-spacing. Consider that the overlap among lines should increase with the average linewidth, and should also increase

as the average spacing between lines decreases. Thus, we might expect the appropriate altitude range for the convolution to increase with a dimensionless parameter $\bar{\alpha}/\delta$, where $\bar{\alpha}$ is an average linewidth for the band, and δ is the bandwidth divided by the number of lines. Furthermore, if we suppose that the logarithm of pressure decreases linearly with increasing altitude, and that linewidth is proportional to pressure, then we should construct a regression line for the (empirical) optimal altitude vs. the $\log(\bar{\alpha}/\delta)$. For each of ten bands, I calculated $\bar{\alpha}/\delta$ from the HITRAN archive (7) for each of the two gaseous components of our mixture. The best correlation coefficient (+78%) between the optimal z and the $\log(\bar{\alpha}/\delta)$ was obtained when I considered only whichever gas showed the greater $(\bar{\alpha}/\delta)$ value for the particular broadband in question. I attempted various weightings of linewidth by linestrength, but none of these improved the 78% correlation. The regression line in my experiment was

$$z(\text{km}) = 14.16 + 7.79 \log_{10}(\bar{\alpha}/\delta), \tag{24}$$

but a more exhaustive experiment would suggest some refinement.

Table 2. Physical and computational assumptions for the equations of Sec. 3.

Condition	Equations						
	16	17	19	20	21	22	23
Low pressure implying narrow lines and narrowly spiked tau(G)	X	X	X	X	X	X	X
No single line of gas 1 overlaps any single line of gas 2	X	X	X	X	X		
Component tau(G)'s for standard set of G's; minimize interpolations	X			X	X		
Background absorption of both gases has been eliminated; will be restored separately	X	X			X	X	
Order-of-magnitude errors in tau(G) OK for G values < 0.5	X			X			

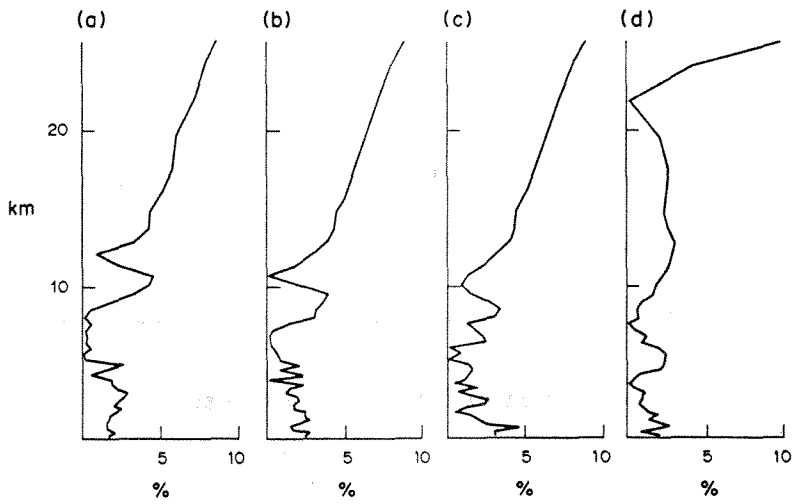

Fig. 15. Changes in absolute humidity have only minor effects on the relative error in heating rates due to the 100-point GWCC convolution. The spectral domain is 5000–5050 wavenumbers. (a) Model atmosphere is from Table 1. (b, c, d) The absolute humidity in each layer has been multiplied by a factor of (b) 0.3, (c) 0.2, (d) 0.05.

Next, we turn to variation with composition. Figure 15 returns to the 5000-5050 cm^{-1} band of GWCC's prototype experiment, and presents the errors introduced by the GWCC convolution when the absolute humidity of the atmosphere from Table 1 is uniformly reduced by a factor of 0.3, 0.2, or 0.05. The typical magnitude of the errors in the troposphere is not markedly increased by these changes. The reason for selecting 0.3 and 0.2 is that, for the atmospheric model shown in Table 1, these reductions of absolute humidity result in the maximum spectral optical thickness of the water in a layer of the lower troposphere being about the same as the maximum spectral optical thickness of the dry gas. Thus, we give the convolution every chance to fail, if it were going to fail here as at high z. But it succeeds, for the reasons suggested in Sec. 2(d).

Finally, I sought the optimal level at which to change from the convolution for low altitudes to the independent-line algorithm high altitudes, in each of the cases of Fig. 15. The "best" choices were to include either 30 or 31 of the 50 layers in the lower slab treated by the convolution. Differences in the quality of the result when the "wrong" one of these choices was used were very small. This preliminary finding suggests the location of the optimal interface level is not highly sensitive to chemical changes. Thus, it should be possible to specify, in advance of repetitive radiative calculations with changing chemical profiles, at what altitude the change from convolution to independent lines should be made, for each spectral range. Further experiments would be needed to explore the robustness of Eq. (24).

5. Support Software

(a) FASCOD2, HITRAN '86

Closely-spaced spectral optical thicknesses for each layer were produced by an enhanced version of FASCOD2 (8,9). For each spectral line, FASCOD2 approximates a Voigt profile out to 25 cm^{-1} from the line center, using data from the HITRAN 1986 archive of spectroscopic data. The far wings are not calculated individually, but treated as a slowly-varying continuum, parameterized in ways that vary from one gas to another. For a description of the FASCOD2 treatment of the water vapor continuum, see Clough, Kneizys and Davies (10). FASCOD2 can give the user optical thicknesses for line-cores only, for far wings only, or for the combination. In Secs. 3 and 4, the several mentions of "stripping away the continuum" referred to having FASCOD2 add up only the absorption contributed by lines within 25 cm^{-1} of any particular frequency. However, the concept is not unique to FASCOD2; no line-by-line program calculates line-wings out to infinity, and some parameterization of far wings is usual.

(b) Layer-adding program

Each cumulative τ-distribution of the combined gas was passed to the same doubling-and-adding program used in GWCC. A new module supplied the photon flux at the top of the atmosphere following Nicolet (11), enabling the solar heating rates to be given in K/day. Another new module provided band-adding capabilities for the tests of Sec. 6 below. My recent validations of the doubling-and-adding programs included some qualitative comparisons against the graphical results of Stamnes and Tsay (12), and many comparisons against the tabulated results of van de Hulst (13). For the latter, agreement

to at least three significant digits was achieved in all cases.

Although the strength of a doubling-and-adding program lies in its capability to perform rapid calculation of multiple scattering effects, no scattering is included in the tests of the present paper. The present focus is the error introduced in the absorption optical thicknesses, by the various gas-mixing algorithms.

In all experiments shown, a six-stream approximation was used for the spherical integration. A solar zenith angle of 55° was used for the two solar bands.

6. Results of Spectrally-Integrated Tests

The method of principal absorbers is so much faster than the methods of Secs. 2 and 3 that I find it necessary to show a real advantage in the latter methods. I formulate the method of principal absorbers in the notation of Secs. 2 and 3 as follows:

$$\tau_{12}(G) = \tau_1(G) + \tau_2(0.5). \tag{25}$$

This method can be expected to do well under two circumstances: (a) the absorption is strongly dominated by one of the two gases, or (b) the absorption of one of the two gases varies only slowly with frequency. This latter circumstance makes Eq. (25) a plausible way of handling the red bands of visible, where water lines are important, but the strong absorption of ozone varies slowly. Apart from (a) and (b), we could ask how well or badly Eq. (25) does when applied arbitrarily.

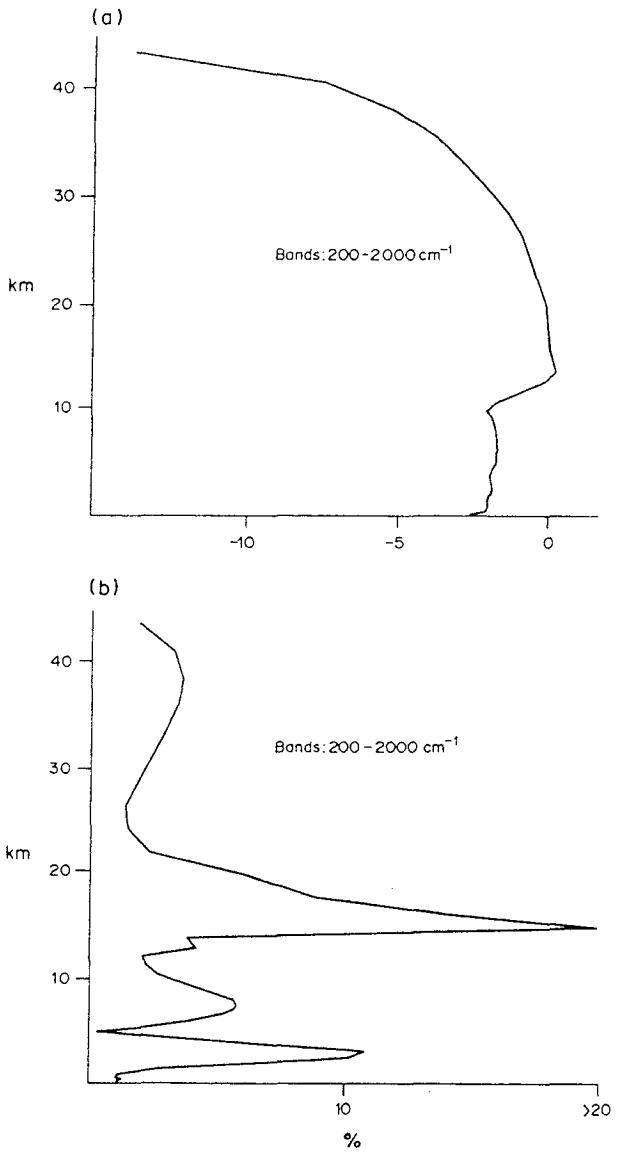

Fig. 16. The upper panel shows the spectrally-integrated thermal cooling of the Table 1 atmosphere, calculated from the cumulative tau-distribution of the spectrally-mixed gas, for 38 bands whose cooling rates are then added. Units are K/day. The lower panel shows the absolute value of the relative error introduced by the method of principal absorbers.

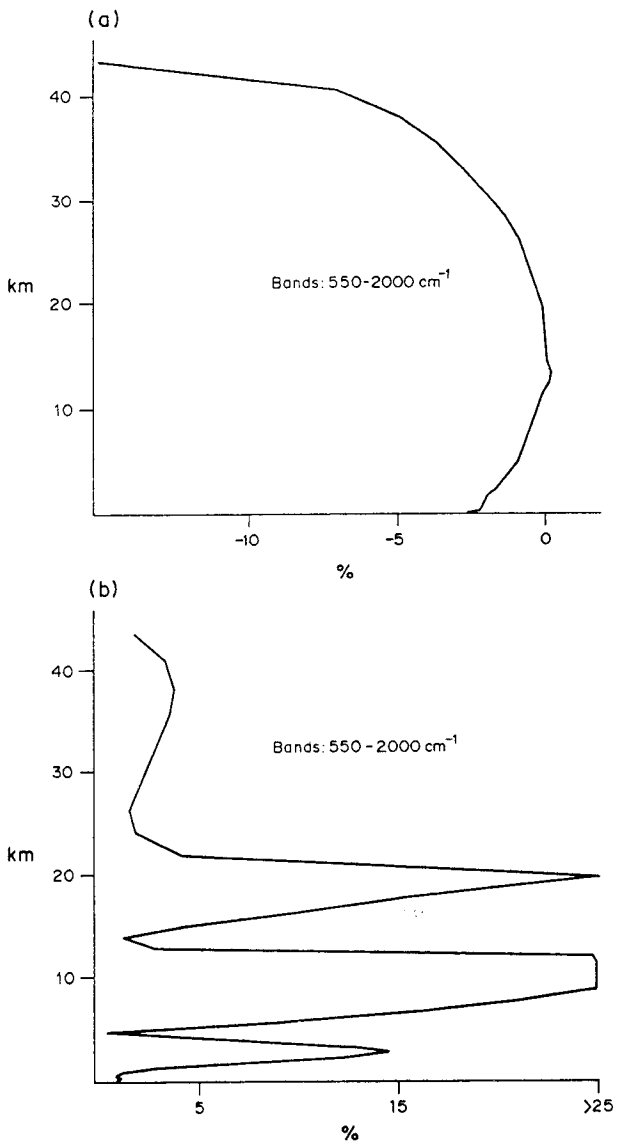

Fig. 17. When the rotation bands of water are omitted, the errors introduced by the method of principal absorbers become more evident. This figure is similar to Fig. 16 except that the spectral domain 200–550 wavenumbers is left out.

Figure 16 shows spectrally-integrated thermal cooling for 38 narrow bands spanning 200-2000 cm^{-1}, and the error introduced by a crude application of the method of principal absorbers to the atmosphere of Table 1: that is, I select one gas as the principal absorber for each narrow band, and add a constant representing the median absorption of the other gas over the spectrum of that band. The result seems good on the face of it. The median error for the 50 layers of the model is only 3.5%. However, Fig. 17 puts a different light on it. This omits the region 200-550 cm^{-1}, where the rotation bands of water entirely dominate, and where the method of principal absorbers therefore works particularly well. When these bands are omitted, the median error for the 50 layers rises immediately from 3.5% to 6.5%, and for 10 of the layers we have errors of 19% or more. Possibly these errors could be much reduced by choosing principal absorbers for each layer, and not just by bands.

The methods suggested earlier in the present paper are compared to the principal-absorbers method in Figs. 18 and 19, for the important 15-micron CO_2 band and 10-μm ozone band. The "principal" absorber for each of these was the pre-mixed combination of the five dry absorbing gases in Table 1; a constant was added representing the median ($G = 0.5$) absorption of water vapor. These were the only bands in the Fig. 16 calculation for which water vapor was not taken to be the principal absorber. As expected, we see the larger errors in Figs. 18 and 19 in the troposphere, where water is important. I conjecture that the error falls off very near the ground because the water lines are so broadened that their median becomes a reasonable representation of their k-distribution. The error curves marked "S" were constructed in a manner similar to Fig. 11. Table 3 shows where the

change from an independent-line algorithm to the convolution algorithm occurred, for each narrow band. The admitted shortcoming of my methods here is that I did not predict the levels where I should switch from Eq. (19) to Eq. (7), but selected them for a favorable outcome.

A comparison of Fig. 16 with Fig. 17 makes it clear that the method of principal absorbers worked very well for the rotation bands of water. The region $\nu < 550$ cm^{-1} can be treated as a pure water band over a wide range of humidities. Apart from that, I recommend more precise methods for all of the terrestrial thermal spectrum, and much of the solar spectrum too. An interesting possibility, not yet implemented, is that the program should choose Eq. (25) rather than (21) or (7), if it finds that the maximum τ for one of the gases exceeds the maximum τ for the other gas by a few orders of magnitude.

Finally, note that the comparisons in the present paper are not strongly dependent on the accuracy of either the line-by-line calculation of the component k's, or the radiative transfer calculations from the final k-distribution. An investigator substituting a different line-by-line program will start with slightly different component k-distributions; an investigator preferring a different radiative transfer calculation will obtain different heating rates. The magnitude of the errors introduced by the method of mixing the cumulative k-distributions should depend only weakly on the details of these other modules.

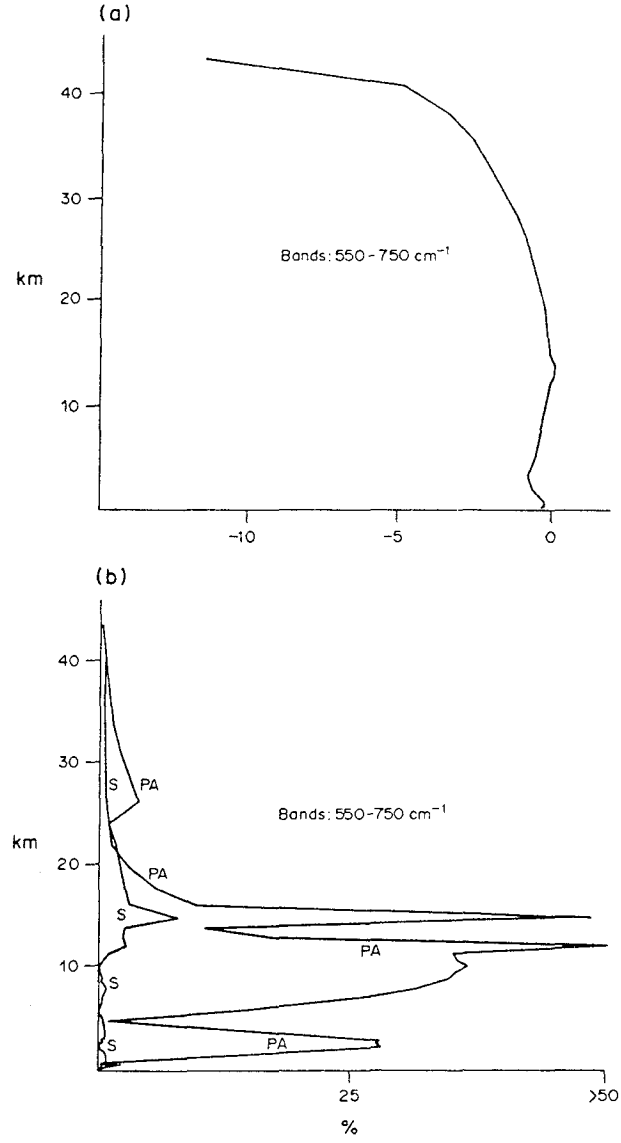

Fig. 18. The upper panel shows thermal cooling for just 4 of the bands from Fig. 16, spanning the 15-μm CO_2 band. Units are K/day. The lower panel compares the absolute value of the relative error introduced by the method of principal absorbers (PA) to that introduced by a split-level method (S) that uses Eqs. (7) and (19).

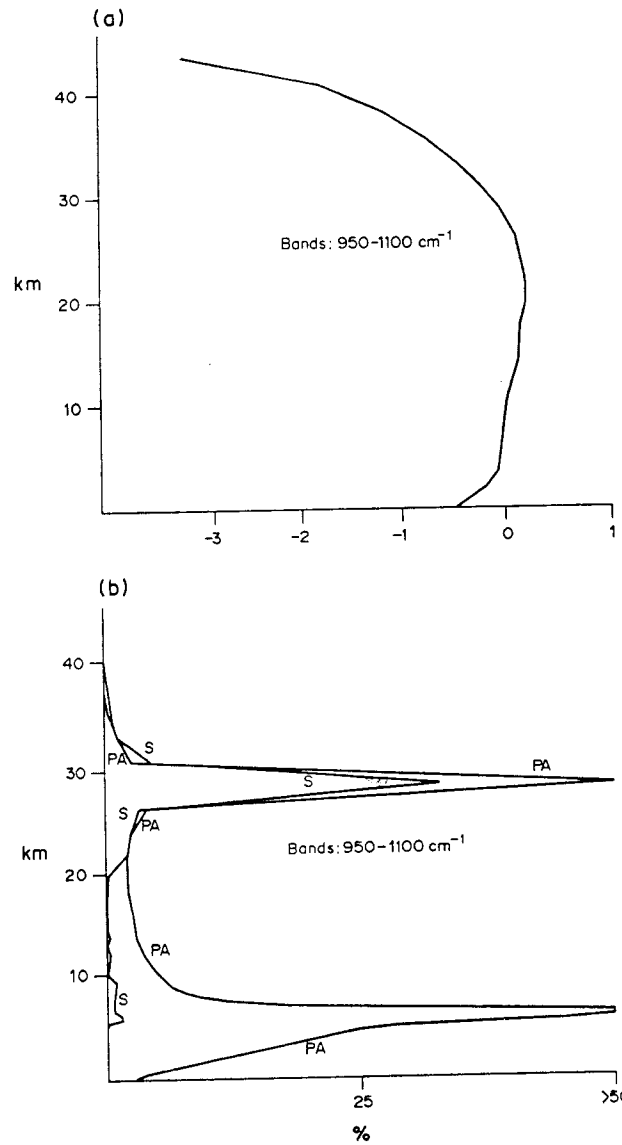

Fig. 19. The upper panel shows thermal cooling for just 3 of the bands from Fig. 16, spanning much of the 9.6-μm band of ozone. Units are K/day. The relation of the lower panel to the upper is as in Fig. 18.

However, the present methods would be useless if one did not believe in the overall viability of the correlated-k method. This paper makes no specific quantitative claim about the accuracy of the correlated-k method when applied to deep, inhomogeneous atmospheres, but Refs. 1, 2, 14, and 15 discuss that subject, with conclusions varying in emphasis.

Acknowledgements - This work was carried out while the author was supported by NASA Training Grant NTG-30016. The author thanks S. A. Clough and R. D. Worsham for providing access to FASCODE; L. Chen for providing access to his convolution program used in the GWCC study; R. A. West for providing access to his doubling-and-adding program. I am grateful to R. M. Goody, who directed this work in its early stages and contributed many important ideas. R. A. West provided useful criticisms of several late drafts of the paper; B. F. Farrell's comments were also appreciated.

References

1. A.A. Lacis and V. Oinas, *J. Geophys. Res.* **96**, 9027 (1991).

2. R.M. Goody, R.A.West, L. Chen, and D. Crisp, *J. Quant. Spectrosc. & Rad. Transfer* **42**, 539 (1989).

3. L.D. Kaplan, *Proc. of the Toronto Meteorological Conference 1953*, p. 49. London, Royal Meteorological Society (1954).

4. D.E. Burch, J.N. Howard, and D. Williams, *J. Opt. Soc. Am.* **46**, 452 (1956).

5. P.R. Bevington, *Data Reduction and Error Analysis for the Physical Sciences.* New York, McGraw-Hill (1969).

6. W.L. Ridgway, Harshvardhan, and A. Arking, *J. Geophys. Res.* **96**, 8969 (1991).

7. L.S. Rothman, R.R. Gamache, A. Goldman, L.R. Brown, R.A. Toth, H.M. Pickett, R.L. Poynter, J.-M. Flaud, C. Camy-Peyret, A. Barbe, N. Husson, C.P. Rinsland, and M.A.H. Smith, *Appl. Opt.* **26**, 4058 (1987).

8. S.A. Clough, F.X. Kneizys, E.P. Shettle and G.P. Anderson, *Proc. of the Sixth Conference on Atmospheric Radiation*, p. 141, Williamsburg, Va (1986).

9. S.A. Clough, R.D. Worsham, W.L. Smith, H.E. Revercomb, R.O. Knuteson, G.P. Anderson, M.L. Hoke, and F.X. Kneizys, *Proc. of IRS '88*, A. Deepak Publishing (1989).

10. S.A. Clough, F.X. Kneizys, and R.W. Davies, *Atmos. Res.* **23**, 229 (1989).

11. M. Nicolet, *Planet. Space Sci.* **37**, 1249 (1989).

12. K. Stamnes and S.-C. Tsay, *Planet. Space Sci.* **38**, 807 (1990).

13. H.C. van de Hulst, *Multiple Light Scattering: Tables, Formulas, and Applications.* New York, Academic Press (1980).

14. R.A. West, D. Crisp and L. Chen, *J. Quant. Spectrosc. & Rad. Transfer* **43**, 191 (1990).

15. K.R. Minschwaner and M.B. McElroy, *Planet. Space Sci.* **40**, 1237 (1992).

Appendix 1

Context and application of correlated-k

When Paper I was written, community interest in the correlated k-distribution method was high, as evidenced by references 1, 2, 14, and 15 cited there. GWCC (2) had claimed 1% accuracy in their k-distribution calculations of radiative flux divergences. Several limitations of the GWCC experiments were accurately reported, but not emphasized. Not all of these limitations were within the scope of Paper I; to that extent, they are discussed here, along with the results of related experiments I performed later.

1. Altitude limitation

All of the GWCC prototype experiments involved an atmospheric column extending from the surface to 50 mb, so there was no direct evidence that the method would be effective in the middle to upper stratosphere. In retrospect, the probability of difficulties at greater altitudes seems to have been high, since the flux divergence errors at 150 mb in the GWCC experiments were more like 5% than 1%, and at 50 mb were more like 25%. It was felt that the errors at 50 mb were perhaps not "real", since the top layer of any artificially truncated model slab may produce peculiar results at a boundary. This feeling proved justified, for when I later tested the non-convolved k-distribution of a gas mixture to obtain heating rates in a 30-layer column, 60 km deep, I found that the 25% errors again appeared only in the top 1 or 2 layers. However, the 5% or 7% errors in thermal flux divergence appeared throughout the middle and upper stratosphere. My finding is

consistent with that of Minschwaner and McElroy (15), whose Figure 3 shows errors on the order of 5% at various pressures lower than 10 mb, but not in the lower stratosphere.

The source of these errors is probably the decorrelation of mixing ratios, along with the effect of changing lineshapes as pressure falls by a second and third order of magnitude. The sorting of spectral optical thicknesses is known as the "correlated-k" method precisely because it depends on spectral peaks' appearing at the same frequencies in different layers. This condition is violated to some extent if the gas mixing ratios change from one layer to another. The transition from water-dominated cooling in the troposphere to CO_2-dominated cooling in the stratosphere is the most obvious problem. Another example is the asymmetric stretching band of ozone, which overlaps the long-wave wing of the bending band of water, so that this region of the spectrum at the earth's surface is not well correlated with that at 30 km.

The effect of changing lineshapes is more subtle. In Lacis and Oinas (1) we see that it causes no problem for k-distribution calculations in a 100-km-deep atmosphere consisting of CO_2 alone. In the case of a vertically homogeneous gas mixture, a problem is expected because the various molecules change from Lorentz shape to Doppler shape at different altitudes. I did not perform the experiments needed to partition the error among these two sources, nor did GWCC report detailed results of their "Case N," a homogeneous mixture of water and CO_2. I agree with their evident decision that "Case O," a mixture with strong gradients, deserved a more thorough report. A series of tests involving homogeneous gas mixtures might help isolate the error due to changing lineshapes, since any error due to changing mixing ratios would be eliminated. It might be worthwhile to pursue such an

investigation, since I found less overall error in the immediate vicinity of the tropopause than at somewhat higher altitudes. This is not the effect expected if mixing-ratio gradients were the dominant error source. Yuk Yung has pointed out that the decorrelation errors may become more apparent as one ascends into optically-thin layers where photon mean free paths are long. A test of his hypothesis (not yet executed) would involve increasing the model concentrations of absorbers in low-pressure layers, to see whether optical thickness alone would make the k-distribution methods more robust.

The high-altitude tests I did perform included comparisons against the line-by-line results of Ridgway *et al* (6) for a three-gas mixture and a full thermal spectrum. Here my k-distribution for the mixture was obtained from the spectrum of the mixture, not from "mixing" the k-distributions of the gases. Accuracy of 5% or 7% would be acceptable if thermal cooling rates were all that we required, but the *net* radiative heating of a stratospheric layer is usually the difference between two much larger terms, since the stratosphere is nearly in radiative equilibrium. Therefore the 5% errors in thermal or solar flux divergence might tend to translate into 40% errors in net radiative heating, which is the quantity relevant to calculating what diabatic circulation would balance the heating. The net heating errors reported in GWCC were not thus amplified, because they involved a single spectral interval in which solar heating was much larger than thermal cooling. Had GWCC's estimate of 1% error in solar heating proven robust in the stratosphere, the errors in net heating would still have been acceptable; so far, it has not. There is a possibility that dividing the spectrum into much narrower bands would improve the altitude range of correlated-k, but preliminary tests suggested 25-cm^{-1} bands did not improve much on

50-cm^{-1} bands.

2. Gas-mixing limitations

Another limitation of the GWCC prototype experiments was that the two tests for gas mixtures were performed with 500 values of G in each component distribution, and in the mixture's distribution as well. The idea that *k*-distribution calculations would be very efficient was based on the notion that a spectral interval of 50 cm^{-1} could be represented by 10 points (GWCC Sec. 5), whereas the use of 500 points slowed the convolution operation by a factor of $50^2 = 2500$. Paper I solves this problem to some extent, but does not address the further difficulty of dealing with spectral regions in which more than two absorbers are important. In experiments not reported elsewhere, I found that convolving the *k*-distributions of two gases, and then convolving a third gas into the mixture, had the effect of nearly doubling the error. This difficulty could possibly be resolved by choosing a *pair* of "principal absorbers" for each spectral interval, mixing them by the methods of my foregoing paper, and then treating the two-gas mixture as the principal absorber, in the sense of Paper I. This solution would avoid any three-gas convolutions, and its efficacy could be determined by examining the few spectral regions where water has more than one absorbing competitor.

3. Recent progress by Xun Zhu

Recently Dr. Xun Zhu (1994) has submitted a paper characterizing the GWCC convolution as "incorrect." He also treats as a resolvable paradox my example of a spectrum that satisfies the multiplication property but not Goody's convolution. The essence of

Zhu's insight is that the definition appearing in GWCC and Paper I,

$$F(\tau) = f(k)/m, \tag{1}$$

is inappropriate because, for a given τ, both $f(k)$ and m can vary. If a spectrum satisfies the multiplication property for *all* values of m, then a convolution theorem will be satisfied as well—not exactly the same convolution theorem as GWCC's.

Dr. Zhu's numerical results (his Fig. 3, analogous to my Fig. 7) show that his convolution produces fractional errors in the k-distribution, limited to 6% at all g greater than about 0.02. However, he has not shown a layer where the maximum absorptions of two convolved spectra are comparable (the case leading to the large errors of my Fig. 7). Nor has he yet translated his accurate convolution into accurate calculation of thermal cooling in a multi-layered atmosphere, but I shall follow his research with interest.

4. Status

In sum, modest refinements could make the k-distribution method a valuable tool at least for tropospheric radiative transfer calculations, and probably extend their range through the lower stratosphere despite the mixing-ratio gradients that exist there. It should also work well in atmospheres strongly dominated by a single absorbing gas. Zhu's papers show that k-distribution calculations still command interest in the community, even though no major operational model has adopted them. Their most likely sphere of relevance is in 2D modeling, since they cannot intrinsically satisfy the speed requirements of 3D modeling (whose radiative transfer codes tend to be *less* accurate), while 1D modelers can afford to use methods that are intrinsically more accurate than the k-distribution method.

For the application that follows in Paper II, we required accurate net radiative heating

rates throughout the stratosphere. In addition to Dr. Crisp's locally-available "quasi-random" code, RTMOD, and the correlated-k models of GWCC and Paper I, we tested the nationally-distributed programs of Keith Shine and Ming-Dah Chou. See Shine (1987); Chou, Ridgway, and Yan (1993); Chou and Kouvaris (1991). These were faster than the quasi-random model, in Chou's case by four orders of magnitude. Neither seemed to fulfill its promise of accurately calculating net radiative heating of stratospheric layers, but it's important to recognize that I was using these programs far from their implementors, and perhaps misusing them, so I cannot reach a firm conclusion. The quasi-random model also appeared to meet the requirements of accuracy as well as or better than the correlated-k program, with the advantage of being well integrated and frequently used.

Should an opportunity arise to develop the k-distribution technology further for a tropospheric application, I would participate with cautious optimism.

5. Theoretical advantage(?) of RTMOD over correlated-k

Yuk Yung and I have speculated on whether the "quasi-random" approach of RTMOD should or should not do better than the spectral sorting of correlated-k. It is uncertain whether the advantage of RTMOD in the tests done so far was a matter of principle, or a matter of implementation and code maturity.

The correlated-k method perhaps preserves a better representation of the spectral statistics for a particular pressure, temperature, and composition, than the "quasi-random" approach does. The efficiency of correlated-k disappears if every new pressure, temperature, and composition requires a new spectral calculation. The quasi-random model preserves the physical rather than the spectral statistics. RTMOD stores, for each spectral

interval, the number of lines of each gas that fit into particular linestrength intervals, together with the strength-weighted mean of their Lorentz widths at a standard temperature and pressure. The strengths, widths, and statistics can then be adjusted for a particular pressure, temperature, or composition, on the basis of known physical laws. In the case of correlated-k, an adjustment for a new pressure can only be done by interpolation, or by assuming that the lines fit some standard model such as a Malkmus distribution. But, N.B., correlated-k has yet to show an advantage over RTMOD even in the "pure" correlated-k tests where spectra are recalculated for each new pressure, temperature, and composition.

Finer spectral resolutions for correlated-k might profitably be pursued. The quasi-random model is currently storing histograms of linestrength for narrow 2-cm^{-1} intervals, even though the linestrength classes are calculated for 20-cm^{-1} intervals. Correlated-k at 2-cm^{-1} would be uselessly inefficient, but some compromise might be effective.

See Paper II and Appendix 2 for further discussions of RTMOD.

6. A simple application of correlated-k

The correlated-k method is adequate to a task recently suggested by Dr. Laszlo Keszthelyi, namely, calculating the radiative heating rate in the near-surface layers above a lava flow. A strong upper bound on the radiative heating rate Q (temperature per unit time) at an altitude z=1 m above the flow can be estimated from

$$Q \ll \frac{\sigma T_L^4}{\rho C_p(1\mathrm{m})} \approx 50 \frac{\mathrm{K}}{\mathrm{s}}, \tag{2}$$

and a more accurate radiative calculation will determine how much less. Here ρ and C_p are the atmospheric density and heat capacity, and T_L the lava temperature (assumed to be 1000 K in the above approximation).

We assume the lava field is wide enough to justify a plane-parallel model of the atmosphere, but narrow enough that the wind passes over it without appreciable change in the absorbing properties of the air. The result of such a calculation can be used to judge whether the second assumption can be met at various altitudes up to 200 m.

For the purpose of calculating absorption coefficients, the 200-m atmospheric surface layer is assumed to be at a constant pressure of 100.1 kPa, and a uniform temperature of 293.59 K. The molecular mixing ratios of water, CO_2, ozone, N_2O, methane, and O_2 are assumed to be 0.0181, 3.3 x 10^{-4}, 3.05 x 10^{-8}, 3.2 x 10^{-7}, 1.7 x 10^{-6}, and 0.209 respectively. Atmospheric spectra from 300 cm^{-1} to 4000 cm^{-1} were calculated from the HITRAN archive (7), using FASCOD (8,9,10), and reduced by the correlated-k method of Goody, West, Chen and Crisp (2). The k-distribution of the gas mixture was obtained from the spectrum of the gas mixture, not from the k-distributions of the component gases.

The lava flow is assumed to radiate as a black body at 500 K, 750 K, or 1000 K. Using a plane-parallel geometry, the spectral flux near the surface of the lava is $\pi B_\nu(T_L)$, where B_ν is the Planck function, and T_L the temperature of the lava. The attenuation of that flux is calculated without accounting for any redistribution of photons among the ten 20-m atmospheric slabs nearest the surface, or any emission by the air towards the lava. This approach would obviously be wrong for a lava flow at 293 K, which cannot heat a 293 K atmosphere, but considering that $(293/500)^4 = 12\%$, the approach introduces only a small positive error in the atmospheric heating induced by the 500 K lava, and negligible errors for the 750 K and 1000 K cases.

The density ρ and heat capacity C_p of the 200-m surface layer are treated as constants,

1.188 kg/m^3 and 1006 J kg^{-1}K^{-1} respectively. Then the heating rate Q_n (temperature per unit time) in the nth 20-m slab of this plane-parallel atmosphere is given by

$$Q_n = (F_n - F_{n+1})/[\rho C_p(z_n - z_{n-1})], \tag{3}$$

where F_n is the spectrally-integrated upwelling flux at the bottom of the nth layer, z_n the altitude at the top of the nth layer, and n increases upward. For a k-distribution calculation, the spectrum is divided into intervals of width $\Delta\nu$ that limit the variation of the Planck function, which is taken to be a constant $\bar{B}_i(T_L)$ in the ith such interval. A Gaussian quadrature from $G = 0$ to $G = 1$ integrates the fluxes within each wide interval, using 100 subintervals ΔG_j. See references (2) and (16). Let τ_j denote the optical thickness in the jth small interval, for each slab of fixed geometric thickness Δz. For a series of cool slabs near a hot radiating source, we consider only the absorption by the cool layers, so that

$$Q_n = \frac{\pi\Delta\nu}{\rho C_p \Delta z} \sum_i \bar{B}_i(T_L) \sum_j \{\exp[-\tau_j \Delta G_j (n-1)] - \exp[-\tau_j \Delta G_j n]\}. \tag{4}$$

In the case at hand, the $\Delta\nu$ was 25 cm^{-1}, the Δz was 20 m, so with some rearrangement,

$$Q_n = \frac{\pi(25\text{cm}^{-1})}{\rho C_p(20\text{m})} \sum_i 2\bar{B}_i(T_L) \sum_j \sinh\frac{\tau_j \Delta G_j}{2} \exp\frac{-\tau_j \Delta G_j (2n-1)}{2}. \tag{5}$$

The results were heating rates of about 0.01 K/s, 0.05 K/s, and 0.15 K/s at $z = 10$ m altitude for lava temperatures of 500, 750, and 1000 K respectively, with reductions of about 5% in the heating rates at 200 m altitude.

The calculation was not entirely repeated for different values of the water-vapor mixing ratio. Intuition suggests humidity is likely to be the most important additional variable, because the bending fundamental of water vapor occurs at 1595 cm^{-1}, while the peaks

of the Planck function for 500 K, 750 K, and 1000 K occur at 980, 1470, and 1960 cm^{-1} respectively. However, limited experimentation indicated that the heating is *not* a very strong function of humidity. Despite the strong self-broadening of water vapor lines, the dependence of Q on the water vapor concentration seems to be less than linear in the case at hand, suggesting that much of the heating is due to strong lines that saturate quickly (and to their wings, in the upper layers).

References

Reference (16) is Paper I above. Other reference numbers in this appendix point to the reference list in Paper I. In addition, this appendix references:

Chou, M.D. and L. Kouvaris, 1991: Calculations of transmission functions in the infrared CO_2 and O_3 bands. *J. Geophys. Res.* **96**, 9003–9012.

Chou, M.D., W.L. Ridgway, and M.M.H. Yan, 1993: One-parameter scaling and exponential sum fitting for water vapor and CO_2 transmission functions. *J. Atmos. Sci.* **50**, 2294–2303.

Keszthelyi, L.P., 1994: On the thermal budget of Pahoehoe flows. Ph.D. thesis, California Inst. of Tech.

Shine, K.P., 1987: The middle atmosphere in the absence of dynamical heat fluxes. *Quart. J. Roy. Met. Soc.* **113**, 603–633.

Zhu, Xun, 1994: On overlapping absorption of a gas mixture. Submitted to *J. Atmos. Sci.*.

Paper II: Radiative forcing of the stratosphere by SO_2 gas, silicate ash, and H_2SO_4 aerosols shortly after the 1982 eruptions of El Chichon

M. F. Gerstell, California Institute of Technology

Joy Crisp and David Crisp, Jet Propulsion Laboratory

ABSTRACT

The 1982 eruptions of El Chichon Volcano injected large quantities of sulfur dioxide gas and silicate ash into the stratosphere. Several studies have shown that the long-lived sulfuric acid aerosols derived from these volcanic effluents produced measurable changes in the radiative heating rates and the global circulation. The radiative and dynamical perturbations associated with the short-lived, but more-strongly-absorbing sulfur dioxide and ash clouds have received much less attention. We therefore used an atmospheric radiative transfer model and observations collected by satellites, aircraft, and ground-based observers to estimate the amplitudes of the stratospheric radiative heating rate perturbations produced by each of these components during the first few weeks after the El Chichon eruption. One week after the April 4, 1982 eruption, net radiative heating rate perturbations exceeding 20 Kelvin per day were found at altitudes near 26 km. The absorption of sunlight by the silicate ash accounts for the majority of this heating. The sulfur dioxide gas and sulfuric acid aerosols each produced net heating perturbations that never exceeded

2 Kelvin per day. In spite of the intense heating by the ash, observations indicate that stratospheric temperatures never increased by more than a few degrees Kelvin. We therefore concluded that this radiative heating was largely balanced by upwelling and adiabatic cooling. The amplitude and spatial extent of this upwelling was estimated with a diagnostic, two-dimensional dynamical model. The ash heating rates may have been balanced by a global enhancement in the stratospheric meridional circulation, with zonally-averaged upward velocities of about 1 cm/sec near the latitude of the plume. This enhanced stratospheric circulation persisted only for a few weeks, but it may have played a major role in the vertical and horizontal dispersal of the plume. The vertical transport needed to balance the heating by sulfur dioxide gas was only 5 to 10 percent as large, but this perturbation may have produced a 2-km increase in the altitude of the plume. These results suggest that the radiative forcing by the ash and the sulfur dioxide gas should be included in more comprehensive models of the plume evolution. They also suggest that particle size distributions inferred from ash fallout rates could be wrong if the upwelling associated with this radiative heating is not considered.

1. Introduction

Volcanic eruptions can inject large quantities of sulfur-bearing gases and silicate ash into the stratosphere. The sulfur gases (primarily SO_2 and H_2S) are the precursors of long-lived volcanic sulfate aerosols, whose effects on the stratospheric thermal structure and dynamics, and the tropospheric climate have been studied extensively (Angell and Korshover, 1983; Dutton and Christy, 1992; Fujita, 1985; Hansen *et al*, 1978; Wang and Lacis, 1978; Kiehl and Briegleb, 1993; Labitzke, Naujokat and McCormick, 1983; Newell, 1970; Parker and Brownscombe, 1983; Quiroz, 1983; Rind *et al*, 1992). A typical finding is that the radiative and dynamical forcing by the aerosols produces warming in the lower stratosphere on a time scale of months, with cooling of the tropospheric climate after a longer period, if the aerosols persist. The silicate ash and SO_2 gas injected into the stratosphere by a major volcanic eruption should also produce significant changes in the radiative forcing, because these constituents are more effective absorbers of solar and thermal radiation than the sulfuric acid aerosols. The radiative and dynamical effects of ash and SO_2 at stratospheric levels has received little attention, because unlike the H_2SO_4 aerosols, which can persist for years, the stratospheric residence time of these constituents is usually limited to weeks or a few months. The radiative and dynamical forcing by these constituents is therefore unlikely to have a long-term impact on the tropospheric or stratospheric climate. This forcing could still have a significant influence on the early evolution and dispersal of the volcanic plume. Observations acquired soon after the 1982

eruptions of El Chichon Volcano provide the data needed to assess the relative effects of the ash, SO_2, and H_2SO_4 aerosols on the stratospheric radiative heating rates and circulation. El Chichon Volcano (17.3°N, 93.2°W) erupted several times during March and April, 1982. The final and largest eruption occurred on April 4. Vupputuri and Blanchet (1984) and Pollack and Ackerman (1983) estimated maximum stratospheric solar heating rates of 4.5 to 7.5 K/day for the silicate ash from El Chichon, but their study focused on a period extending 3 to 6 months after the eruption, when the majority of the ash had fallen out of the stratosphere. In the present study, we used a comprehensive atmospheric radiative transfer model to estimate the solar and thermal radiative effects of silicate ash and the SO_2 gas for conditions like those observed during the first month after the April 1982 eruption of El Chichon Volcano, before the H_2SO_4 aerosol cloud fully developed. These effects were compared to those produced by the fully-developed H_2SO_4 cloud. We found that even though the SO_2 and ash produced stratospheric heating perturbations that were short-lived and more localized than those caused by the H_2SO_4 aerosols, their radiative forcing immediately after the eruption was sufficiently intense to have a strong influence on the vertical and horizontal dispersal of the volcanic plume. In the densest regions of the volcanic plume, at altitudes near 26 km, the solar radiative heating by the ash may have been an order of magnitude stronger than that by SO_2 gas (or the fully-developed H_2SO_4 aerosol cloud), and more than 20 times larger than the background net radiative heating in the lower stratosphere. In spite of this intense heating, no large temperature increases were observed within the plume (Angell and Korshover, 1983). We therefore concluded that the strong radiative heating was largely balanced by the adiabatic expansion

and cooling associated with enhanced upwelling. The intensity and spatial extent of the upwelling needed to balance this heating perturbation was estimated with a stratospheric meridional circulation model based on the Eulerian-mean residual formulation (Santee and Crisp, 1994). The derived upward velocities within the densest part of the plume were comparable to the average fall speeds of the ash particles. Thus, distributions of ash size or density inferred from theoretical fall velocities are likely to be wrong if the buoyancy associated with direct solar heating of the ash is neglected.

Section 2 describes the meridional circulation model, radiative transfer model, and background climatologies adopted here. Section 3 shows the perturbations of stratospheric net heating rates and the circulation needed to balance the direct radiative forcing by the sulfate aerosols. These results provide a comparison standard for the heating by the SO_2 gas and silicate ash. Section 4 quantifies the radiative effects of the SO_2, and Section 5 quantifies the radiative effects of the silicate ash. Section 6 is a summary of our findings.

2. Model descriptions

(a) Radiative transfer model

The computation of net radiative heating and cooling rates requires a detailed representation of the flux distribution throughout the atmosphere. Crisp (1986, 1989, 1990) has developed fast, accurate methods for finding radiative fluxes and heating rates in scattering and absorbing planetary atmospheres. These methods have been combined in a comprehensive radiative transfer model that accommodates all radiative processes known to be important in the terrestrial atmosphere, including absorption, emission, and multiple

scattering by gases and airborne dust particles.

A multiple-scattering model based on the multi-level delta-Eddington/adding method (Crisp, 1986) was used to find solar fluxes and heating rates in a vertically-inhomogeneous, plane-parallel atmosphere. Because this approach for evaluating the equation of transfer assumes that Beer's law is satisfied at all points along the optical path (i.e. the optical depth varies linearly with absorber amount) it is strictly valid only in spectral regions sufficiently narrow that the optical properties do not vary substantially across each. This method should therefore provide reliable results in moderately-wide spectral intervals at ultraviolet and visible wavelengths, where extinction (absorption and scattering) is contributed by airborne ash, H_2SO_4 aerosols, Rayleigh scattering, and electronic or photolytic absorption bands of gases (H_2O, CO_2, O_3, N_2O, CO, CH_4, O_2, SO_2, NO_2), since the optical properties of these constituents vary slowly with wavelength. This method is also valid in near-infrared spectral regions occupied by very weak water and carbon dioxide lines, whose cores are not saturated for realistic atmospheric optical paths.

This approach for evaluating the equation of transfer is not strictly valid within broad spectral regions occupied by strong near-infrared gas vibration-rotation bands, because the gas absorption coefficients vary rapidly with wavelength in these intervals, and the broadband absorption does not satisfy Beer's law. For these spectral regions, we tested two approaches for evaluating the equation of transfer. In the first, we returned to the two-stream nonscattering model described by Crisp (1990). The broadband gas absorption within vibration-rotation bands was evaluated using a Voigt quasi-random model (Crisp, 1990; Santee and Crisp, 1994). H_2SO_4 aerosol and silicate ash absorption was also included

at these wavelengths (by adding the aerosol and ash absorption optical depth to that of the gas), but multiple scattering was neglected. In the second approach, we simply ignored the violation of Beer's law and used the multiple scattering model. To estimate the absorption by gases in this model, the Voigt quasi-random model was first used to evaluate the gas transmission between the top of the atmosphere and each atmospheric level in 20 to 200 cm^{-1} wide spectral regions. These transmission values were then inverted to yield the effective wavelength-averaged gas optical depth in each atmospheric layer. These results were combined with the gas continuum and aerosol absorption optical depths to yield the total absorption optical depth. Finally, the absorption optical depths were combined with the Rayleigh and aerosol scattering optical depths to yield the total extinction optical depth and single scattering albedo in that spectral interval (cf. Crisp, 1986). These two methods were tested against rigorous line-by-line multiple scattering calculations performed with a multi-stream discrete ordinate model (Stamnes *et al*, 1988; Bell and Crisp, 1993). Both approximate methods produced similar results for clear-sky conditions, with heating rate errors rarely exceeding 5%. The second method usually produced fluxes and heating rates that were more accurate for cloudy or aerosol-laden atmospheres. We therefore selected the second approach for the calculations presented here. The thermal radiative transfer model used here includes absorption by gases and the absorption by airborne ash and aerosols, but neglects multiple scattering. This simplified approach was adopted because the single-scattering albedos of the H_2SO_4 aerosol and ash particles are small (less than 0.2) at thermal wavelengths. The Voigt quasi-random model (Crisp 1989, 1990) is used to find the broadband gas transmission functions in spectral intervals that were 2 cm^{-1} wide.

The solution to the equation of transfer is identical to that described in Crisp (1989), equations (5)–(9), except that we have added the surface boundary condition given in Crisp (1990, equation 14). The atmosphere was resolved into 60 vertical layers between the surface, at 1013 mbar, and the 0.178 mbar level. The levels defining the boundaries of each layer were equally spaced in the logarithm of pressure and characterized by a pressure, a temperature, the gas mixing ratios for eight gases, (H_2O, CO_2, O_3, N_2O, CH_4, O_2, NO_2, SO_2) and the optical thickness for each of aerosol particle type (H_2O, H_2SO_4, silicate ash). The aerosol particle number density was assumed to be constant within each layer. The temperatures and gas mixing ratios were assumed to vary linearly with log pressure between the top and bottom of each layer. The solar spectrum was divided into 755 spectral intervals between 0.125 and 5.26 μm to resolve the wavelength dependence of the solar flux and that of gas and dust absorption features. The spectrally-dependent solar fluxes above the atmosphere at wavelengths between 0.125 and 0.8 μm are those of the World Meteorological Organization (1986); outside this wavelength range we used the data of Thekaekara (1969). The thermal spectrum was divided into 95 spectral intervals between 5.26 and 200 μm to resolve the wavelength dependence of the Planck function and various gas and aerosol absorption bands. Spectral intervals occupied by infrared gas vibration-rotation bands were further subdivided into 2–cm^{-1} intervals to improve the accuracy of the multiplicative property of narrow-band transmission (Goody and Yung, 1989), which is used to combine the effects of two or more gases that absorb in the same spectral interval.

The absorption line parameters for gases at infrared wavelengths were taken from

the 1992 edition of the HITRAN database (Rothman *et al*, 1992). The gas absorption cross sections at ultraviolet and visible wavelengths were taken from DeMore *et al* (1992). Wavelength-dependent extinction, absorption, and scattering cross-sections and scattering phase functions for liquid water droplets, H_2SO_4 aerosols, and silicate ash particles were derived from the refractive index data for these aerosols with a model that incorporates the Mie-scattering algorithm of Wiscombe (1980; personal communication, 1992), with the methods for integrating over particle size distributions described by Hansen and Travis (1974). The wavelength-dependent refractive indices for liquid water were taken from Hale and Querry (1973). Cloud particle size distributions for altostratus and stratus clouds were taken from Hansen (1971). Because Mie scattering is not appropriate for evaluating the optical properties of the non-spherical ice particles that compose cirrus clouds, we adopted published values of the wavelength-dependent optical properties of columnar ice crystals (Freeman and Liou, 1979). For the H_2SO_4 aerosols, the real and imaginary components of the wavelength-dependent refractive index of 75% sulfuric acid solution were taken from Palmer and Williams (1975). A single log-normal size distribution (cf. Eqn. (2.60) of Hansen and Travis, 1974) was used at all latitudes. The geometric mean particle radius (r_g in Hansen and Travis, 1974) was assumed to be 0.4 μm, and the geometric standard deviation with respect to the natural logarithm of particle radius (σ in Hansen and Travis, 1974) was assumed to be 0.34 μm (cf. Pollack *et al*, 1991; Bandeen and Fraser, 1982; Oberbeck *et al*, 1983). The Chichon ash was composed of andesitic glass and crystals (MacKinnon *et al*, 1984). For our calculations, we used the optical properties of crystalline andesite (Pollack *et al*, 1973). Sensitivity experiments on rhyolite and basalt

glasses suggest that omitting the optical properties of the andesite glass may produce net radiative heating rates that are up to 20% too large, but the optical properties of andesitic glass were not available. The nominal mean radius of the stratospheric ash particles was assumed to be 3 μm one week after the eruption. Alternate distributions with mean radii of 1 and 5 μm were also used. These particle radii are roughly consistent with aircraft observations, which indicate a median radius of 6 μm as late as May 7, for all collected particles larger than 2 μm (MacKinnon *et al*, 1984). The geometric standard deviations of all ash size distributions, with respect to the natural logarithm of the radius, were assumed to be σ=0.16 μm, consistent with measurements of the ash acquired in September, 1982 (Oberbeck *et al*, 1983).

This radiative transfer model was used to find the diurnally-averaged solar heating rates, thermal cooling rates, and net radiative heating rates at 19 latitudes including the poles, with an increment of 10° of latitude. The solar fluxes and heating rates for each latitude were evaluated at four solar zenith angles, and these results were integrated over the solar day to obtain the diurnally-averaged solar heating rates. Thermal radiances were obtained for two streams (one up, one down); a diffusivity factor of 1.66 (Elsasser, 1943) was used to obtain the upward and downward thermal fluxes and cooling rates at each model level. Finally, the net heating rates at each latitude and altitude were obtained by differencing the solar heating rates and thermal cooling rates.

(b) Meridional circulation model

Given estimates of the thermal structure and net radiative heating rates at stratospher-

ic levels, the net meridional transport can be derived diagnostically from the transformed Eulerian-mean (TEM) equations of motion (Andrews and McIntyre, 1976; Dunkerton, 1978; Shia *et al*, 1989; Santee, 1992). This approach is widely used in stratospheric chemical tracer transport studies, because it incorporates the almost equal, but opposing, effects on planetary scale waves and the zonal-mean meridional circulation, to yield a direct estimate of the net, Lagrangian-mean mass and heat transports. This approach is most valid at altitudes within the middle and lower stratosphere, where the waves are approximately linear and time-invariant. In the TEM approach, the residual, zonal-mean meridional and vertical velocities, $v^\star$, $w^\star$, are defined through the transformation:

$$v^\star \equiv \bar{v} - \frac{1}{\rho}\frac{\partial}{\partial z}\left(\frac{\rho\overline{v'T'}}{\frac{\partial\bar{T}}{\partial z}+\frac{g}{c_p}}\right) \tag{1}$$

$$w^\star \equiv \bar{w} + \frac{1}{a\cos\phi}\frac{\partial}{\partial\phi}\left(\frac{\overline{v'T'}\cos\phi}{\frac{\partial\bar{T}}{\partial z}+\frac{g}{c_p}}\right), \tag{2}$$

where $\bar{v}$ and $\bar{w}$ are the zonal–mean velocity components in the meridional and vertical directions, respectively, a is the radius of the earth, z the log-pressure altitude, ρ is the atmospheric density, g is the gravitational acceleration, ϕ is latitude, and c_p is the specific heat at constant pressure. The $\overline{v'T'}$ term describes the eddy heat flux. When these definitions are substituted into the zonally-averaged primitive equations, the mass continuity and thermodynamic energy equations take the form [Andrews, Holton, and Leovy, 1987]:

$$\frac{1}{a\cos\phi}\frac{\partial}{\partial\phi}\left(v^\star\cos\phi\right)+\frac{1}{\rho}\frac{\partial}{\partial z}\left(\rho w^\star\right) = \frac{\partial\rho}{\partial t} \approx 0 \tag{3}$$

$$\frac{\partial\bar{T}}{\partial t}+\frac{v^\star}{a}\frac{\partial\bar{T}}{\partial\phi}+w^\star\left[\frac{\partial\bar{T}}{\partial z}+\frac{g}{c_p}\right]-\bar{Q} = -\frac{1}{\rho}\frac{\partial}{\partial z}\left[\frac{\rho\overline{v'T'}\frac{\partial\bar{Q}}{\partial\phi}}{a\left(\frac{\partial\bar{T}}{\partial z}+\frac{g}{c_p}\right)}+\rho\overline{w'T'}\right], \tag{4}$$

where H is a mean scale height, $\bar{T}$ is the zonal-mean temperature, and $\bar{Q}$ is the zonal-mean (diurnally-averaged) net diabatic heating rate. The term on the right-hand side of the thermodynamic energy equation (Eq. 4) is called the "wave heating" term. This term vanishes for quasi-geostrophic motions, and for steady, conservative gravity waves, and is usually neglected. In addition, at stratospheric levels, radiative heating and cooling rates dominate the net diabatic heating, so that $\bar{Q}$ reduces to the net radiative heating. Finally, if we neglect $\partial\rho/\partial t$ and $\partial\bar{T}/\partial t$ in Eqs. 3 and 4, these two equations can be solved simultaneously in terms of the steady-state TEM streamfunction, ψ (Shia *et al*, 1989):

$$\left(\frac{\psi}{H} - \frac{\partial\psi}{\partial z}\right)\frac{\partial\bar{T}}{\partial\phi} + \left(\frac{\partial\bar{T}}{\partial z} + \frac{g}{c_p}\right)\frac{\partial\psi}{\partial\phi} = \bar{Q}a\ cos\ \phi. \tag{5}$$

This equation describes the net steady-state meridional circulation that transports enough heat to maintain the observed thermal structure in the presence of the imposed net radiative heating rate. It should be interpreted as a diagnostic statement of balance, rather than a mechanistic model of the processes producing the circulation. In other words, even though this equation describes a circulation consistent with the observed radiative heating field, it does not require that the circulation be forced directly by that heating. In many studies (e.g., Dunkerton, 1978; Rosenfield *et al*, 1987; Gille *et al*, 1987), Eq. 4 is simplified further by neglecting the second term on the left-hand side, which accounts for horizontal advection of heat. The thermodynamic energy equation then reduces to the form:

$$w^\star\left[\frac{\partial\bar{T}}{\partial z} + \frac{g}{c_p}\right] \approx \bar{Q}\,. \tag{6}$$

This approximation was not adopted here, but the simple expression in Eq. 6 more

clearly illustrates the linear relationship between the TEM vertical velocity, $w^{\star}$, and the net radiative heating rates, $\bar{Q}$. The numerical methods used to solve Eq. 5 are described in detail in Santee (1993) and Santee and Crisp (1994).

(c) Background atmospheres and surfaces

The fractional cloudiness and cloud-top pressures for tropospheric water clouds were derived by averaging the 1984-86 values for each latitude and month as reported by the International Satellite Cloud Climatology Project (ISCCP; see Rossow and Schiffer, 1991). ISCCP data are not available for 1982, the year of El Chichon's eruption. All high clouds were modeled as cirrus clouds composed of ice crystals, with an optical thickness of 1.5 at 0.425 μm; all middle-altitude clouds were assumed to be altostratus, with an optical thickness 5 at 0.425 μm; all low-level clouds were modeled as stratus with an optical thickness of 10 at 0.425 μm.

Climatological temperature profiles at each latitude for April and July were obtained by averaging National Meteorological Center (NMC) data collected in 1984-86 (Gelman *et al*, 1986). Eight absorbing gases were included in our background atmospheres. The volume mixing ratios of O_2 and CO_2 were assumed to be constant, at 0.21 and 0.00033. Climatological O_3 profiles were obtained by averaging the Solar Backscatter Ultraviolet (SBUV) data from 1984-1986 for each latitude and month. The 1984-86 period was chosen for consistency with available ISCCP data, even though NMC and SBUV data from the Chichon period could have been used. Stratospheric O_3 abundances in the south polar regions, where SBUV data were not available, were obtained from the 1986 balloon data

described by Komhyr *et al* (1989). Stratospheric profiles of H_2O, N_2O, CH_4, and NO_2 for each latitude and month were derived from Nimbus-7 LIMS and SAMS measurements and (for H_2O) ground-based microwave data. The sulfur dioxide profile for the unperturbed atmosphere was taken from Warneck (1988, Fig. 3-13). Tropospheric H_2O mixing ratios were derived from climatological specific humidity data (Oort, 1983). The mixing ratios of other gases at tropospheric levels were estimated by extrapolating stratospheric values to the surface, assuming the logarithm of the mixing ratio decreased linearly with the logarithm of pressure.

Surface albedos at visible wavelengths for each latitude and month were also taken from the ISCCP database. At near-infrared wavelengths, we adopted the approach described by Briegleb (1992) and assumed that the ratio of near-infrared albedo to visible albedo depends on surface type (snow, ice, water, vegetation, etc.). Meridional distributions of 12 surface types were obtained from the Goddard Institute for Space Studies database (see Matthews, 1983). The visible albedos given by ISCCP were extrapolated into the ultraviolet, to 0.2 μm, and set to zero at shorter wavelengths. Surface albedos at thermal infrared wavelengths were assumed to be zero for dry land. For snow, values were taken from Warren (1982). For the ocean, the albedos were calculated directly from the optical constants of seawater, with the aid of a Fresnel facet model for rough surfaces. This model explicitly includes the effects of increased sea-surface roughness as one goes from the tropics to high latitudes.

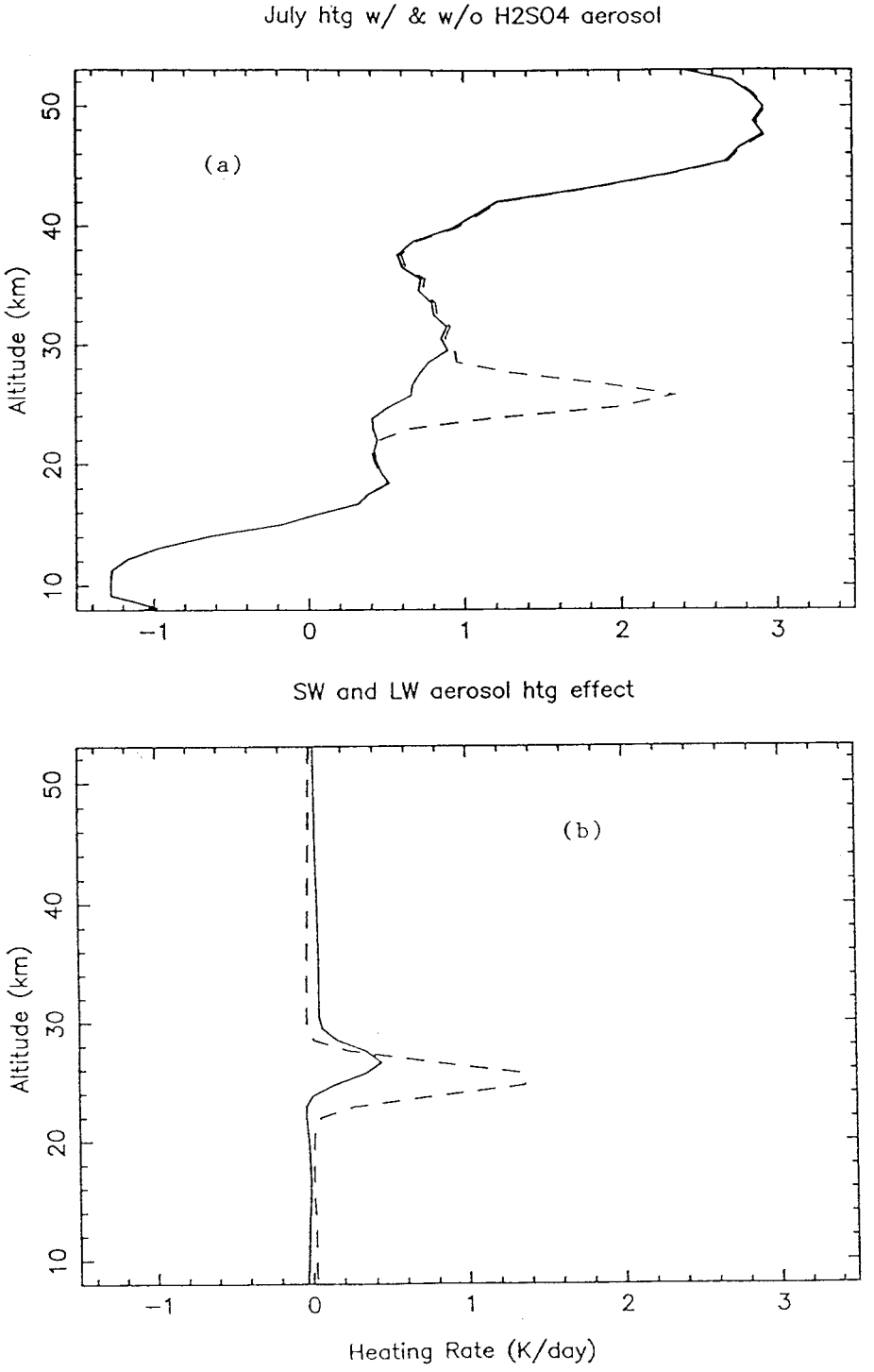

Fig. 1 Above: diurnal average radiative heating rates for a typical July climate at 20°N, with a clear sky (solid curve) and with a sulfuric acid aerosol layer (dashes) as described in the text. Below: short-wave (solid) and long-wave (dashes) components of the difference between the aerosol heating rate and the clear-sky heating rate.

3. Sulfuric Acid Aerosols

Net radiative heating rates and diabatic streamfunctions were derived for two reference atmospheres. The first included only the climatological gas and cloud distributions described in the previous section. The second used this background climatology, but also included an H_2SO_4 aerosol cloud with latitude-dependent column optical depths similar to those measured by the Solar Mesosphere Explorer (SME) several months after the eruption of El Chichon (see Eparvier *et al*, 1994; Thomas *et al*, 1983). The same aerosol vertical profile was used at all latitudes. This profile was derived from observations acquired near 20°N in early July, 1982. It assumes a Gaussian distribution of spherical particles with number densities peaked at 26 km, and a half-width-at-half-max of 1.5 km (DeLuisi *et al*, 1983; Shibata *et al*, 1984; Oberbeck *et al*, 1983; Labitzke *et al*, 1983).

The diurnal-average net radiative heating profile at 20°N for the background climatology and the H_2SO_4 aerosol–laden atmosphere are shown in Fig. 1a. The net radiative heating by the aerosols is most intense at the 26 km level, at latitudes between the equator and 40°N, where the aerosols are most concentrated. The solar and thermal contributions to the net heating by the H_2SO_4 aerosol clouds are compared in Figure 1b. These results confirm the findings of other investigators (Young *et al*, 1994, and its references), that the radiative perturbation by H_2SO_4 aerosol is mainly due to the absorption of upwelling thermal radiation emitted by the surface and lower troposphere. The majority of the absorption of solar radiation by the H_2SO_4 aerosols occurs at wavelengths longer than 3 μm, where these aerosols have very low single scattering albedos.

The net radiative heating by the H_2SO_4 aerosols never exceeds 2 K/day, but this

heating could still produce significant stratospheric temperature increases over the lifetime of the aerosol cloud if it were not balanced by horizontal or vertical transport. The amplitude of the transport needed to balance this heating was estimated with the TEM model described in Section 2.2. The derived stratospheric streamfunctions for the baseline climatology and the aerosol-laden atmospheres are compared in Figs. 2a and 2b. We found that the net heating by the aerosols could be balanced by intensified upwelling (≈ 0.5 mm/s) at low latitudes near 26 km altitude, where the aerosol concentrations and heating rates are largest. This upwelling is associated with the formation of a weak meridional circulation cell in the northern hemisphere.

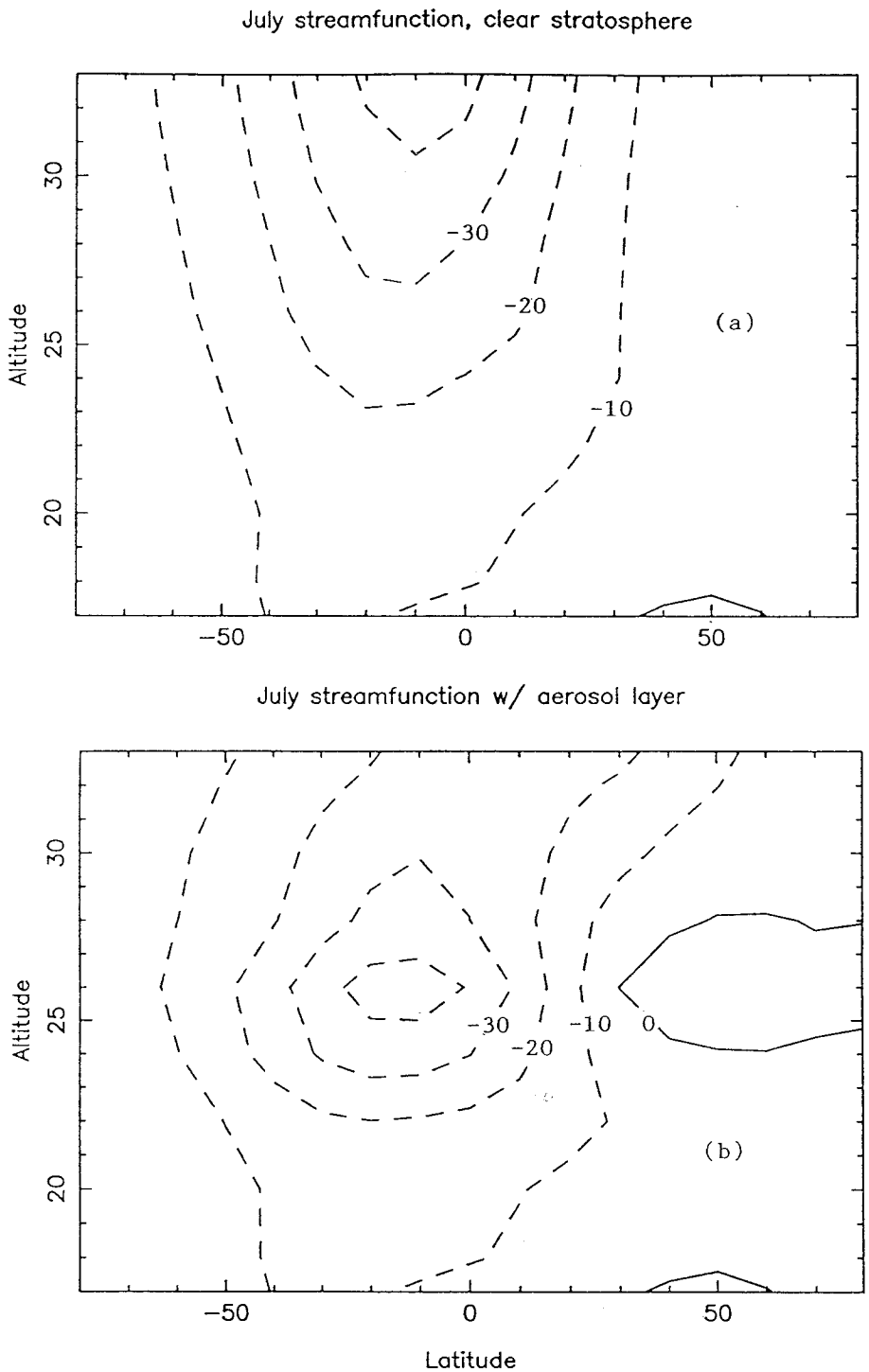

Fig. 2 Above: streamfunction of the meridional circulation for a typical July climate with only tropospheric water clouds. Units are 100 m^2/s, intervals 1000 m^2/s. Below: the same, with a sulfuric acid aerosol layer as described in the text.

4. Sulfur Dioxide Gas

The similarity between SO_2 and O_3 absorption spectra at ultraviolet wavelengths (Fig. 3) suggests that volcanic SO_2 should produce significant perturbations of the solar heating rates. The largest heating rate perturbations should occur where the SO_2 concentrations exceed the ozone concentrations, as they did near the center of El Chichon's eruption plume. The Total Ozone Mapping Spectrometer (TOMS) acquired approximately 100,000 measurements of the SO_2 column abundances each day (Krueger, 1983). We used the TOMS data for April 4, 5, 6, 12, 19, and 26, 1982. The 3° by 3° field of view of this instrument is stepped to 35 cross-track positions every 8 seconds as the spacecraft follows a sun-synchronous, noon-midnight polar orbit. The spatial resolution at the nadir is 50 by 50 km, and increases to 150 by 300 km at the far scan positions. Krueger (1983) estimated average SO_2 column amounts near 42 Dobson units (m atm cm) inside a volcanic cloud whose area was 3.3 x 10^6 km on April 6, 1982. Peak SO_2 column amounts of 750 DU were observed during the 24 hours immediately following the April 4, 1982 eruption.

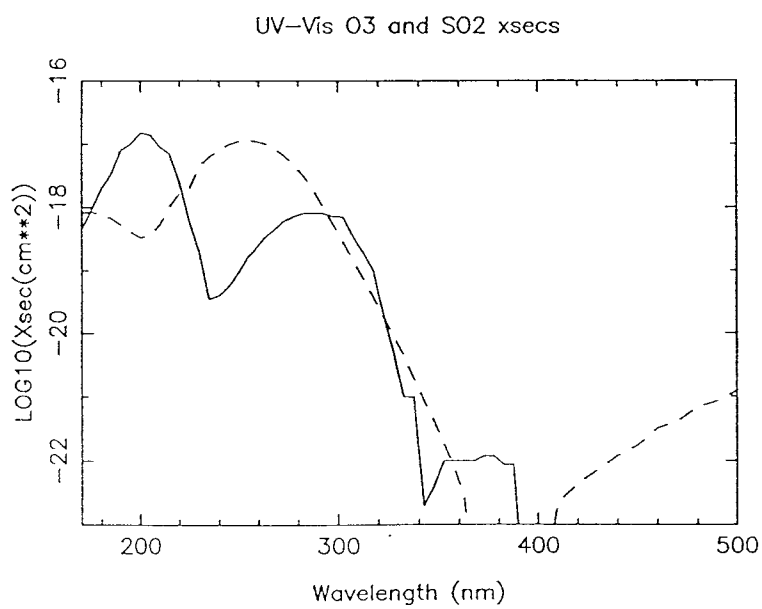

Fig. 3 Absorption cross-sections of ozone (dashes) and sulfur dioxide (solid) at ultraviolet and visible wavelengths, derived from Demore et al (1992).

We performed a series of sensitivity tests to quantify the effects of SO_2 absorption on the net heating rates. In these tests, we assumed that the SO_2 was concentrated in a plume with a Gaussian vertical profile, with a vertical half-width-at-half-max of 1.5 km. Even though SO_2 absorbs strongly at both solar and thermal wavelengths, its effect on the net radiative heating is dominated by the absorption of sunlight. For a given SO_2 column abundance, the solar heating rate perturbation increased as the altitude of the peak of the SO_2 plume increased (Fig. 4). The maximum solar heating rates were produced when the maximum SO_2 concentrations were near 30 km, where this gas begins to escape the shading by the O_3. When the peak SO_2 concentrations occur at higher altitudes, the absorption of sunlight by this gas continues to increase, but the total heating peak is reduced, because ozone absorption no longer contributes much to the total heating.

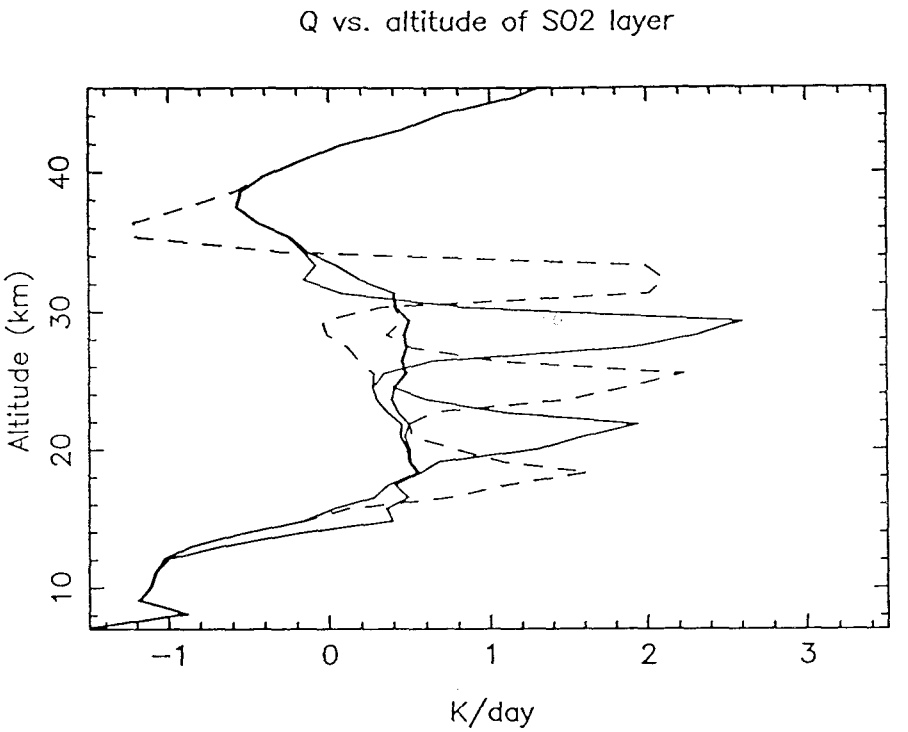

Fig. 4 Diurnal average radiative heating rates for a typical April climate with a sulfur dioxide layer (100 DU) centered at 34 km, 26 km, 16 km (all dashes); 30 km, 22 km, 10 km (all solid).

Just after the April 4, 1982 eruption of El Chichon, the largest SO_2 concentrations probably occurred within the ash cloud. This cloud was centered near 26 km altitude on April 10 (DeLuisi *et al*, 1983). The amplitude of the heating rate perturbation produced at this altitude for a 42 DU sulfur dioxide layer was slightly larger than that produced by the H_2SO_4 aerosol layer described in the previous section. The large SO_2 abundances extended over a much more limited area than the H_2SO_4 aerosols, however. If the derived SO_2 radiative forcing were averaged over a 10° wide zonal band, and used to create an analog of Fig. 2b, the resulting streamfunction would be almost indistinguishable from that obtained in the unperturbed case.

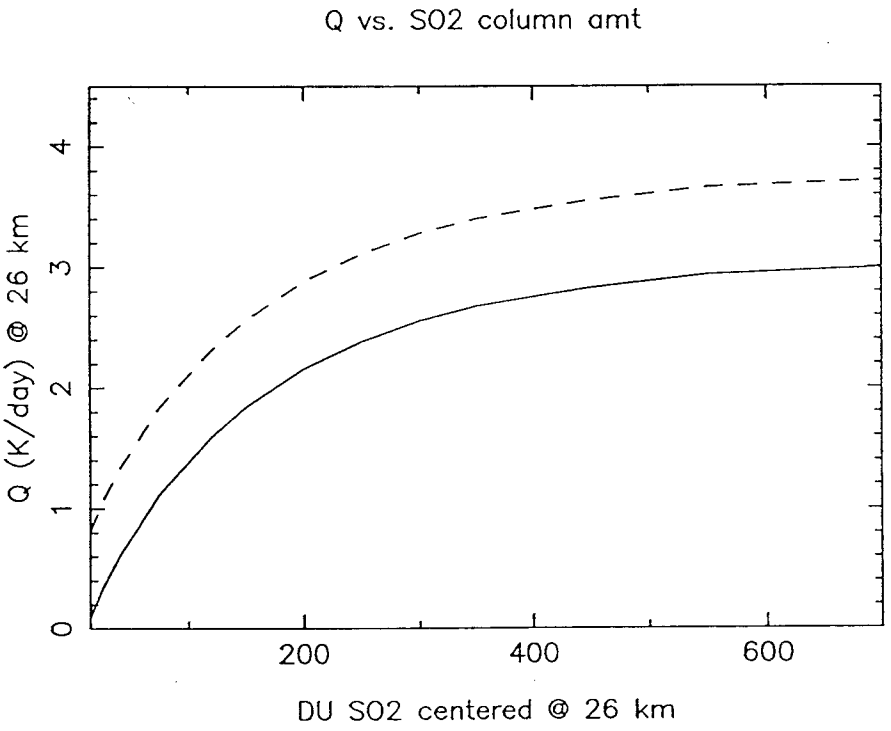

Fig. 5 Diurnal average radiative heating rate at the peak of a sulfur dioxide layer centered at 26 km altitude. The heating rate is shown as a function of the total column amount of sulfur dioxide. Dashes: total heating for a 7-gas atmosphere including the volcanic sulfur dioxide layer. Dots: excess over the typical April net heating at 26 km altitude with unperturbed sulfur dioxide. Graph begins at 15 DU, our threshhold for recognizing perturbed SO_2 in the TOMS data.

In spite of their limited spatial extent, SO_2 concentrations as large as those seen near the center of the El Chichon plume could have a considerable effect on the height of the volcanic plume. To illustrate this, Eq. 6 can be rearranged to yield an expression for the elevation change, ΔZ, associated with the net heating, Q:

$$\Delta Z = S^{-1} \int Q \, dt, \tag{7}$$

where t is time Q the radiative heating rate, and S ($= dT/dz + g/C_p$) is about 12 K/km at 26 km altitude, at 20°N in the springtime.

The amplitude of the radiative heating for an SO_2 plume centered at 25-26 km altitude is shown as a function of the SO_2 column amount in Fig. 5. The lower curve shows the amplitude of the heating rate perturbation for this latitude, altitude, and season calculated with respect to a background atmosphere with an unperturbed SO_2 abundance. Maximum SO_2 column amounts in the TOMS data were approximately 750, 200, 50, and 30 DU on April 4, 6, 12, and 26 respectively. Using these values, and integrating Eq. 7 over time, we find ΔZ for that part of the atmosphere where the SO_2 concentration are largest to be about 2 km during April—doubling the rise due to the Brewer-Dobson circulation at this latitude and season.

Another way to assess the magnitude of the radiative forcing by SO_2 gas is to compare the total energy it transfers into the 23-27 km layer to that deposited in the atmosphere by the erupted volcanic solids. A rough upper limit on the latter is 0.8 EJ (1 EJ = 10^{18}J), using an estimate of 0.4 km^3 magma (Rampino *et al*, 1988), magma density of 2600 kg m^{-3}, a heat capacity of 1000 J kg^{-1} K^{-1} (Peck, 1978), a magma temperature of 810°C (Rye *et al*, 1984; Luhr, 1990), which cools to about 20°C since most of it remains near the

ground or quickly falls back to the ground, in the tropics.

The excess solar energy absorbed by the SO_2 layer, compared to that usually absorbed at this latitude, altitude, and season, can be estimated from the heating rates shown in Fig. 5 (lower curve) and the TOMS SO_2 maps. For April 5, 12, 19, and 26, we find excess energy deposition rates of 0.32, 0.27, 0.14, and 0.03 EJ/day, for a time-integrated total of 4 – 5 EJ. Thus, the energy collected in the middle stratosphere by the SO_2 plume during the first few weeks following the eruption may have been at least as great as the energy delivered to the atmosphere by the erupted solids.

5. Silicate Ash

DeLuisi *et al* (1983) measured optical depths exceeding 0.7 (at 425 nm) at Mauna Loa on two dates in mid-April, 1982. Because little H_2SO_4 aerosol would have formed in the first week after the eruption (e.g., Turco *et al*, 1983), the measured optical thickness was attributed mainly to silicate ash. We therefore adopted an ash optical thickness of 0.6 for the sensitivity tests presented here. We assumed that the ash layer was centered at 26 km, and had a vertical half–width–at–half–maximum of 1.5 km. This is roughly consistent with lidar backscatter observations over Mauna Loa, which revealed a peak at 25 km altitude for a few days following the April 9 arrival of the eruption plume from El Chichon (Coulson *et al*, 1982).

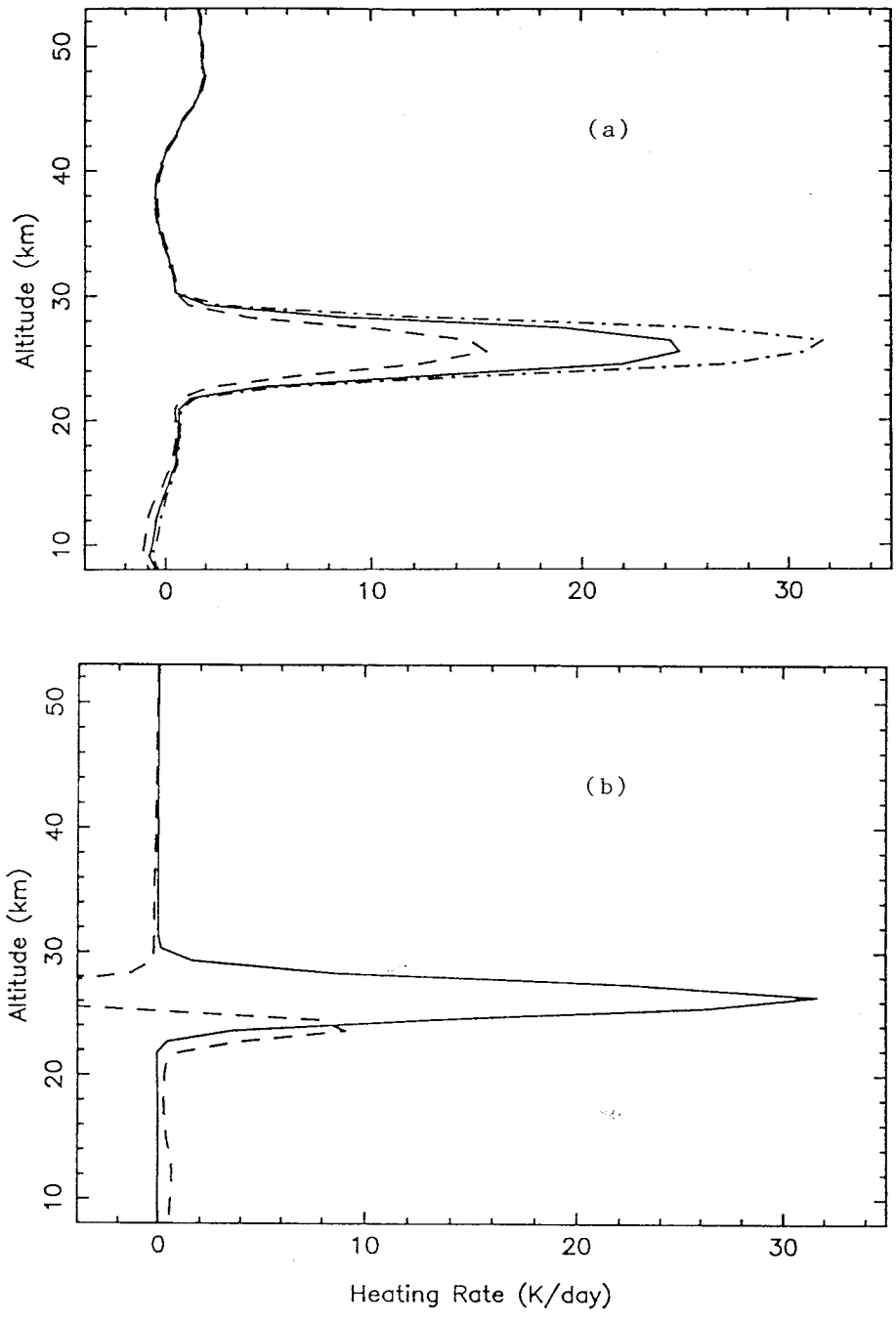

Fig. 6 Above: diurnal average radiative heating rate profile for a typical April atmosphere after injection of an ash layer described in the text, $\tau = 0.6$ in each case. In the range of particle radii shown, the peak heating rate increases monotonically with particle size. Mean radii of 1 μm (dashes), 3 μm (solid), 5 μm (dot-dash). Below: Short-wave (solid) and long-wave (dashes) components of the difference between 3μm ash heating and clear-sky heating. Ash optical properties in all cases are those of crystalline andesite.

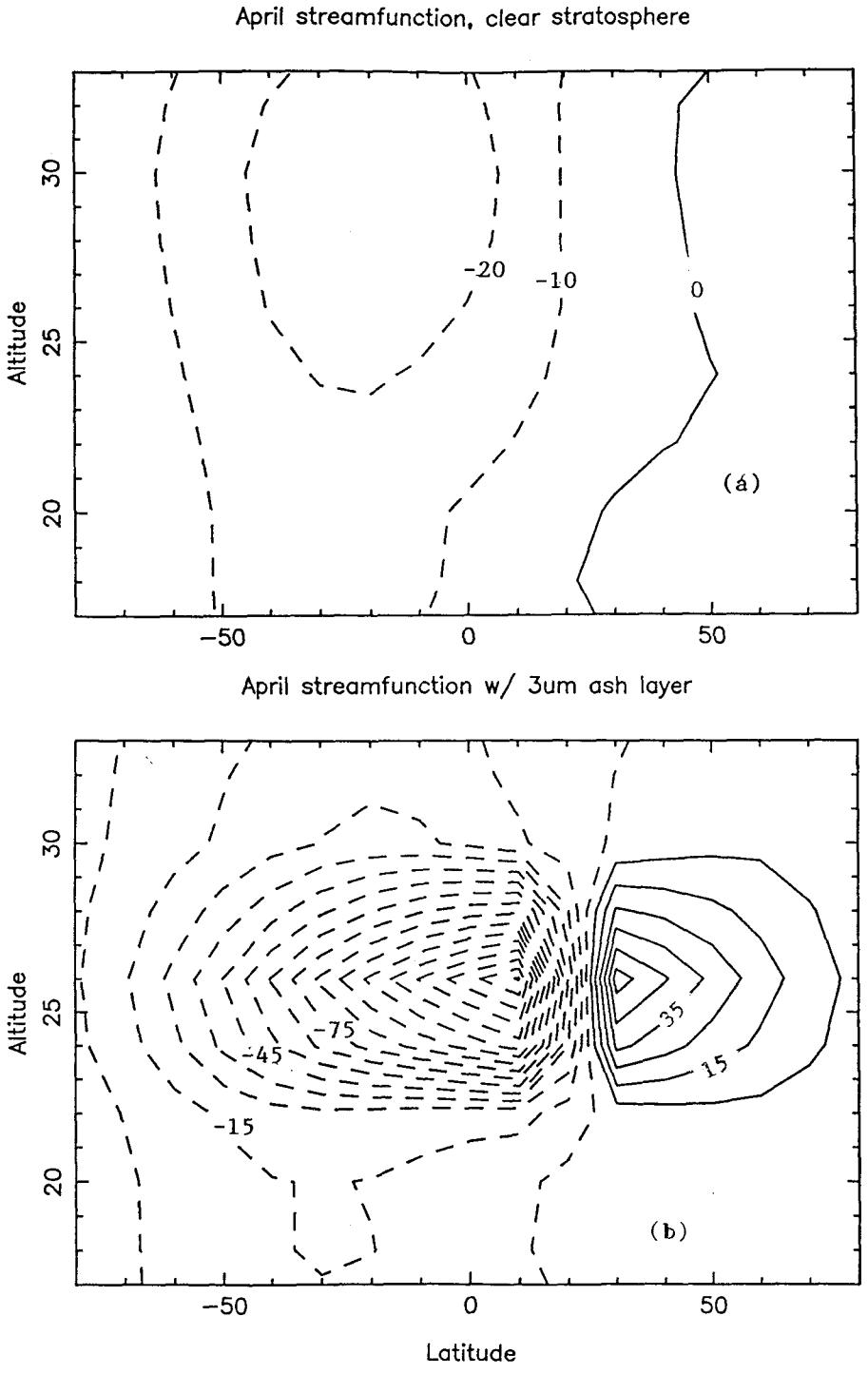

Fig. 7 Above: streamfunction of the meridional circulation for a typical April climate with only tropospheric water clouds. Units are 100 m^2/s, intervals 1000 m^2/s. Below: the same, after injection of a layer of 3-μm andesite dust particles as described in the text.

The solar, thermal, and net radiative heating rates produced by this ash layer are shown in Fig 6. We found that this ash plume produces a radiative perturbation that is about an order of magnitude larger than that caused by the SO_2 gas or the H_2SO_4 aerosol plumes described above. The amplitude of the ash heating is very sensitive to the mean particle radius (Fig. 6a), which is uncertain for the eruption of El Chichon. For the nominal 3-μm distribution, the heating rates can exceed 23 K/day. This radiative perturbation by silicate ash is due mainly to an increase of solar heating, with a smaller contribution from a reduction in thermal cooling (Fig. 6b).

The large radiative heating rates associated with the ash cloud should produce dramatic changes in the stratospheric thermal structure or dynamics. Monthly-averaged NMC temperatures measured at altitudes near 26 km between 15°–25°N latitude show no variations from climatology larger than about 2 K during April, 1982. We therefore concluded that the ash radiative forcing was largely balanced by changes in the stratospheric circulation. We used the TEM model to estimate the amplitude of these circulation changes. Streamfunctions for background and perturbed stratospheres are compared Fig. 7. The TEM circulation shown in Fig 7b assumes that an ash layer with an optical depth 0.6 circled the globe and extended from 15°N to 25°N. It is unlikely that this ash cloud covered

Table I

Stokes Fall Time (in Days) from 26 km

R (um)	0.2	0.6	1.0	3.0	5.0
to 21 km	730	81.	29.	3.2	1.2
to tropopause	1428	159	57.	6.3	2.3

this entire zonal band, since this would require that more than 1% of the erupted solids (cf. Cadle *et al* 1976) reached the middle stratosphere. However, if such a layer existed at some longitudes, the residual vertical velocity inferred from net diabatic heating (of 23 K/day) at the center of the ash layer would have been about 1 cm/s. The ash therefore produces a much greater short-term perturbation in the stratospheric circulation than the H_2SO_4 aerosols or the SO_2 gas. These large ash effects could play an important role in the dispersal of the volcanic plume in the stratosphere. The time-integrated effects of the ash do not exceed those of the aerosols, however, because the stratospheric residence time of the ash is much shorter than that of the aerosols.

Large vertical motions like those described above should also affect the ash particle fallout rates. To estimate these rates, we first computed the Stokes fall speeds using molecular viscosities deduced from the monthly-averaged NMC temperature profiles for May, 1982 at 20°N. Results presented in Table I suggest that 3-μm ash particles should fall from 26 km altitude to the tropopause in a week, but this inference ignores two important facts. First, the Stokes formulation assumes spherical particles, which is probably inaccurate. MacKinnon *et al* (1984) found that a Wilson-Huang formulation of terminal velocity incorporating a shape factor (Wilson and Huang, 1979) gives fall speeds about half as large. Second, the vertical advection associated with the absorption of solar radiation by the silicate ash may actually exceed the Wilson-Huang fall speed for some particle sizes. For example, upward velocities at the center of the ash layer may have been about 1 cm/s. This exceeds the Wilson-Huang fall speed of the 3-μm particles. This upwelling will reduce the ash particle fallout rates, but will not suspend the particles indefinitely for the

following three reasons. First, the amplitude of the heating rates and the associated circulation will decrease as the ash cloud is dispersed horizontally by the perturbed circulation. Second, the ash cloud consists of a distribution of particle sizes, and the heating rates will decrease as particles with radii much greater than 3 μm fall out, since the ash heating rate is a strong function of particle size (Fig. 6). Third, the background temperature profiles suggest increasing viscosity against particle fall as the air parcels rise, so that a stable equilibrium position for the particles should not exist. Thus these experiments cannot fully replace other explanations for the unexpected persistence of large particles (Gooding *et al*, 1983; Knollenberg and Huffman, 1983).

6. Summary

Numerical experiments involving the best accessible data on sulfur dioxide, ash, and sulfate aerosols from the period immediately following the 1982 eruptions of El Chichon have shown that the instantaneous, local radiative forcing by sulfur dioxide gas is comparable to that of the successor sulfuric acid aerosols. The time-averaged, globally integrated effects of the sulfur dioxide are much smaller than those of the aerosols, however, since the SO_2 has a much shorter stratospheric residence time. In spite of this, the radiative heating by the SO_2 can contribute to the height of the plume. Furthermore, the solar energy absorbed in the stratosphere by SO_2 may exceed the energy delivered to the atmosphere by erupted solids.

Silicate ash deposited in the middle stratosphere has a much greater potential than sulfur dioxide to heat or elevate the layer in which it occurs. The amplitude of the ash

heating depends strongly on the ash size distribution, which is not well known for El Chichon. To balance the net radiative heating by ash particles, we infer a vertical advection of about 1 cm/s, which is unusual in the stratosphere. No formulation of fall velocities is likely to be valid if the vertical advection associated with the particles' absorption of solar radiation is ignored.

We reiterate the recommendation, published in an earlier abstract (Gerstell *et al*, 1993), that general circulation models used to study the effects of volcanism on climate should incorporate the radiative forcing of both the SO_2 and the silicate ash, in addition to the sulfuric acid aerosols. Our study differs from that of Young *et al* (1994), who performed their calculations for H_2SO_4 aerosol even though they used the probable presence of uncoated ash to justify their choice of optical thickness. We find that the possibly large perturbation due to silicate ash is dominated by short-wave heating. While the potential effect of silicate ash on global circulation is more obvious than that of SO_2 gas, a model that can produce a full three-dimensional prognosis of the plume's evolution will certainly be affected by inclusion of the sulfur dioxide.

For a more accurate assessment of the impact of volcanic ash on the stratospheric thermal structure and dynamics, we need a much better description of the ash distribution and optical properties. These parameters must be determined in a timely manner since the ash has a limited stratospheric lifetime. The measurements collected just after the April 1982 eruptions of El Chichon still provide one of the best data sets for this purpose. Extensive measurements of the Mt. Pinatubo eruption plume were also made, but these measurements were less appropriate for studying the ash properties because very early

lidar observations of its plume are not available. The sensitivity experiments described here would therefore have been even more speculative for the Mt. Pinatubo eruption.

Acknowledgements

We thank Ian Sprod and Arlin Krueger for providing TOMS sulfur dioxide data. We thank Frank Eparvier for providing a preprint of his SME aerosol columns. We acknowledge use of the ISCCP-C2 database for 1984-86. We are grateful for the detailed comments of two anonymous referees.

Support for this study was provided by the NASA Global Change Research Program, the NASA Volcano-Climate Interactions Program, and the NASA Upper Atmosphere Research Program. The work by J. Crisp and D. Crisp was carried out at the Jet Propulsion Laboratory, California Institute of Technology, under contracts with the National Aeronautics and Space Administration. The work by M. Gerstell was carried out at the California Institute of Technology in partial fulfillment of the requirements for a Ph.D. degree in the Division of Geological and Planetary Sciences, under contract NAGW-413 with the National Aeronautics and Space Administration.

References

Andrews, Holton and Leovy, 1987: *Middle Atmosphere Dynamics.* Orlando, FL, Academic Press, 489 pp.

Andrews, D.G. and M.E. McIntyre, 1976: Planetary waves in horizontal and vertical shear: the generalized Eliassen-Palm relation and the mean zonal acceleration. *J. Atmos. Sci.* **33**, 2031–2048.

Angell, J.K. and J. Korshover, 1983: Comparison of stratospheric warmings following Agung and Chichon. *Mon. Weather Rev.* **111**, 2129–2135.

Bandeen, W.R. and R.S. Fraser (eds.), 1982: Radiative effects of the El Chichon volcanic eruption: preliminary results concerning remote sensing. *NASA Technical Memo 84959*, 102 pp.

Bell, J.F. and D. Crisp, 1993: Ground-based imaging spectroscopy of Mars in the near-IR: preliminary results. *Icarus* **104**, 2–19.

Briegleb, B.P., 1992: Delta-Eddington approximation for solar radiation in the NCAR community climate model. *J. Geophys. Res.* **97**, 7603–7612.

Cadle, R. D., C.S. Kiang, and J.-F. Louis, 1976: The global scale dispersion of the eruption clouds from major volcanic eruptions. *J. Geophys. Res.* **81**, 3125–3132.

Coulson, K.L., T.J. DeFoor, and J. DeLuisi, 1982: Lidar and optical polarization measurements of stratospheric cloud in Hawaii. *EOS Trans. AGU* **63**, 897.

Crisp, D., 1986: Radiative forcing of the Venus mesosphere, I. Solar fluxes and heating rates. *Icarus* **67**, 484–514.

Crisp, D., 1989: Radiative forcing of the Venus mesosphere, II. Thermal fluxes, cooling

rates, and radiative equilibrium temperatures. *Icarus* **77**, 391–413.

Crisp, D., 1990: Infrared radiative transfer in the dust-free Martian atmosphere. *J. Geophys. Res.* **95**, 14577–14588.

DeLuisi, J.J., E.G. Dutton, K.L. Coulson, T.E. DeFoor, and B.G. Mendonca, 1983: On some radiative features of the El Chichon volcanic stratospheric dust cloud and a cloud of unknown origin observed at Mauna Loa. *J. Geophys. Res.* **88**, 6769–6772.

DeMore, W.B., D.M. Golden, R.F. Hammpson, M.J. Kurylo, C.J. Howard, A.R. Ravishankara, C.E. Kolb, and M.J. Molina, 1992: Chemical kinetics and photochemical data for use in stratospheric modeling. *JPL Publication 92-20*, Jet Propulsion Laboratory, Pasadena, CA, 185 pp.

Dunkerton, T., 1978: On the mean meridional mass motions of the stratosphere and mesosphere. *J. Atmos. Sci.* **35**, 2325–2333.

Dutton, E.G. and J.R. Christy, 1992: Solar radiative forcing at selected locations and evidence for global lower tropospheric cooling following the eruptions of El Chichon and Pinatubo. *Geophys. Res. Lett.* **19**, 2313–2316.

Elsasser, W.M., 1943: Heat transfer by infrared radiation in the atmosphere. *Harvard Meteorological Studies, No. 6.* Harvard University Press.

Eparvier, F., D.W. Rusch, R.T. Clancy, and G.E. Thomas, 1994: Solar Mesosphere Explorer satellite measurements of El Chichon stratospheric aerosols 2: aerosol mass and size parameters. Submitted to *J. Geophys. Res.*

Freeman, K.P. and K.N. Liou, 1979: Climate effects of cirrus clouds. *Adv. Geophys.* **21**, 231–287.

Fujita, T., 1985: The abnormal temperature rises in the lower stratosphere after the 1982 eruptions of the volcano El Chichon, Mexico. *Papers in Meteor. and Geophys.* **36**, 47–60.

Gelman, M. E., A. J. Miller, K. W. Johnson and R. M. Nagatani, 1986: Detection of long term trends in global stratospheric temperature from NMC analyses derived from NOAA satellite data. *Adv. Space Res.* **6**, 17–26.

Gerstell, M.F., J. Crisp and D. Crisp, 1993: Radiative forcing of the stratosphere by SO_2, ash, and H_2SO_4 aerosols, during the first 3 months after the El Chichon eruptions. *EOS Trans. AGU* **74:43**, 105.

Gille, J.C., L.V. Lyjak, and A.K. Smith, 1987: The global residual mean circulation in the middle atmosphere for the northern winter period. *J. Atmos. Sci.* **44**, 1437–1452.

Gooding, J.L. and U.S. Clanton, 1983: El Chichon volcanic ash in the stratosphere: Particle abundances and size distributions after the 1982 eruption. *Geophys. Res. Lett.* **10**, 1033–1036.

Goody, R.M. and Y.L. Yung, 1989: *Atmospheric Radiation: Theoretical Basis*, Chap. 4. New York, Oxford University Press, 519 pp.

Hale, G.M. and M.R. Querry, 1973: Optical constants of water in the 200-nm to 200-μm wavelength region. *Appl. Optics* **12**, 555–563.

Hansen, J.E., 1971: Multiple scattering of polarized light in planetary atmospheres. Part II: Sunlight reflected by terrestrial water clouds. *J. Atmos. Sci.* **28**, 1400–1426.

Hansen, J.E. and L.D. Travis, 1974: Light scattering in planetary atmospheres. *Space Sci. Rev.* **16**, 527–610.

Hansen, J.E., W.-C. Wang, and A.A. Lacis, 1978: Mount Agung eruption provides test of a global climatic perturbation. *Science* **199**, 1065–1068.

Kiehl, J.T. and B.P. Briegleb, 1993: The relative roles of sulfate aerosols and greenhouse gases in climate forcing. *Science* **260**, 311–314.

Knollenberg, R.G. and D. Huffman, 1983: Aerosol measurements in El Chichon. *Geophys. Res. Lett.* **10**, 1025–1028.

Komhyr, W.D., R.D. Grass and P.J. Reitelbach, 1989: Total ozone, ozone vertical distributions, and stratospheric temperatures at South Pole, Antarctica in 1986 and 1987. *J. Geophys. Res.* **94**, 11429–11436.

Krueger, A.J., 1983: Sighting of El Chichon sulfur dioxide clouds with the Nimbus 7 total ozone mapping spectrometer. *Science* **220**, 1377–1379.

Labitzke, K., B. Naujokat, and M. P. McCormick, 1983: Temperature effects on the stratosphere of the April 4, 1982 eruption of El Chichon, Mexico. *Geophys. Res. Lett.* **10**, 24–26.

Luhr, J.F., 1990: Experimental phase relations of water and sulfur-saturated arc magmas and the 1982 eruption of El Chichon volcano. *J. Petrology* **31**, 1071.

Mackinnon, I.D.R., J.L. Gooding, D.S. McKay, and U.S. Clanton, 1984: The El Chichon stratospheric cloud: Solid particulates and settling rates. *J. Volcanol. Geotherm. Res.* **23**, 125–146.

Matthews, E., 1983: Global vegetation and land-use: new high resolution data-bases for climate studies. *J. Climate Appl. Meteor.* **22**, 474–487.

Newell, R. E., 1970: Stratospheric temperature change from the Mount Agung vol-

canic eruption. *J. Atmos. Sci.* **27**, 977–978.

Oberbeck, V.R., E.F. Danielsen, K.B. Snetsinger, and G.V. Ferry, 1983: Effect of the eruption of El Chichon on stratospheric aerosol size and composition. *Geophys. Res. Lett.* **11**, 1021–1024.

Oort, A.H., Global atmospheric circulation statistics, 1958-1973, *NOAA Professional Paper 14*, U.S. Department of Commerce, National Oceanic and Atmospheric Administration, Washington, D.C., April, 1983.

Palmer, K.F. and D. Williams, 1975: Optical constants of sulfuric acid; application to the clouds of Venus? *Appl. Optics* **14**, 208–219.

Parker, D.E. and J.K.L. Brownscombe, 1983: Stratospheric warming following the El Chichon volcanic eruption. *Nature* **301**, 406–408.

Peck, D.L., 1978: Cooling and vesiculation of Alae lava lake. *USGS Professional Paper 935B*, 59 pp.

Pollack, J.B., O.B. Toon, and B.N. Khare, 1973: Optical properties of some terrestrial rocks and glasses. *Icarus* **19**, 372–389.

Pollack, J.B., F.C. Witteborn, K. O'Brien, and B. Flynn, 1991: A determination of the infrared optical depth of the El Chichon volcanic cloud. *J. Geophys. Res.* **96**, 3115–3122.

Quiroz, R.S., 1983: The isolation of stratospheric temperature change due to the El Chichon volcanic eruption from nonvolcanic signals. *J. Geophys. Res.* **88**, 6773–6780.

Rampino, M.R., S. Self, and R.B. Stothers, 1988: Volcanic winters. *Ann. Rev. Earth Planet. Sci.* **16**, 73–99.

Rind, D., N. K. Balachandran, and R. Suozzo, 1992: Climate change and the middle

atmosphere, Part II: The impact of volcanic aerosols. *J. Climate* **5**, 189–208.

Rosenfield, J.E., M.R. Schoeberl, and M.A. Geller, 1987: A computation of the stratospheric diabatic circulation using an accurate radiative transfer model. *J. Atmos. Sci.* **44**, 859–876.

Rossow, W.B. and R.A. Schiffer, 1991: ISCCP cloud data products. *Bull. Amer. Meteor. Soc.* **72**, 2–20.

Rothman, L.S., R.R. Gamache, R.H. Tipping, C.P. Rinsland, M.A.H. Smith, D.C. Benner, V.M. Devi, J.-M. Flaud, C. Camy-Peyret, A. Perrin, A. Goldman, S.T. Massie, C.R. Brown, and R.A. Toth, 1992: The HITRAN molecular database editions of 1991 and 1992. *J. Quant. Spectrosc. & Radiat. Transfer* **48**, 469–507.

Rye, R.O, J.F. Luhr, and M.D. Wasserman, 1984: Sulfur and oxygen isotope systematics of the 1982 eruptions of El Chichon volcano, Chiapas, Mexico. *J. Volcan.* **23**, 109–123.

Santee, M., 1992: The thermal structure, dust loading, and meridional transport in the Martian atmosphere during late southern summer. Ph.D. thesis, Calif. Inst. of Tech., 1992.

Santee, M. and D. Crisp, 1993: Thermal structure and dust loading of the Martian atmosphere during late southern summer: Mariner 9 revisited. *J. Geophys. Res.* **98**, 3261–3279.

Santee, M. and D. Crisp, 1994: Diagnostic calculations of the circulation in the Martian atmosphere. Submitted to *J. Geophys. Res. - Planets.*

Shia, R.L., Y.L. Yung, M. Allen, R.W. Zurek, and D. Crisp, 1989: Sensitivity study

of advection and diffusion coefficients in a 2-dimensional stratospheric model using C-14 data. *J. Geophys. Res.* **94**,18467–18484.

Shibata, T., M. Fujiwara and M. Hirono, 1984: The El Chichon volcanic cloud in the stratosphere: lidar observations at Fukuoka and numerical simulation. *J. Atmos. Terrestr. Phys.* **12**, 1121–1146.

Stamnes, K., S.-C. Tsay, W. Wiscombe, and K. Jayaweera, 1988: Numerically stable algorithm for discrete-ordinate method radiative transfer in multiple-scattering and emitting layered media. *Appl. Optics* **27**, 2502–2509.

Thekaekara, M.P., 1969: Solar fluxes at the top of earth's atmosphere. *Appl. Opt.* **8**, 1713–1732.

Thomas, G.E., B.M. Jakosky, R.A West, and R.W. Sanders, 1983: Satellite limb-scanning thermal infrared observations of the El Chichon stratospheric aerosol: First results. *Geophys. Res. Lett.* **10**, 997–1000.

Turco, R.P., O.B. Toon, R.C. Whitten, P. Hamill, and R.G. Keesee, 1983: The 1980 eruptions of Mt. St. Helens: physical and chemical processes in the stratospheric cloud. *J. Geophys. Res.* **88**, 5299–5319.

Vupputuri, R.K.R. and J.P. Blanchet, 1984: The possible effects of El Chichon eruption on atmospheric thermal and chemical structure and surface climate. *Geof. Int.* **23**, 433–447.

Warneck, P., 1988: *Chemistry of the Natural Atmosphere.* San Diego, Academic Press, 757 pp.

Warren, S.G., 1982: Optical properties of snow. *Rev. Geophys.* **20**, 67–89.

Wilson, L. and T.C. Huang, 1979: The influence of shape on the atmospheric settling velocity of volcanic ash particles. *Earth Planet. Sci. Lett.* **44**, 311–324.

Wiscombe, W.J., 1980: Improved Mie-scattering algorithms. *Appl. Optics* **19**, 1505–1509.

World Meteorological Organization, 1986: *Atmospheric Ozone 1985.* WMO Global Ozone Research and Monitoring Project Report No. 16, Vol. I.

Young, R.E., H. Houben, and O.B. Toon, 1994: Radiatively forced dispersion and induced temperature perturbations in the stratosphere during the first few months following the eruption. *Geophys. Res. Lett.* **21**, 369–372.

Paper III: Sensitivity of polar stratospheric radiative heating to upper and lower boundary conditions

ABSTRACT

Uncertainties in the solar spectrum can affect modeled net heating rates in the upper stratosphere by a factor of several. Variation among Antarctic surface albedo values in common use can affect modeled net heating rates in the lower stratosphere by tens of percent. Large uncertainties in polar cloud cover are less important to stratospheric heating models. I join Marcel Nicolet in urging support for a continuous solar observation program, and recommend that future intercomparisons of stratospheric radiation models prescribe a solar spectrum, to reveal other differences.

This note comments on the large sensitivity of stratospheric radiative heating to uncertain details of the solar spectrum, on the smaller but appreciable effect of using different surface albedos that appear in the literature, and on the negligible role of large uncertainties in polar cloud cover. Caltech-JPL's radiative transfer model is described by Crisp (1986, 1989,1990) and by Gerstell, Crisp and Crisp (1994; hereafter, GCC). The seven-gas climatology (H_2O, CO_2, O_3, N_2O, CH_4, O_2, NO_2) used here is for January, 85°S, and its derivation is also described in GCC. The latitude and season were chosen for large sensitivities of stratospheric heating to upper and lower boundary conditions. The sensitivities are not necessarily representative, or maximal. A more extensive future paper may incorporate a global map.

Marcel Nicolet (1990) argued that continuing support for measurement of solar spectral irradiances had not reached the minimum level necessary for the needs of aeronomers and climate scientists. A cogent illustration of dynamical sensitivity to the solar spectrum lies hidden in the differences between Caltech-JPL vertical velocity field calculations, and those of other groups, as shown in the published intercomparison of Nagatani and Rosenfield (1993). Although the total solar flux at the top of the atmosphere, and its temporal fluctuations, are subjects of reasonable agreement, differences of 10% to 20% in spectral solar fluxes are found in the ultraviolet, where most ozone heating occurs. This is an improvement from the 50% differences cited in the critical review of Brasseur and Simon (1981). Given the close balance of thermal cooling and solar heating in the stratosphere, an error of 10% in solar heating always produces larger errors in net heating, occasionally even a change of sign in the vertical velocity.

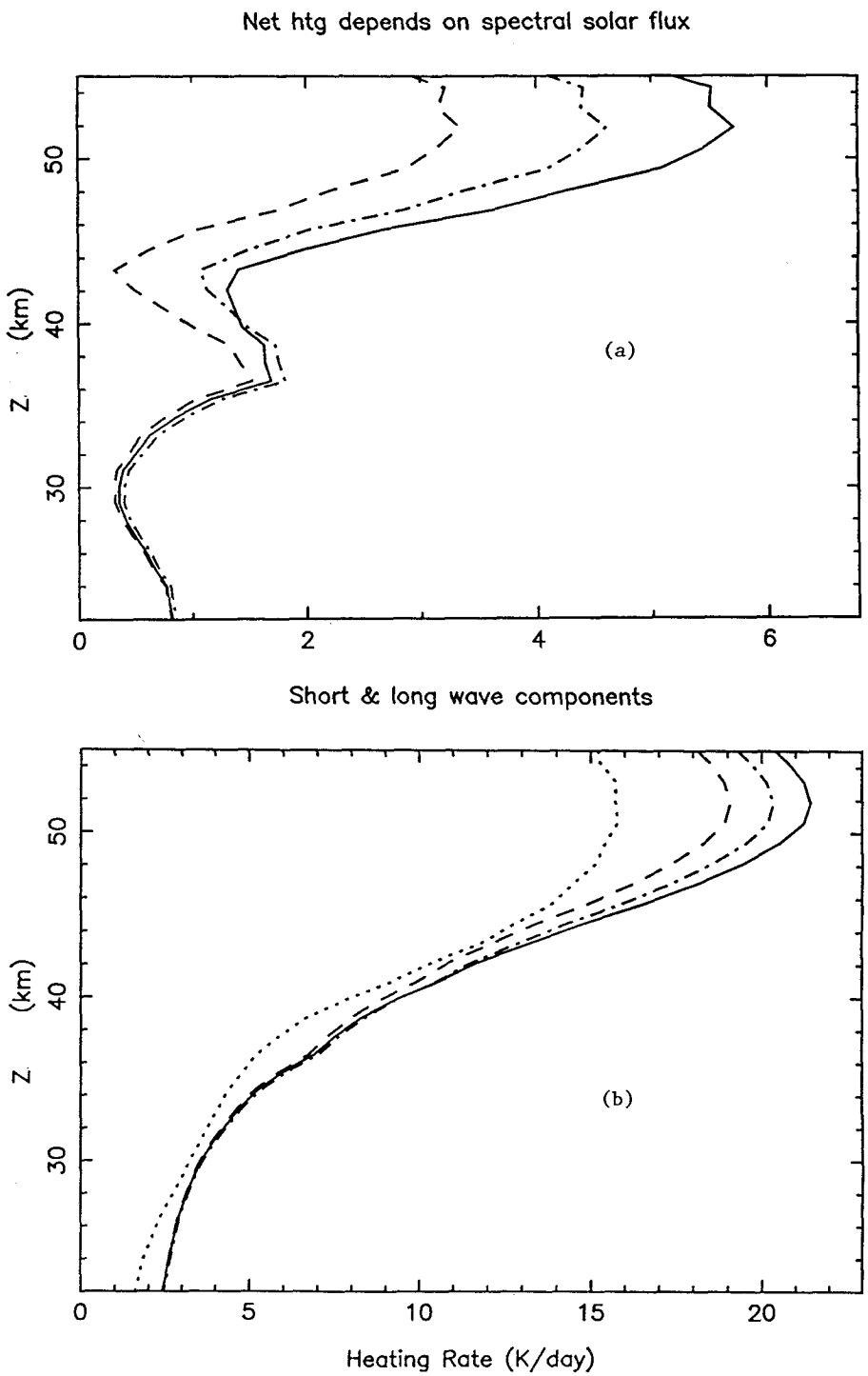

Fig. 1 Above: net radiative heating of the stratosphere at 85°S in January, diurnally averaged; calculated with three different solar spectra. (WMO=dashes, Nicolet=dot-dash, Thekaekara=solid.) Below: solar heating and thermal cooling (dots), as above.

To illustrate the sensitivity to top-of-atmosphere solar spectral fluxes, Fig. 1a shows our net radiative heating for a cloudless sky, calculated with three different sets of solar spectral fluxes: those of Thekaekara (1969), the World Meteorological Organization (1986; WMO), and Nicolet (1989). Nicolet's recommended reference spectrum is derived from SUSIM measurements (Van Hoosier *et al*, 1987) for wavelengths shorter than 0.4 μm, and from Arvesen *et al* (1969) for longer wavelengths. Outside the WMO range, we supplement the WMO set with Thekaekara's values. The WMO and Thekaekara datasets then integrate to the same solar constant, within 0.1%, but large differences at wavelengths less than 300 nm cause calculated solar heating rates to vary by at least 10% at altitudes greater than 45 km. In the case at hand, this translates into variation of net radiative heating rates by a factor of 1.7–4.4 in the 40–50 km range, and a factor of 1.5–1.8 at higher altitudes. The solar and thermal components of the net heating from Fig. 1a are shown in Fig. 1b.

In the comparisons of Nagatani and Rosenfield, the Caltech group used Thekaekara (1969); more recently we have used WMO (1986), as in GCC. Rosenfield *et al* (1987) cite WMO, as do Yang *et al*, 1991. Brasseur *et al* (1993) cite Brasseur and Simon (1981), whose data were the result of a critical review of 14 solar spectral observations of the 1970's. Briegleb (1992) mainly uses Labs and Neckel (1968), and finds heating rate discrepancies arising from the difference between this solar spectrum and that of Thekaekara and Drummond (1971) are limited to about 0.05 K/day; but Briegleb's comparisons are tropospheric. Our experience supports his view that the uncertainty of the solar spectrum has little direct impact on tropospheric studies.

Various modeling groups use different schemes for visible surface albedo. A difference of 15% in visible albedo in the Antarctic produces a change of 4% in solar heating, or 10%-40% in net stratospheric radiative heating, as illustrated by Fig. 2a. The effect is due mainly to the visible bands of ozone and is confined to the lower stratosphere. Our model assumes a Lambert surface, so that many reflected photons travel shorter optical paths than the direct beam. The net heating rates in Fig. 2 were calculated with three different values of visible surface albedo: 0.795, which is Yang, Olaguer, and Tung's (1991) visible albedo for 85°S; 0.84, the short-wave albedo for 80°S to 90°S in Sellers (1965) Table I; and Caltech's 0.94, based on 1984-86 January observations near 85°S by the International Satellite Cloud Climatology Project (ISCCP; see Rossow and Schiffer, 1991). The WMO solar spectrum is used in all cases of Fig. 2, and a near-infrared albedo of 0.67. Following Briegleb (1992), GCC assumed the ground albedo reported by ISCCP at 0.6 μm could be used from 0.7 μm to 0.2 μm, but for the present comparison our albedo drops to zero at wavelengths shorter than 0.28 μm, following Yang, Olaguer and Tung (1991). Ongoing global measurements of surface albedo at more than the two standard ISCCP wavelengths would be desirable. The solar and thermal components of the net heating from Fig. 2a are shown in Fig. 2b.

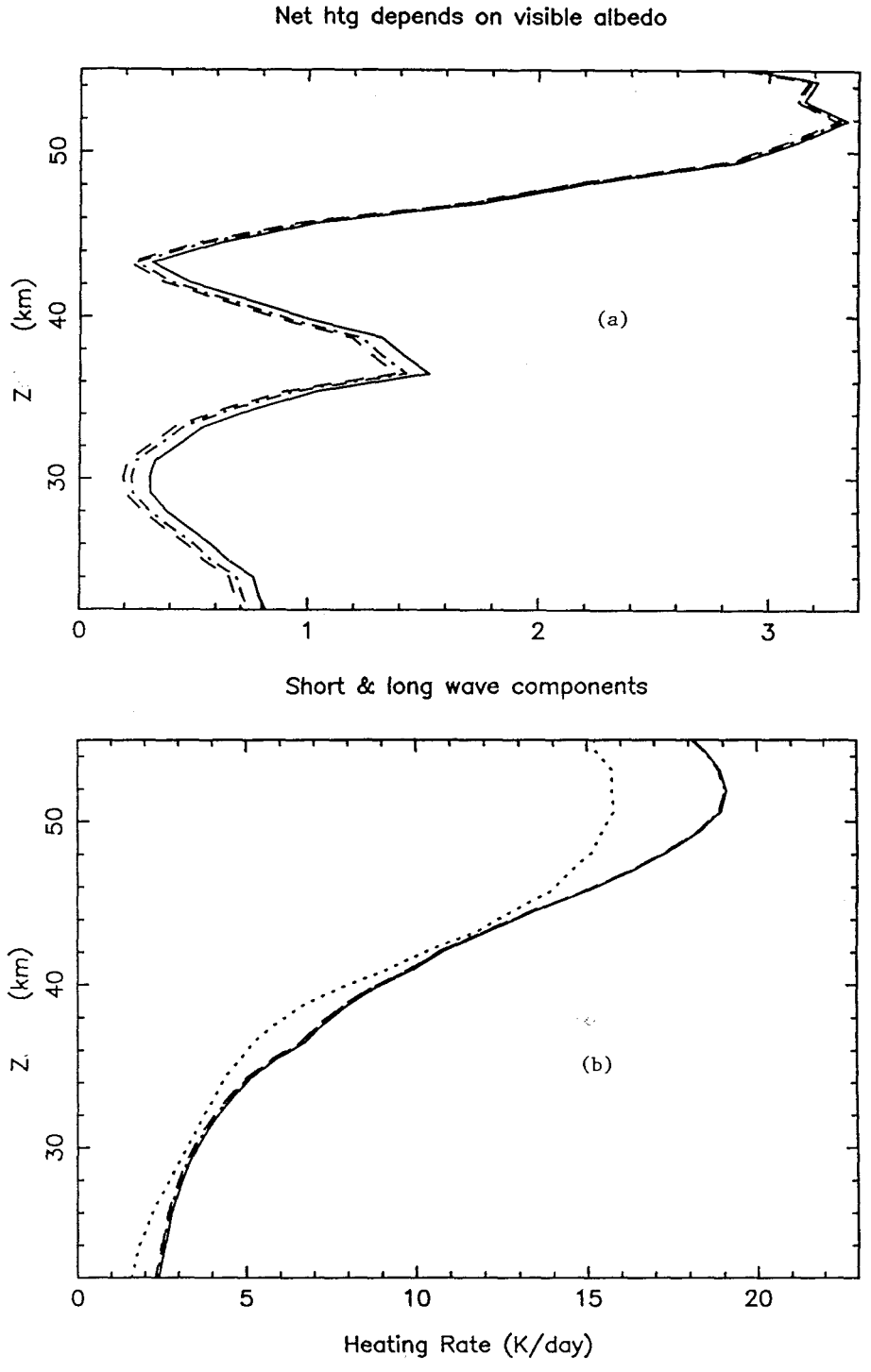

Fig. 2 Above: net radiative heating of the stratosphere at 85°S in January, diurnally averaged; calculated with three different values of surface albedo. (Dashes=0.795, dot-dash=0.84, solid=0.94.) Below: solar heating and thermal cooling (dots), as above.

One might next ask whether the sensitivity to surface albedo would change if the specular component of snow and ice reflectance were considered. The heating rate in the plane-parallel atmosphere model would depend on the azimuthally-integrated value of the bidirectional reflectance distribution. Perovich (1994) presents bidirectional reflectance values for various snow and ice types, with a solar zenith angle near 60°. Although his reported reflectance is a strong function of azimuth at his largest zenith viewing angle (60°), the azimuthally-integrated reflectance is not appreciably enhanced at the 60° zenith viewing angle for snow. The enhancement for bare ice and blue ice seems to be on the order of 5% or less. There could be a slight increase in the clear-sky sensitivity to surface albedo that is reported above, if the bidirectional reflectance were treated accurately in the heating-rate calculation.

One might next inquire about cloudiness, since all of the above calculations were for cloudless skies. At high summer latitudes, cloud cover reported by satellites differs markedly from that reported by ground-based observers. For example, at 85°S, the January fractional cloudiness suggested by ISCCP data is less than 5%, while Peixoto and Oort (1992) rely on Berliand and Strokina's (1980) data, which report something near 55%. But the difficulty of remotely sensing clouds over an area with a large surface albedo immediately suggests that their radiative effects on the stratosphere will be virtually nil under such conditions, and our radiative calculations support this idea, showing less than 1% change in stratospheric radiative heating when cloud cover is 55% as opposed to 0%, over the summer Antarctic.

I join Nicolet in urging support for a continuous solar observation program. Climate

modeling is not the only application directly affected by uncertainty about solar spectral fluxes; see, for example, Cagaeo *et al* (1994). I further recommend that any new intercomparisons of middle-atmosphere radiative transfer models should prescribe a particular solar spectrum, in order that other differences can be seen and diagnosed.

Acknowledgements

I am indebted to D. Crisp and E. Olaguer for the use of their radiative transfer models. The use of ISCCP-C2 data and the support of NASA contract NAGW-413 are acknowledged. Y. Yung and J. Eluszkiewicz provided useful advice.

References

Arvesen, J.C., R.N. Griffin, Jr., and B.D. Pearson, 1969: Determination of extraterrestrial spectral irradiance from a research aircraft. *Appl. Optics* **8**, 2215.

Berliand, T.G. and L.A. Strokina, 1980: *Global distribution of total cloudiness.* Gidrometeoizdat, Leningrad, 71 pp.

Brasseur, G., C. Granier, I. Folkins, S. Walters, M. Hitchman and A. Smith, 1993: NCAR model specifications, limitations, goals. In *The Atmospheric Effects of Stratospheric Aircraft: Report of the 1992 Models and Measurements Workshop*, Prather, M. J. and E. E. Remsberg, eds. NASA Reference Publication 1292, Vol. I, pp. 106–109.

Brasseur, G. and P.C. Simon, 1981: *J. Geophys. Res.* **86**, 7343-7362.

Briegleb, B.P., 1992: Delta-Eddington approximation for solar radiation in the NCAR community climate model. *J. Geophys. Res.* **97**, 7603–7612.

Cagaeo, R.P., Y.L. Ha, M.F. Morgan and Y.L. Yung, 1994: Calculated hydroxyl $A^2\Sigma - X^2\Pi$ (0,0) band emission rate factors and absorption cross sections applicable to atmospheric spectroscopy. Submitted to *J. Quant. Spectrosc. & Rad. Transfer.*

Crisp, D., 1986: Radiative forcing of the Venus mesosphere, I. Solar fluxes and heating rates. *Icarus* **67**, 484–514.

Crisp, D., 1989: Radiative forcing of the Venus mesosphere, II. Thermal fluxes, cooling rates, and radiative equilibrium temperatures. *Icarus* **77**, 391–413.

Crisp, D., 1990: Infrared radiative transfer in the dust-free Martian atmosphere. *J. Geophys. Res.* **95**, 14577–14588.

Gerstell, M. F., J. Crisp and D. Crisp (1995), Radiative forcing of the stratosphere by SO_2 gas, silicate ash, and H_2SO_4 aerosols, shortly after the 1982 eruptions of El Chichon. Submitted to *J. Climate.*

Labs, D. and H. Neckel, 1968: The radiation of the solar photosphere from 200A to 100 μ. *Z. Astrophys.* **69**, 1–73.

Nagatani, R. M. and J. E. Rosenfield (1993), Temperature, net heating and circulation. In *The Atmospheric Effects of Stratospheric Aircraft: Report of the 1992 Models and Measurements Workshop*, Prather, M. J. and E. E. Remsberg, eds. NASA Reference Publication 1292, Vol. II, pp. A1–A47.

Nicolet, Marcel 1989: Solar spectral irradiances with their diversity bewteen 120 and 900 nm. *Planet. Space Sci.* **37**, 1249–1289.

Peixoto, J.P. and A.H. Oort, 1992: *The Physics of Climate.* New York, American Inst. of Physics, 520 pp.

Perovich, D.K, 1994: Light reflection from sea ice during the onset of melt. *J. Geophys. Res.* **99**, 3351–3359.

Rosenfield, J.E., M.R. Schoeberl, and M.A. Geller, 1987: A computation of the stratospheric diabatic circulation using an accurate radiative transfer model. *J. Atmos. Sci.* **44**, 859–876.

Rossow, W.B. and R.A. Schiffer, 1991: ISCCP cloud data products. *Bull. Amer. Meteor. Soc.* **72**, 2–20.

Sellers, W.D., 1965: *Physical Climatology.* Univ. of Chicago Press, 272 pp.

Thekaekara, M.P., 1969: Solar fluxes at the top of earth's atmosphere. *Appl. Opt.* **8**, 1718–1732.

Thekaekara, M.P. and A.J. Drummond, 1971: Standard values for the solar constant and its spectral components. *Nature (London) Phys. Sci.* **229**, 6–9.

Van Hoosier, M.E., J.-D.F. Bartoe, G.E. Brueckner, and D.K. Prinz, 1987: Solar irradiance measurements 120-400 nm from *Spacelab*-2 (results from the SUSIM experiment). IUGG Assembly, Vancouver.

World Meteorological Organization, 1986: *Atmospheric Ozone 1985.* WMO Global Ozone Research and Monitoring Project Report No. 16, Vol. I.

Yang, H., E. Olaguer, and K.K. Tung (1991): Simulation of the present-day ozone, odd nitrogen, chlorine, and other species using a coupled 2-D model in isentropic coordinates. *J. Atmos. Sci.* **48**, 442–471.

Appendix 2

Further validations and sensitivities of Caltech-JPL's radiative transfer model, RTMOD

The following experiments were documented as a result of the external review of Eluszkiewicz *et al*'s (1994) interpretation of Upper Atmosphere Research Satellite data, and in final preparation for the publication of Gerstell, Crisp and Crisp (1994; GCC).

For a comparison of RTMOD thermal cooling against that of GFDL's line-by-line program, see Fig. 0. While RTMOD's cooling rates are a little too large everywhere, the match is adequate. If using a light table, note that the figure we want to match is the dashed line, since we had the GFDL version of the inputs. Though the match in this particular case could be improved by tuning any of a number of parameters, it's not clear that the program's overall accuracy would then be improved for other cases. That's why Dr. Crisp is developing a more accurate model, which of necessity will be much slower. See West, Crisp and Chen (1990). Allusions below to the UW group refer to the radiative transfer model described in Yang, Olaguer and Tung (1991).

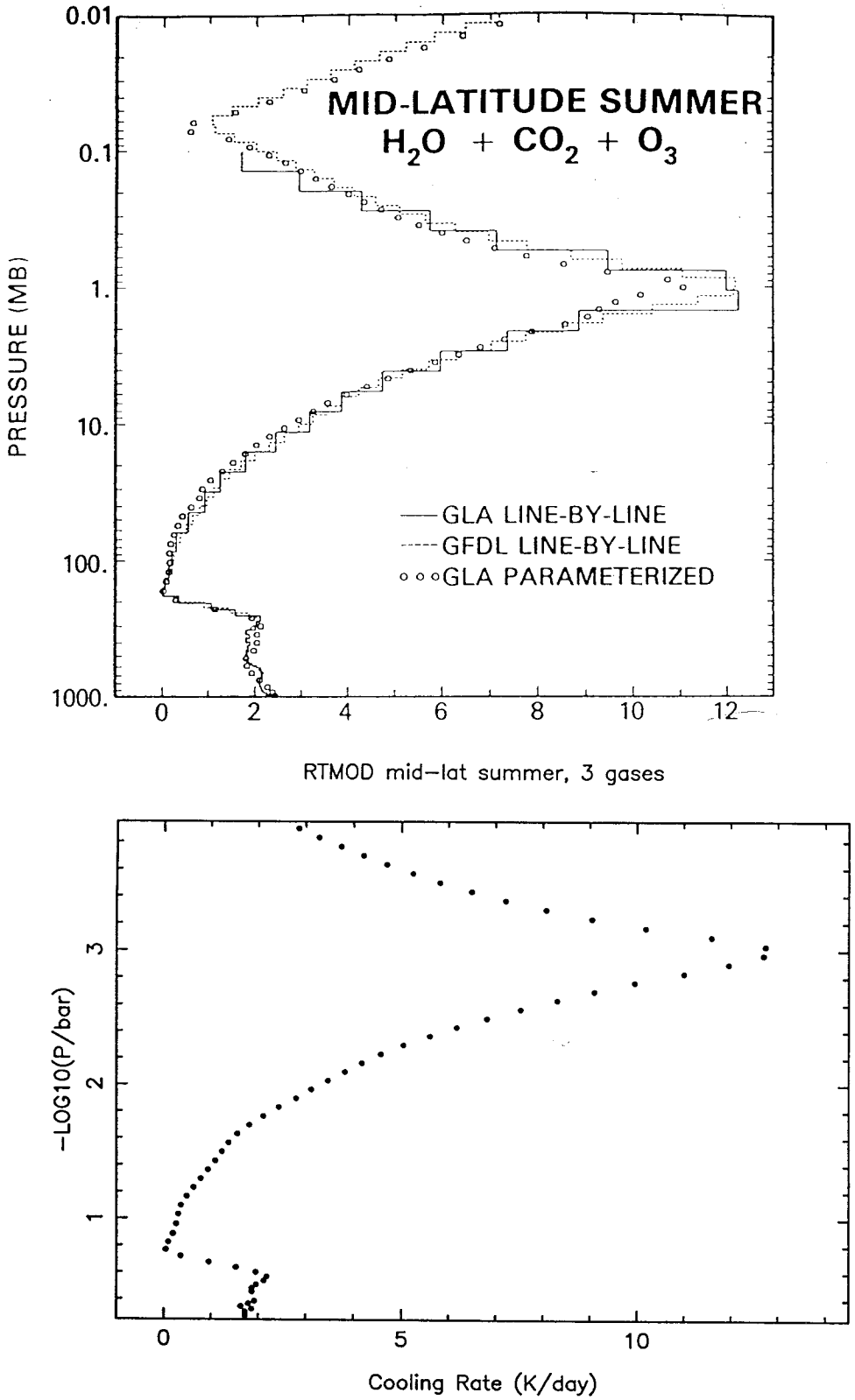

Fig. 0 Comparison of RTMOD mid-latitude summer thermal cooling for a mixture of three gases against standard line-by-line results. Top panel from Ridgway, Harshvardhan, and Arking (1991). Scales are the same in both panels.

It was Dr. Eluszkiewicz who realized the vertical resolution we had habitually been using was inadequate even for solar heating calculations. The pole-to-pole climatology I accumulated for GCC involved a 2-km vertical grid, or more accurately, a grid in which $p_n/p_{n+1} = 10^{1/8}$. We found that doubling the resolution of the p grid for the radiative transfer calculation gave substantial changes in the results, as in Fig. 1 (an example for south polar summer); doubling it *again* gave a further perceptible change, but an order of magnitude smaller.

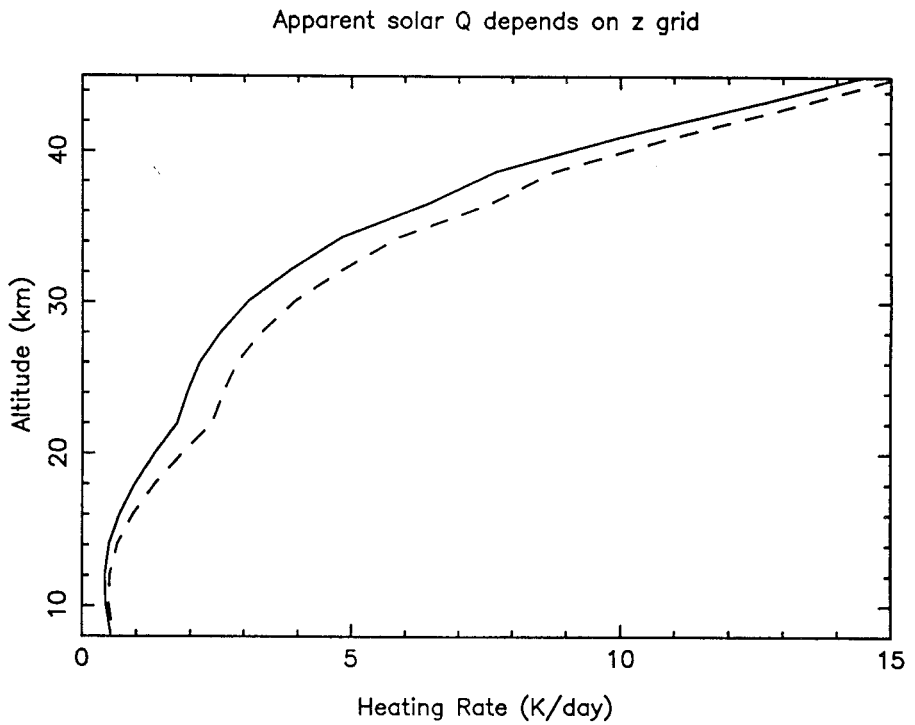

Fig. 1 Diurnal average solar heating at 90°S in summer calculated by RTMOD at z^* resolution of 1 km (solid) and 2 km (dashes).

Boundary conditions were among the major sources of discrepancy between RTMOD's results and UW's results, but not the sole source. Suspecting differences in ozone heating, we tried to validate that part of RTMOD. UW had already conceded that their treatment of line absorption in the near-IR was less detailed, and less likely to be correct, than RTMOD's. See Yang *et al* (1991) for a discussion of their methods. Significant differences in solar heating results of RTMOD and UW near the peak of the ozone layer provoked questions about our treatment of simple photolysis, and/or our diurnal averaging procedures. Both RTMOD and UW use the same set of ozone cross-sections (DeMore *et al*, 1992), which differ from WMO (1986) cross-sections only at wavelengths shorter than 250 nm.

Figs. 2–4 validate RTMOD's treatment of ozone photolysis by comparison against Stamnes and Tsay (1990; St&Ts), for three of their four spectral regions. Fig. 5 shows RTMOD's heating-rate deficit vs. St&Ts in the crucial 175–290 nm band. This is qualitatively what one expects based on the above-mentioned difference in DeMore and WMO cross-sections in this spectral range. For example, at 220 nm, the DeMore cross-section is about 15% smaller than that of WMO. The agreement shown in Fig. 3 (315–400 nm) is less impressive than Figs. 2 and 4, but the total heating contribution from this band is much smaller in any case. Fig. 4 (290–315 nm) appears to support Dr. Crisp's decision not to include the temperature dependence of the cross-sections given in WMO; this is the spectral range where that decision would have been most likely to produce a perceptible error. RTMOD of course accommodates the temperature dependence of line

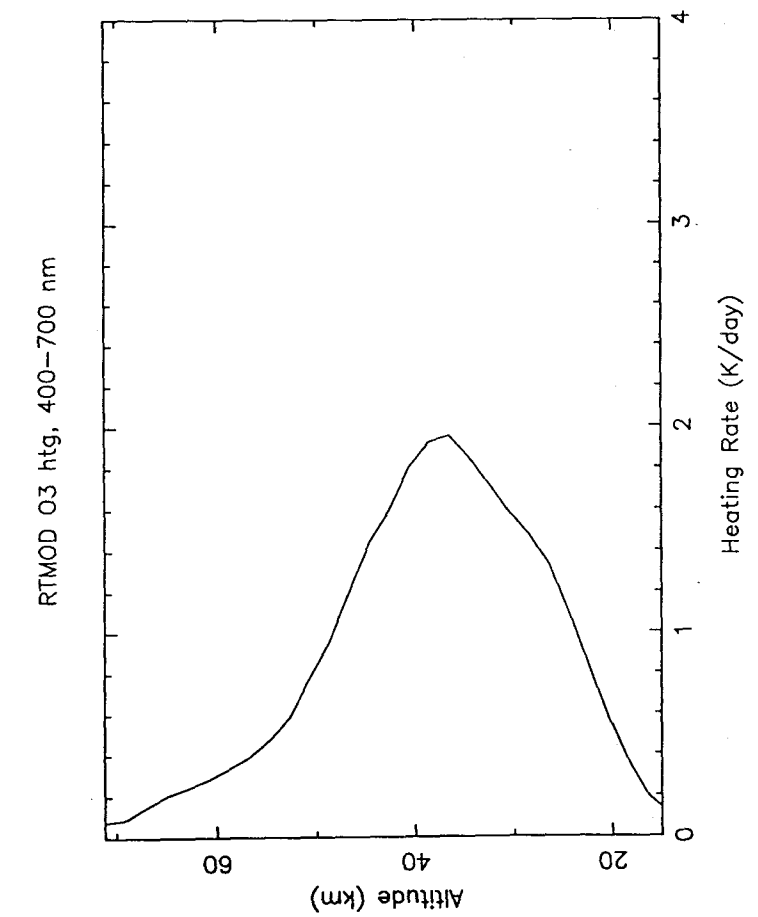

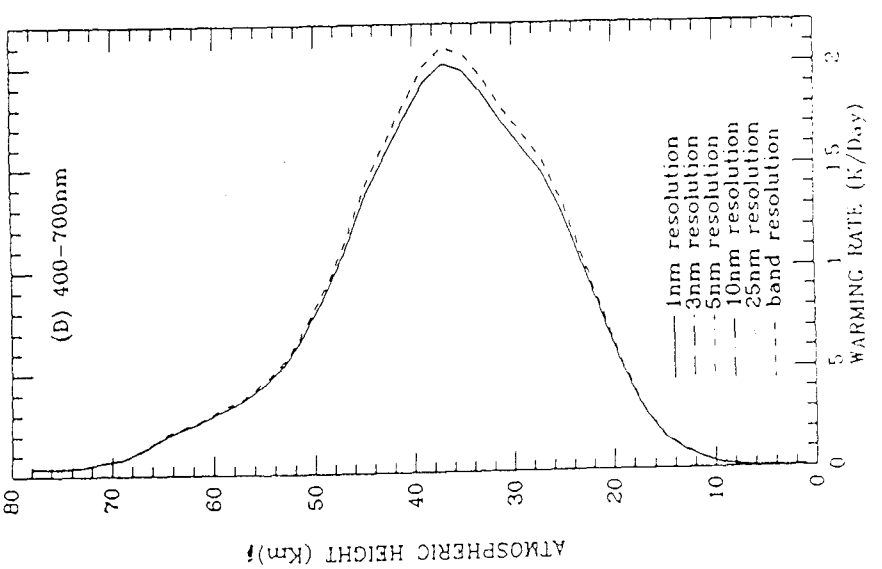

Fig. 2 Comparison of ozone heating in the 400-700 nm band for a U.S. standard atmosphere, 55° solar zenith angle, 0.2 surface albedo, with Rayleigh scattering, as calculated by RTMOD and Stamnes & Tsay (1990). Scales are the same in both panels; vertical offset should be ignored.

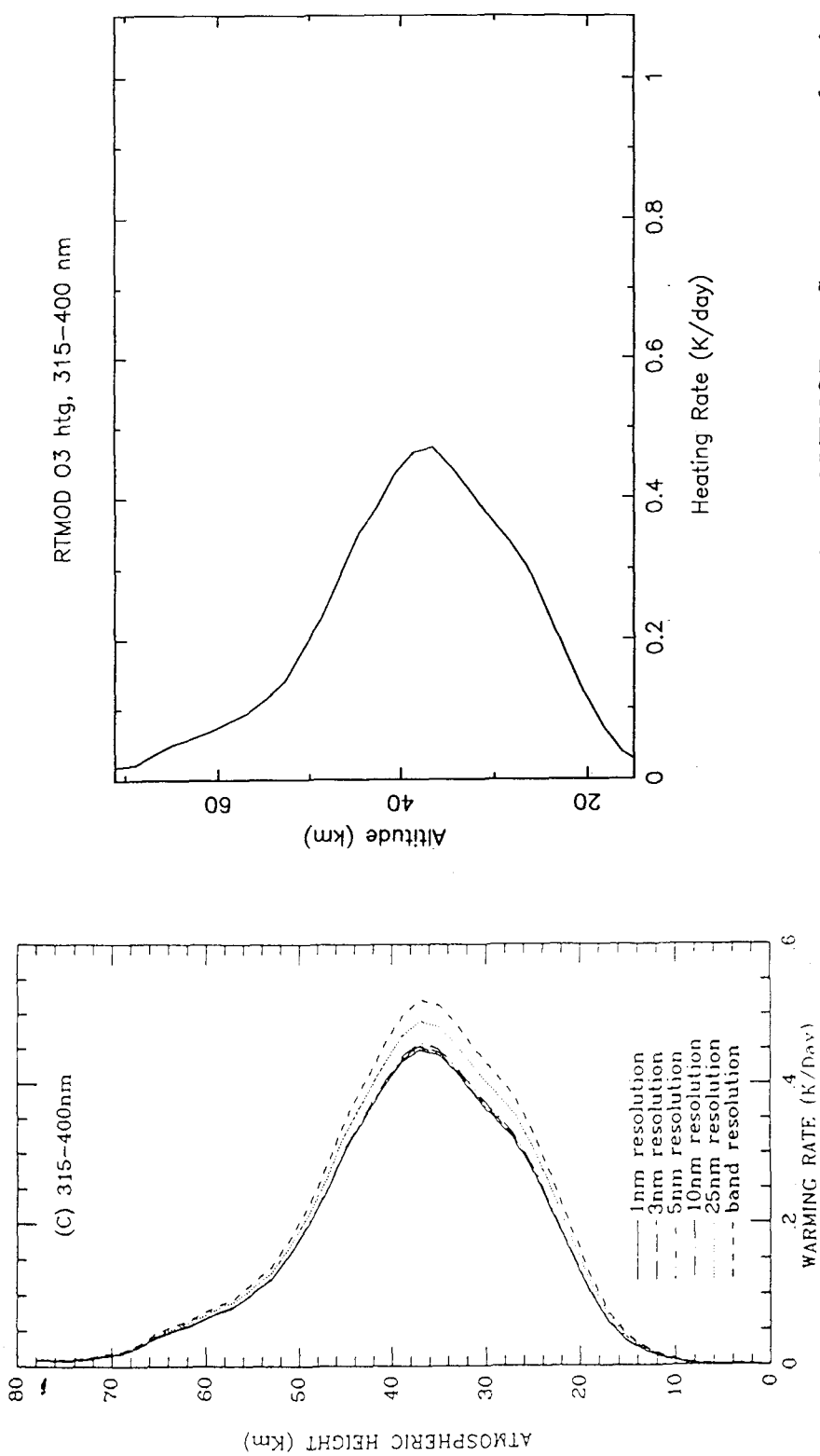

Fig. 3 Comparison of RTMOD vs. Stamnes ozone heating in the 315-400 nm band. See caption of Fig. 2.

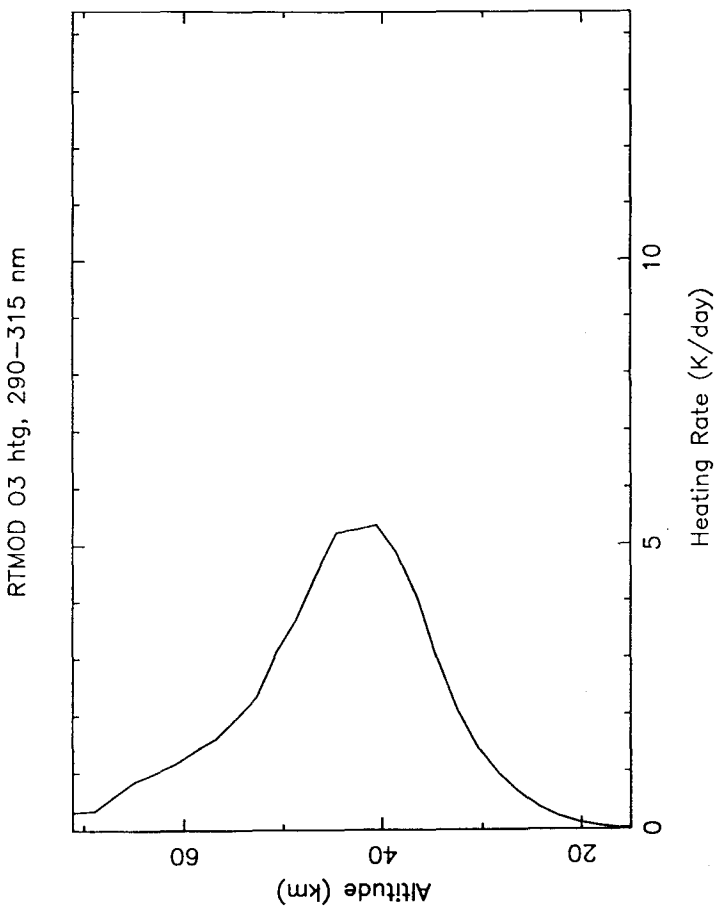

Fig. 4 Comparison of RTMOD vs. Stamnes ozone heating in the 290-315 nm band. See caption of Fig. 2.

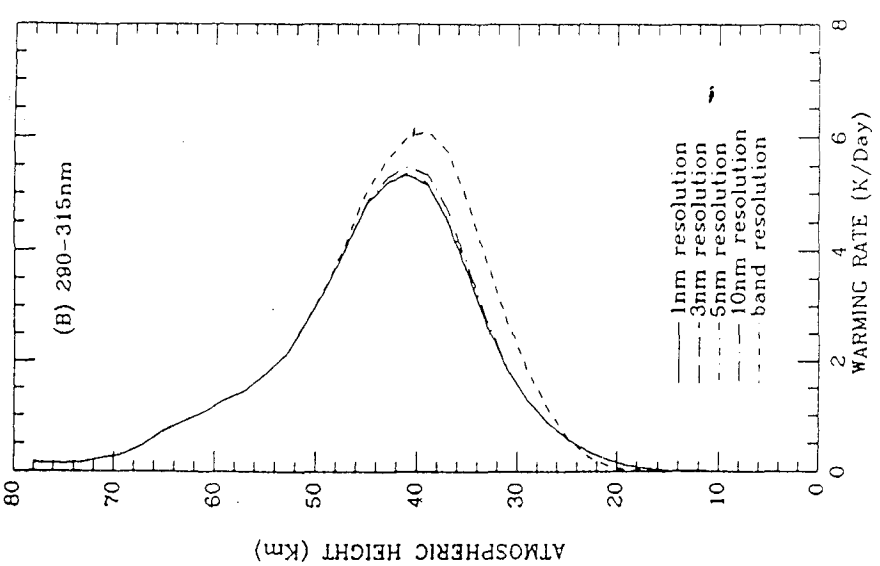

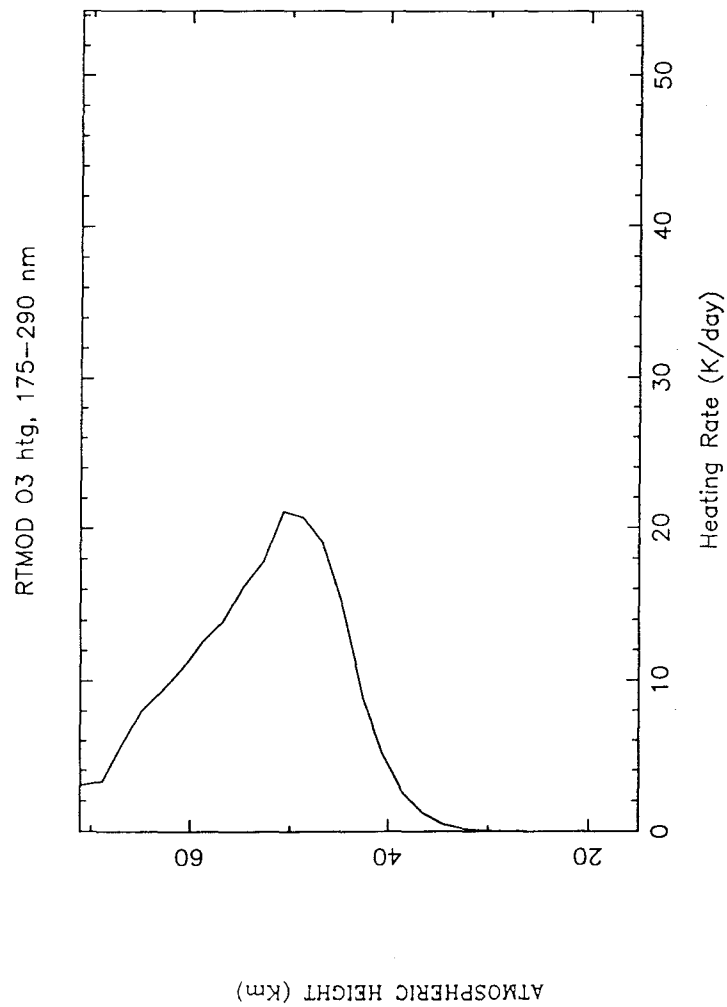

Fig. 5 Comparison of RTMOD vs. Stamnes ozone heating in the 175-290 nm band. Discrepancy consistent with the difference between JPL and WMO cross-sections.

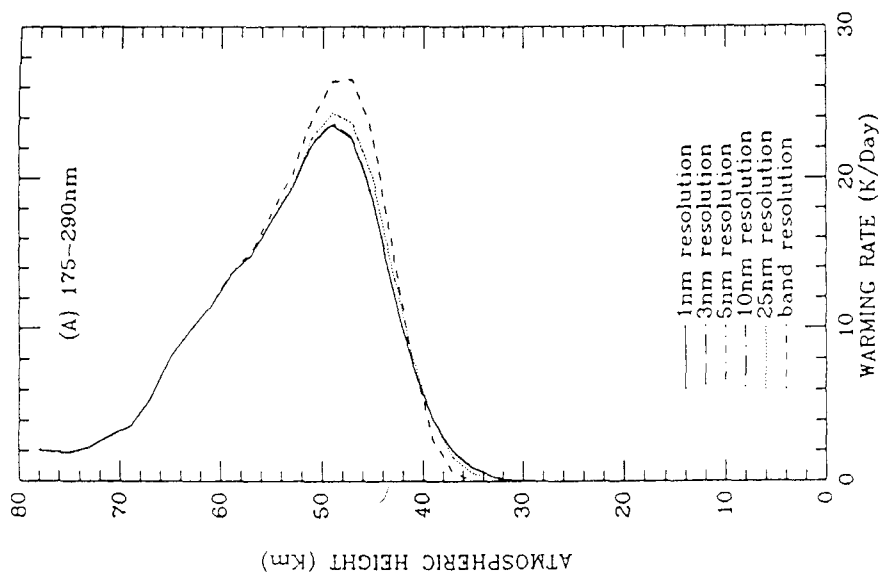

absorptions. In the RTMOD calculations of Figs. 2–5, the ozone profile, temperature profile, Rayleigh scattering, surface albedo, solar spectrum, and single solar zenith angle of 55° are those specified by St&Ts. No clouds are included, nor any gases other than ozone, except radiatively inactive pressure sources.

If ozone heating *per se* were not at fault, the next most obvious error source for the lower stratosphere would be the diurnal averaging algorithm, or some other aspect of the astronomy. Although UW and RTMOD were calculating the same declination for January 15, the UW code does its diurnal averaging of solar heating using only two solar zenith angles, commented as noon and midnight inside the code. For 85°S these were 65.124° and 72.188° (obviously not noon and midnight, which would differ by 10.00°; nevertheless they are centered on an appropriate value). To simulate UW's diurnal averaging process, and to find the resulting error in net heating, the average of two RTMOD results for these two SZA's was compared against an RTMOD diurnal average done with eight Gaussian longitudes, our usual number. Fig. 6 shows the error in solar heating arising from the two-angle method. For convenience, this particular test covered the UV and visible only, rather than the full solar spectrum, but undoubtedly it *is* part of the answer to the RTMOD/UW discrepancy, in which RTMOD always reports the larger heating. The two-angle error is negative throughout the stratosphere, -1% to -2% in the altitude range of greatest interest. The agreement at the top of the modeled atmosphere is consistent with the idea that both Olaguer and Crisp treat the obliquity and eccentricity correctly.

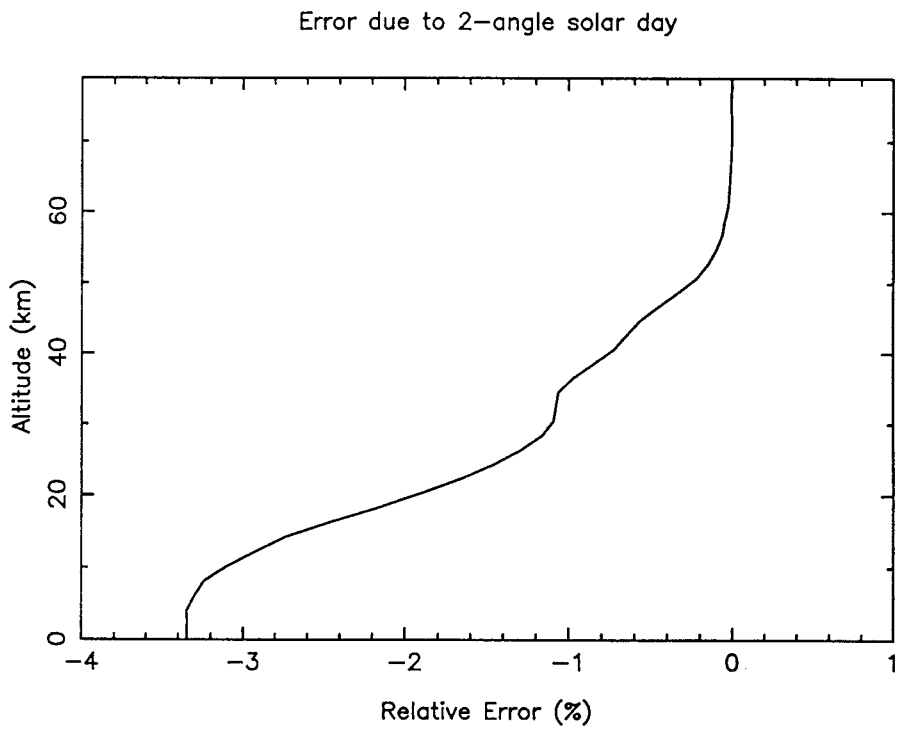

Fig. 6 Error introduced in UW's visible-UV heating rate by use of two-angle approximation of the sun's diurnal cycle at 85°S in mid-January, vs. RTMOD's eight-angle calculation. Agreement at top of atmosphere suggests both programs handle astronomical parameters correctly.

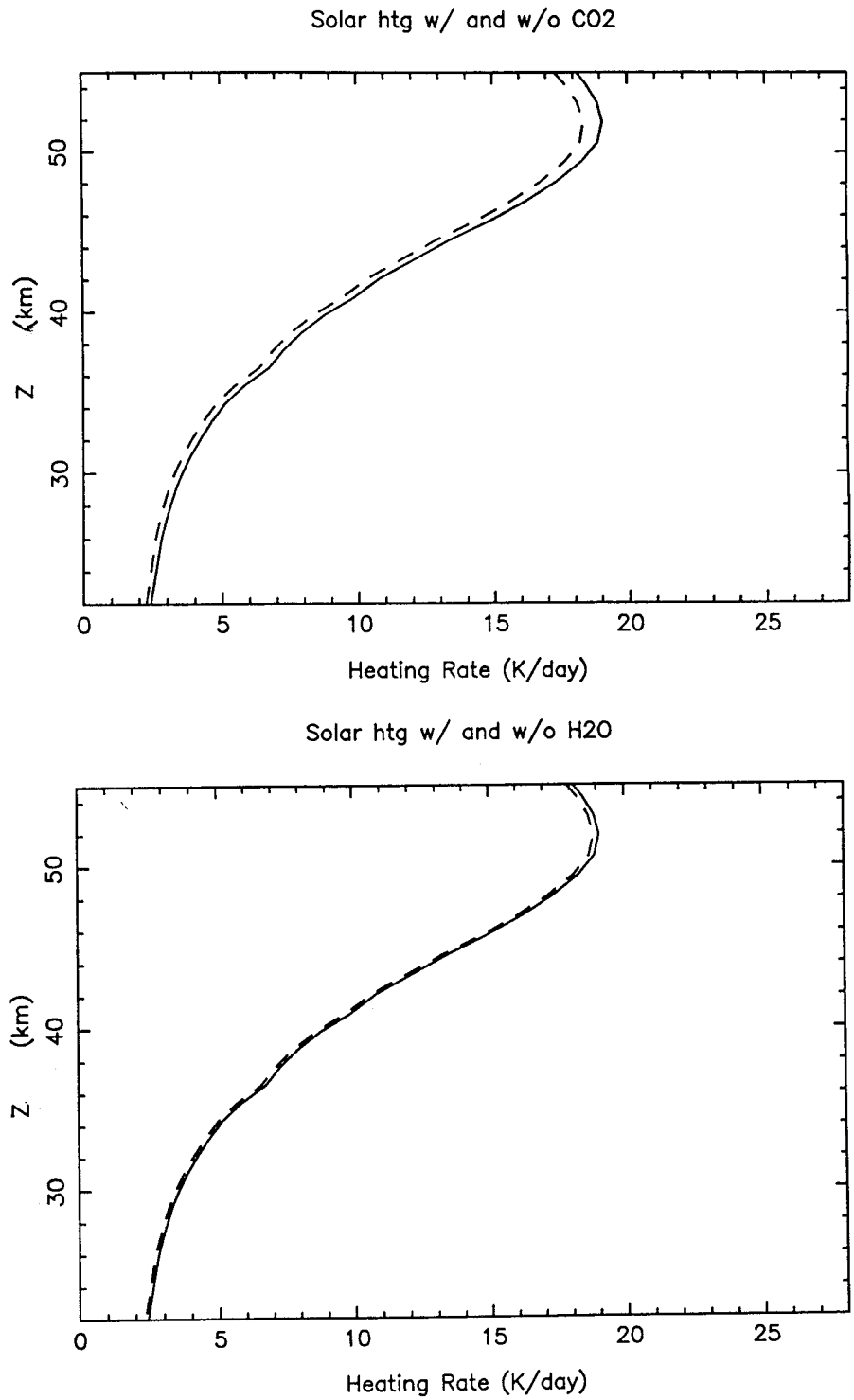

Fig. 7 Above: Solar heating profiles for 85°S with 330 ppm CO_2 (solid) and 0.0 CO_2 (dashes). Below: Solar heating profiles for 85°S with climatological H_2O (solid) and 0.0 H_2O (dashes). The two solid curves are identical, as both include the heating of H_2O, CO_2, O_3, O_2, and NO_2.

The remaining discrepancies in solar heating between the two models were several times larger, at many altitudes, than the thermal cooling errors of Fig. 0. Furthermore, most solar heating is photolytic, hence easy to calculate correctly (Figs. 2–4). In the middle atmosphere, whatever solar heating is not photolytic is due mainly to CO_2 emissions in the NIR. For a January, 85°S case, Fig. 7a shows solar heating with and without CO_2. The CO_2 heating is only 3–6% of the solar heating in the 20–60 km range, not enough to account for the discrepancy even if UW didn't include CO_2 absorption at all. Fig. 7b is analogous to Fig. 7a, but for water. During related experiments, Drs. Crisp and Eluszkiewicz discovered and corrected a bug in RTMOD's combination of ozone photolysis with weak water lines. The figures in GCC, in the boundary conditions note, and in this appendix were executed with the corrected program, in which solar radiative heating of the stratosphere is quite insensitive to the usual stratospheric water concentrations.

Some other effects that were considered during the search for the discrepancy are mentioned below. The UW model fails to photolyze CO_2. This turns out to be an $O(10^{-7})$ error in the stratosphere, suggesting that we might profitably run RTMOD without CO_2 photolysis...but the profit might be even smaller than the error. The UW model calculates the first derivative, with respect to pressure, of the ozone infrared absorbance, by using the Curtis-Godson approximation. According to Goody and Yung (1989), ozone is the least likely candidate for Curtis-Godson approximations, with 10% errors in ozone cooling rates to be expected; but this had no possible relevance to the discrepancy in solar heating rates. The strongest NIR band of ozone at 2110.79 cm^{-1} has about 1% the strength of the nearby CO_2 band at 2349.15 cm^{-1}, not to mention the difference in the concentrations of

these two species. The UW model calculates Voigt widths according to an approximation of Rodgers and Williams (1974), which can introduce almost 8% error under some conditions, while RTMOD uses a more time-consuming Voigt algorithm of Humlicek (1982) whose errors are on the order of 10^{-4}. Again, this could not help account for the RTMOD/UW discrepancy, for the error of the Rodgers and Williams approximation is always positive, whereas RTMOD's solar heating exceeded UW's in all known cases, until RTMOD was repaired.

Improvement of either RTMOD or our assumed climatology is still needed, since preliminary experiments have suggested we are not achieving a very good approximation of radiative equilibrium in the stratosphere. The magnitude of the horizontally averaged net heating rate (which should be zero) seems to be typically 7% of the magnitude of the geographical maximum net heating rate at any given altitude.

A full comparison of the corrected RTMOD and the Olaguer model will involve a wide collaboration and may be published eventually.

References

DeMore, W.B., D.M. Golden, R.F. Hampson, M.J. Kurylo, C.J. Howard, A.R. Ravishankara, C.E. Kolb, and M.J. Molina, 1992: Chemical kinetics and photochemical data for use in stratospheric modeling. *JPL Publication 92-20*, Jet Propulsion Laboratory, Pasadena, CA, 185 pp.

Eluszkiewicz, J., D. Crisp, L. Elson, E. Fishbein, L. Froidevaux, J. Waters, and R.

Zurek, 1994: Residual circulation in the stratosphere and lower mesosphere as diagnosed from Microwave Limb Sounder data. Submitted to *J. Atmos. Sci.*

Gerstell, M. F., J. Crisp and D. Crisp (1994), Radiative forcing of the stratosphere by SO_2 gas, silicate ash, and H_2SO_4 aerosols, shortly after the 1982 eruptions of El Chichon. To appear in *J. Climate* **8**.

Goody, R.M. and Y.L. Yung, 1989: *Atmospheric Radiation*, chap. 4. New York, Oxford Univ. Press, 519 pp.

Ridgway, W.L., Harshvardhan, and A. Arking, 1991: *J. Geophys. Res.* **96**, 8969. Permission to reproduce this figure in a new scientific paper or book is ceded under a blanket permission that appears inside the front cover of every issue of *JGR*.

Rodgers, C.D. and A.P. Williams, 1974: Integrated absorption of a spectral line with the Voigt profile. *J. Quant. Spectrosc. & Rad. Transfer* **14**, 319.

Stamnes, K. and S.-C. Tsay, 1990: Optimum spectral resolution for calculating atmospheric and photodissociation rates. *Planet. Space Sci.* **38**, 807–820. Figures reprinted with kind permission from Elsevier Science Ltd., The Boulevard, Langford Lane, Kidlington 0X5 IGB, UK.

West, R.A., D. Crisp and L. Chen, 1990: *J. Quant. Spectrosc. & Rad. Transfer* **43**, 191.

Yang, H., E. Olaguer, and K.K. Tung (1991): Simulation of the present-day ozone, odd nitrogen, chlorine, and other species using a coupled 2-D model in isentropic coordinates. *J. Atmos. Sci.* **48**, 442–471.

Paper IV: Testing the Porcupine Plate Hypothesis

M. F. Gerstell and J. M. Stock

Abstract. The Porcupine Plate, postulated in 1986 to explain difficulties in reconstructing anomalies 21 and 24 in the North Atlantic, is re-examined. Focusing sharply on the spreading segments nearest to Charlie-Gibbs Fracture Zone casts doubt on the Porcupine Plate hypothesis.

Introduction

The present study examines a hypothesis of Srivastava and Tapscott (1986; hereinafter S&T), who proposed the existence of a small plate southwest of the British Isles during the Eocene. They called it the Porcupine Plate. If this plate existed, it would be an unusual and interesting example of plate break-up near a divergent boundary, with no ridge propagation or major trench nearby.

In the context of an effort to describe the kinematic history of all plates in the North Atlantic region, S&T proposed that the Porcupine Plate (Figure 1) moved northwestward, relative to its northern neighbor, the Eurasian Plate, from anomaly 25 time (59 Ma B.P.) until anomaly 13 time (36 Ma B.P.); see Kent and Gradstein (1986). The motivation for S&T's proposition was that the rotations derived for the region north of the Charlie

Gibbs Fracture Zone (CGFZ), if applied to the region south of the CGFZ but north of King's Trough, caused anomalies 21 and 24 to move beyond closure, creating an overlap of the North American and Eurasian plates. However, they found an adequate fit for the next younger anomaly they considered – anomaly 13. Assuming that anomalies 21 and 24 had been correctly identified, and taking account of the spreading between Greenland and North America that occurred during the Eocene, they proposed that a short-lived Porcupine Plate on the European side of the Mid-Atlantic Ridge, and south of CGFZ, could account for the misfits of anomalies 21 and 24. A later study by Roest and Srivastava (1991), focusing on the tectonics of Iberia, mentions the Porcupine plate in passing, but appears to treat it as part of the Eurasian plate, and also moves its southern boundary northward from King's Trough, cutting off about 20% of the plate along its southern boundary. Further recent papers by these authors and others revive the Porcupine Plate as a separate entity; see Muller and Roest (1992) and its references. All papers cited here have a wider scope, so none gives detailed documentation of the case for or against the Porcupine Plate. Since the concept persists in the literature, it seems worth confirming or refuting.

While admiring the achievement of S&T in their presentation of a solution for the history of the entire North Atlantic, we adopt the view that the data most likely to resolve the Porcupine Plate question are those in the immediate vicinity of Charlie-Gibbs Fracture Zone (52°N), which was its northern boundary, and the one motivating its invention. In particular, we restrict our western data to the North American Plate, using no data from the Greenland Plate during the period of its independent motion. By focusing mainly on a

narrow band of sea-floor between 44°N and 56°N, we present evidence that anomaly 21 fits well without a boundary at CGFZ. We further propose that any motion along the eastern branch of CGFZ during the early Eocene may have had a very different sense from that proposed by S&T, and that the observed misfits need not be localized at Charlie-Gibbs.

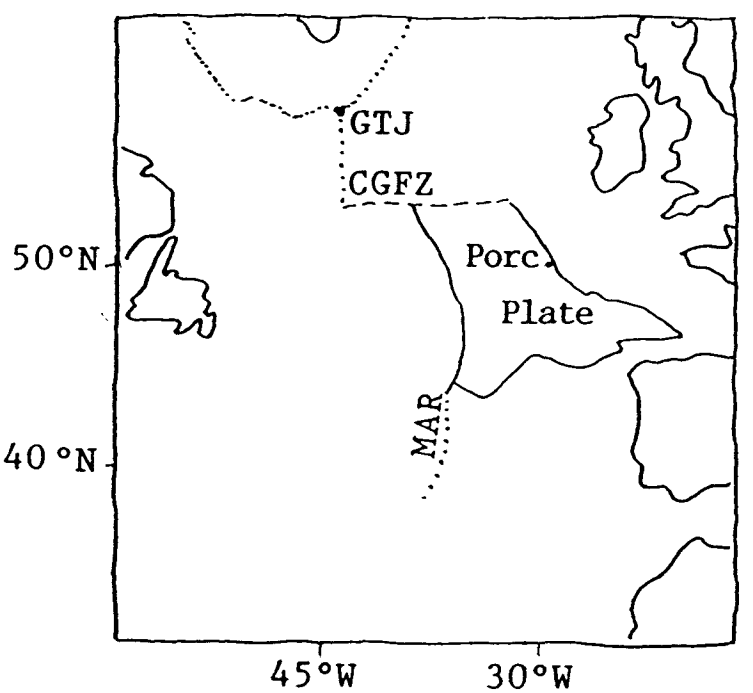

Fig. 1. The Porcupine Plate at anomaly 21 time, in the North American reference frame. After Srivastava and Tapscott (1986). GTZ: Greenland Triple Junction; MAR: Mid-Atlantic Ridge; CGFZ: Charlie-Gibbs Fracture Zone.

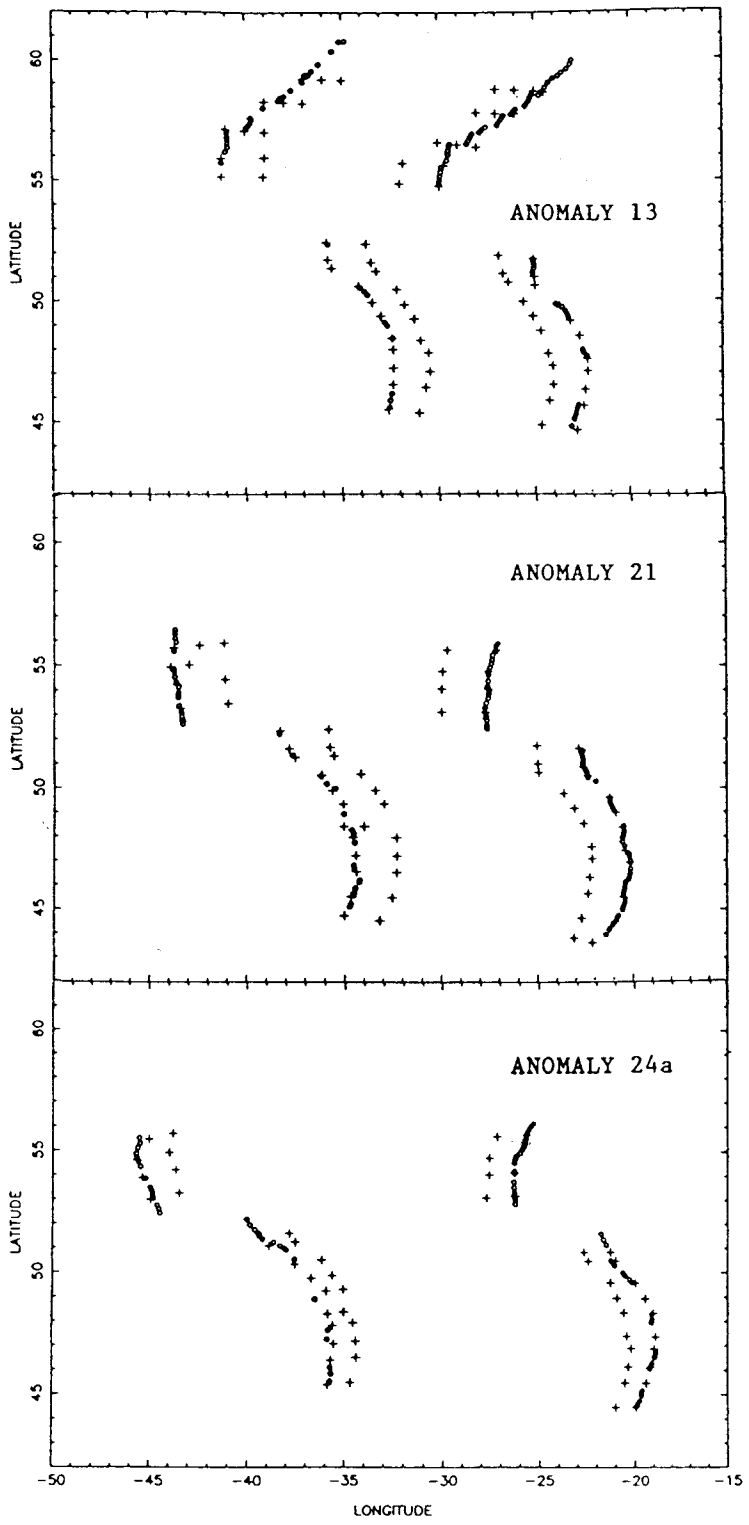

Fig. 2 Magnetic lineation points (circles) and fracture-zone data points (crosses) used in the present study.

Overview of Theoretical Method

Several investigations during the past 15 years proposed parameterizing the uncertainties in tectonic reconstructions derived from marine magnetic data (Pilger, 1978; Hellinger, 1981; Stock and Molnar, 1983; Jurdy and Stefanick, 1987; Richardson and Cole, 1991). A statistically rigorous definition of confidence intervals for finite rotations was given by Chang (1988) and further described by Chang, Stock and Molnar (1990). Hereinafter, these two papers are referenced as C88 and CSM.

The reconstruction method of Hellinger (1981; hereinafter, H81) involves finding the best-fitting great circle segments for each magnetic lineation and each fracture zone. Although the fracture zones are actually segments of small circles, they are so short that the difference between the ideal great-circle and small-circle segments is negligible. The best-fitting rotation is then found by requiring that each segment lie on the same great circle as its mate from the opposite plate, and minimizing the sum of the squares of the distances of observed points from their ideal great circles. In this latter calculation, the distances are weighted by the reciprocals of the estimated standard errors of the observed points.

Occasional absurdities can arise from this approach. For example, a pair of nearly-parallel magnetic stripes is most likely to be due to a small-angle rotation around a pole roughly 90° away. But Chang's implementation of the H81 method sometimes gives a 180° rotation around a pole in the center of the data set. This can be a "good" fit because there is no requirement that the points on corresponding magnetic lineation segments should

rotate to positions near one another – only that the great circles defined by corresponding segments should coincide after the rotation. When spreading is slow and segment offsets are small, as in the Atlantic, one occasionally obtains the statistically best fit by completely inverting one stripe or the other. This species of spurious fit can always be avoided by including at least some fracture-zone data.

Absolute changes in apparent positions of finite-rotation poles do not appropriately describe stability, from the point of view of CSM. Apparent errors in the poles are systematically large when the rotation magnitudes are small, and vice versa. To see this, one need only consider a rotation of zero magnitude, for which the location of the pole is entirely undefined. The best parameterization of uncertainties involves considering how a perturbing rotation affects the sum-of-squares misfit. Starting from this concept, and assuming that the observed data points follow a Fisher-Bingham distribution (Kent, 1982) about the corresponding points on the ideal great circles, C88 and CSM give a precise algorithm for constructing a 3D confidence region around the pole and rotation magnitude.

Richardson and Cole (1991) claim greater generality than previous investigators of the uncertainties in plate reconstructions. However we propose that their method lacks the generality of C88 in one crucial respect. Richardson and Cole allow the uncertainties of individual data points to follow any radially symmetric probability density function, but the radial symmetry itself is an unwarranted assumption when positions along linear tracks (magnetic anomalies and fracture zones) are being reported. The Fisher-Bingham distribution suggested in C88 is the analogue, for a spherical surface, of the bivariate normal distribution in the plane, so that along-track and across-track errors can be estimated

separately. Advantages of C88 over the earlier methods of estimating uncertainties are expounded in C88.

Data and Procedures

Data used in the present study are illustrated in Figure 2. These data were obtained from Woods Hole Oceanographic Institution, where they had been processed in a manner partially described by Klitgord and Schouten (1986) and Vogt (1986), and their chronology determined by Kent and Gradstein (1986). Some new fracture zone data were added at WHOI subsequent to the cited publications, but the magnetic data were unchanged. Our reason for restricting anomaly 24a and anomaly 21 data to a narrow band north of CGFZ in the present study is to avoid any points that were on the Greenland Plate while it was moving relative to North America. This motion is generally agreed to have stopped by anomaly 19 time. For example, see S&T (1986). For anomaly 13, the band was expanded slightly, because available data for the North American lineation were too sparse in the latitudes immediately north of CGFZ. The anomaly 13 data north of CGFZ are therefore associated with Reykjanes Ridge, but selected from the southernmost segments of adequate data density.

All rotations were derived from Chang's implementation of H81, and all error ellipsoids from C88.

A difficulty that arose in selecting fracture-zone positions suitable for processing by the methods of H81 and C88 is that even in this relatively well-mapped region, our sparse

data precluded choosing more than one fracture-zone point lying within the small offset between a pair of adjacent segments of a magnetic lineation. Constructing and matching the great circles along which the fracture-zone points are assumed to lie requires at least two fracture-zone points on at least one of the two plates, and one point on the matching fracture zone from the opposite plate. Therefore the direction of motion must be defined by including fracture zone points that are removed from the magnetic lineation of interest by a hundred kilometers or more, which in the case at hand corresponds to an age difference of about ten million years. However, this difficulty is not peculiar to the method of H81; many reconstruction methods using fracture-zone data involve a similar problem.

Some of the fits in the present study were refined after excluding all fracture-zone data. Where fracture-zone data were used, each fracture zone was represented by at least four points: one quite close to each branch of the particular magnetic anomaly under consideration, and the next nearest available fracture-zone point on the younger side of each branch. The younger side was selected in preference to the older side because the fit between any one pair of anomalies is relevant only to their subsequent history. Fracture zones used in this study were traceable all the way from the western to the eastern branch of whichever magnetic anomaly was being considered. It was assumed that uncertainties in the positions of fracture-zone points were twice as large as the uncertainties in the positions of magnetic-anomaly points. Except as otherwise noted, estimates of absolute uncertainties in the data were adjusted upward or downward, while keeping relative uncertainties the same, until the $\hat{\kappa}$ parameter of C88 lay between 0.95 and 1.05; when this outcome was achieved the error ellipsoids were assumed correct. The $\hat{\kappa}$ parameter is the ratio of estimated uncertainties

to true uncertainties.

Newer fracture-zone data are in circulation, such as those of Sandwell and Ruiz (1992) or Muller and Roest (1992). Visual comparison indicates our data are generally consistent with these. In any case, the constraints provided by fracture-zone data in the present study are weak compared to those provided by magnetic data. This is appropriate since magnetic data motivated for the Porcupine Plate hypothesis.

The final versions of the fits in Figure 3 did not involve any fracture-zone data.

Results

A statistically acceptable fit ($\hat{\kappa} \approx 1$) was found for all the points on magnetic anomaly 21 in Figure 2, with only a 4-km estimate of uncertainties in the data points, if fracture zone data were ignored. The same was true of anomaly 13. The reconstructions are illustrated in Figure 3, in the reference frame of North America. Total rotations for these reconstructions were (for A21) 9.74° around a pole at 50.82° S, 35.94° W, and (for A13) 6.96° around a pole at 56.42° S, 38.89° W. Had an equally satisfactory fit been found for anomaly 24, we would reject out of hand the hypothesis of an Eocene plate boundary along the eastern branch of Charlie-Gibbs Fracture Zone. Since the misfit of anomaly 24a was inescapable, further details were explored with the working hypo- thesis that such a boundary may have existed.

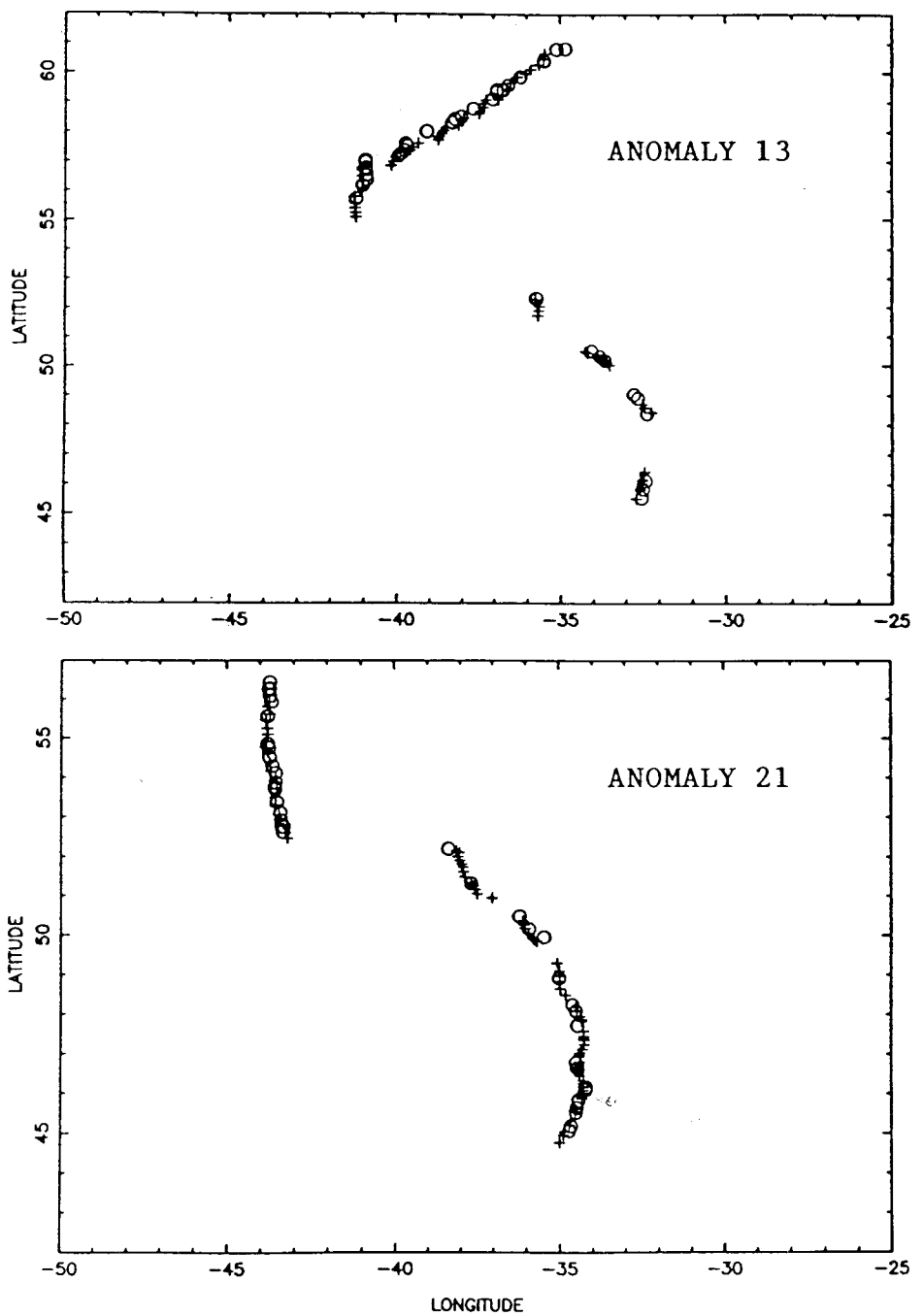

Fig. 3 Magnetic lineation data from the Eurasian plate (crosses) have been rotated onto North American magnetic lineations (circles). Best-fitting rotations were derived by considering magnetic data from both north and south of Charlie-Gibbs Fracture Zone.

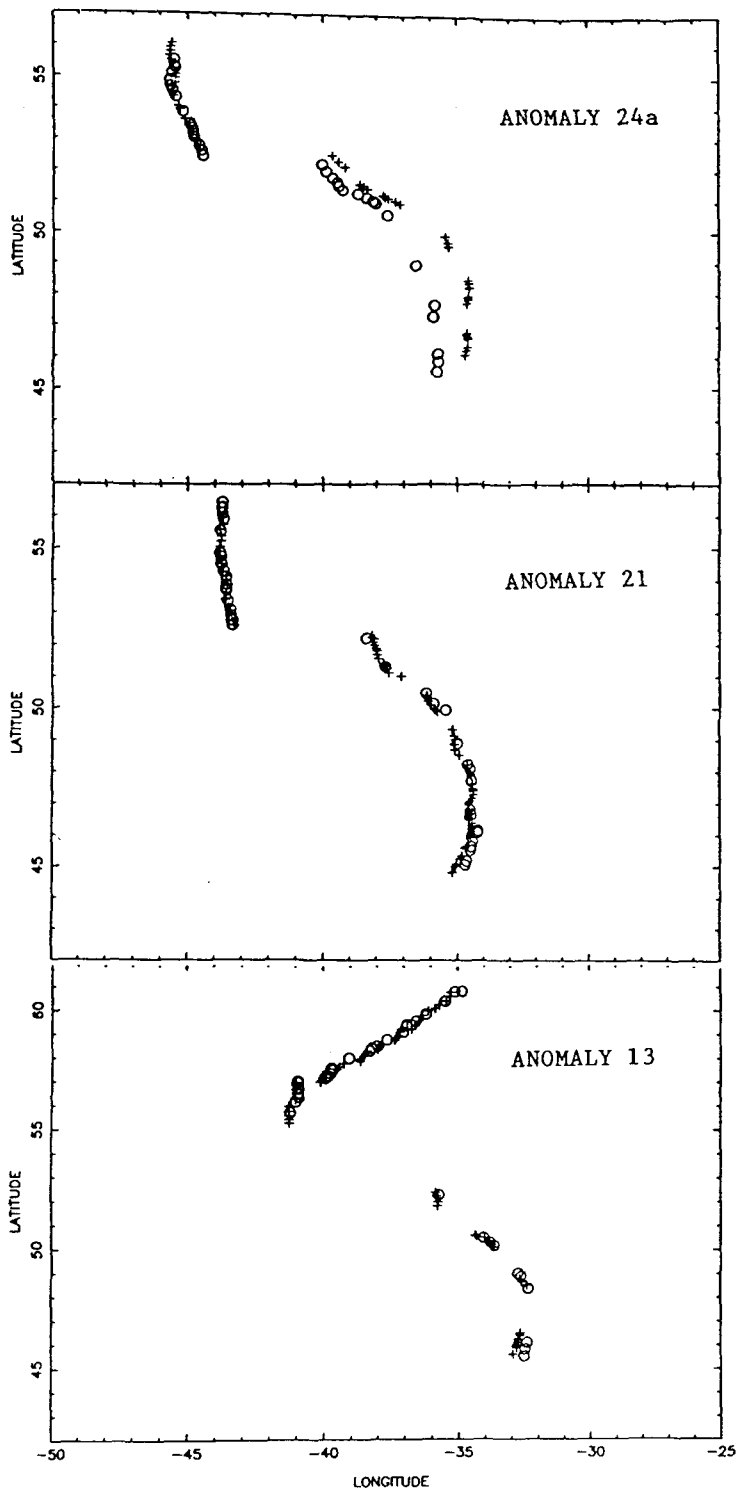

Fig. 4 The rotations applied to the Eurasian data were calculated in this case using only the data from north of Charlie Gibbs Fracture Zone. Symbols as in Figure 3.

In Figure 4, each of anomalies 24a, 21, and 13 has been subjected to the best-fitting rotation derived from the northern data only (both magnetic lineations and fracture zones), and it is plain that the southern "Porcupine" data are systematically misfit. Crosses are points from the Eurasian side, circles on the American side. In the case of anomaly 24, the sense of the misfit is opposite to that reported by S&T; rather than rotating too far, the points south of CGFZ are not rotated far enough. This indicates that any net motion of the Porcupine Plate relative to Eurasia after A24 time should have been left-lateral, not right-lateral as implied by S&T.

The misfit of anomaly 24a, in contrast to the better fit of anomaly 21, almost certainly means that something occurred between anomaly 24 time and anomaly 21 time to distort the existing record of anomaly 24a. The Porcupine Plate hypothesis as given by S&T is not consistent with the present study, because it implies the misfit should be in the opposite direction. The most obvious difference between North Atlantic tectonics of the early Eocene and those of modern times is that Greenland was separating from North America. Recall that the spreading segments under consideration here were limited with the intention of minimizing Greenland's possible influence. The western lineations in the A21 and A24a experiments are definitely on the North American Plate, not the Greenland Plate. However, a plausible alternate interpretation for the obvious misfit of anomaly 24a is that the North American lineation in the latitudes immediately above CGFZ was distorted by the eastward motion of Greenland during the A24-A21 interval. Some support for this idea comes from Figure 5, where one sees that the "fit" of anomaly 24a onto anomaly 21 is slightly worse for the northwest quadrant than for the other three quadrants.

The slight misfit of anomaly 21 is indeed in the direction described by S&T, but it will be shown that this effect, if real, can be partly attributed to motions that occurred after the time of anomaly 13. Furthermore, the misfit of anomaly 13 cannot be localized at Charlie-Gibbs Fracture Zone. The best-fitting pole for the motion of the Reykjanes portion of A13 meanders irregularly away from the best-fitting "Porcupine" pole as more northerly data sets are selected for the Reykjanes part of A13. These further experiments are not shown, but they suggest a distributed deformation in the region north of CGFZ. Argus et al (1989) concluded that any present-day Eurasian oceanic microplates are moving much more slowly than the 4-7 mm/yr motion of Africa relative to Eurasia, but the deformation imagined here has also been much slower than that, averaged over the 36-Ma age of anomaly 13, so it may possibly persist.

In Table I, numbers in the first column are derived from the work of S&T by summing various rotations they give for the Porcupine and Eurasian Plates relative to North America. Numbers in the second column were obtained in the present study, by the methods of C88, and include the effects of all data points shown in Figure 2. The 95% confidence ellipsoids for the Porcupine/North America motions and Eurasia/North America motions were disjoint in this experiment, but for A13 and A21, could be made to overlap by omitting some data points. It can be seen that the earliest motions (A24a to A21) deduced in the present study have a sense nearly opposite to the motions deduced by S&T for the same period. Motions in the A21 to A13 period are right-lateral in both columns, but transtensive in the present study, in contrast with the transpression implied by S&T. The resemblance of our A13 rotation to their A21 and A24 rotations is admittedly not so

striking geometrically as numerically; both our pole and theirs are close to the data, so the direction of motion is somewhat different. But the resemblance supports our earlier claim that the overlap of Porcupine and North American data in Figure 4(b), if meaningful, could be partly attributed to more recent motions.

Discussion

The strongest reason for challenging the Porcupine Plate hypothesis, as formulated by Srivastava and Tapscott, is the existence of a statistically acceptable fit for anomaly 21 with no boundary at Charlie-Gibbs Fracture Zone. A secondary reason is that the present study indicates that any net motion along the eastern branch of CGFZ during the early Eocene should have been in the opposite sense from the motion proposed by S&T. The differences between the present results and theirs are probably due to our excluding the data most likely to have been affected by motions of Greenland. Nevertheless, the remaining apparent discrepancy between rotations north and south of CGFZ could well be an artifact of the assumption that Greenland's motions have been eliminated, or of the assumption that the plates flanking Reykjanes Ridge have been rigid since the time of anomaly 13. S&T proposed, but discarded, two alternative explanations for the disparities that led them to invent the Porcupine Plate. One of these involved the Lomonosov Ridge in the Arctic. Although the present study does not include Labrador Sea data, it does seem likely that the problem of anomaly 21 and 24 overlaps, which motivated S&T's Porcupine Plate proposal, was a result of the circuit around Greenland rather than a local boundary at

CGFZ. The second alternative was the possibility of mistaken identification of anomalies, and we agree this alternative needs further investigation.

The numbers in Table I may or may not be consistent with basin-scale tectonics. They are intended only to suggest that the magnetic data within a few hundred km of Charlie-Gibbs Fracture Zone do not indicate a uniform right-lateral transpression there beginning with anomaly 25 and ending with anomaly 13.

Finally, there is no independent evidence for motion along S&T's proposed eastern boundary of the Porcupine Plate. Using their northwestward transpression of the Porcupine Plate towards CGFZ, the motion required on the eastern boundary would be right-lateral, and comparable in speed to the putative motion along Charlie-Gibbs Fracture Zone. No bathymetric signature is seen so close to the French coast. (One could be buried in sediments.) A notable basement high runs SSE from Charlie-Gibbs Fracture Zone for a few hundred kilometers, roughly along anomaly 24. See Olivet et al (1974), and Figure 6 herein. This structure appears east and west of the Mid-Atlantic Ridge, and is somewhat symmetric on the two sides of the ridge. The distance from the basement high to the ridge on the Eurasian or Porcupine side is smaller than on the American side, which would be consistent with the Porcupine Plate hypothesis but does not require it. The length of the basement high is virtually identical on both sides, which might militate against the Porcupine Plate hypothesis.

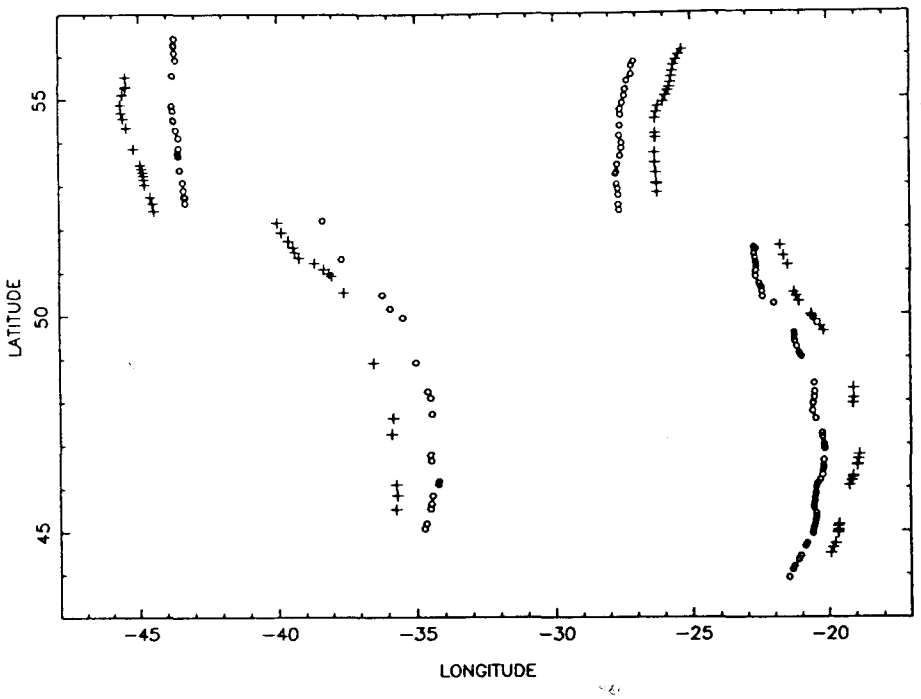

Fig. 5 The "fit" of anomaly 24a (crosses) onto anomaly 21 (circles) appears slightly worse north of Charlie-Gibbs Fracture Zone and west of the mid-Atlantic ridge than in the other three quadrants of the picture.

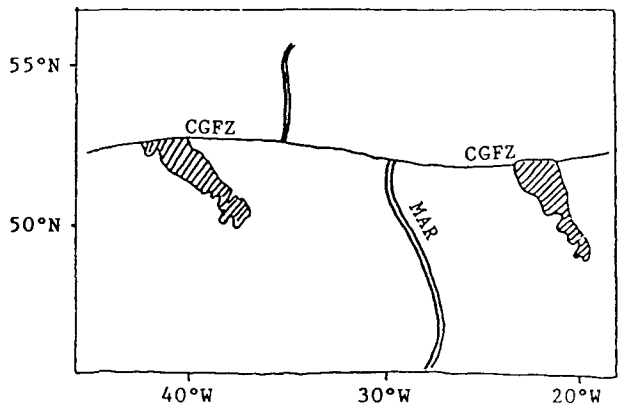

Fig. 6 The cross-hatched areas are basement highs. After Olivet *et al*, 1974.

Time Interval	Deduced from Srivastava and Tapscott (1986)			This study, methods of Chang (1988)		
	Lat.	Long.	Angle	Lat.	Long.	Angle
A0 –A13			0.00	51.85	–19.64	1.65
A0 –A21	59.93	–10.07	1.15	59.36	–23.91	2.13
A0 –A24	59.94	–10.02	1.80	54.45	–24.31	–5.56
A13–A21	59.93	–10.07	1.15	78.82	–73.60	0.54
A21–A24	59.95	–9.95	0.65	55.80	–24.09	–7.67

Positive angles are counterclockwise, and time runs from present to past.

TABLE I

Computed poles of motion of the Porcupine Plate relative to the Eurasian Plate

Muller and Roest (1992) regard the morphology of Charlie-Gibbs Fracture Zone as evidence in favor of its status as a former plate boundary. They point out changes in CGFZ's structure, east of 27° W. Since anomaly 21 intersects CGFZ near 27° W, their argument is more consistent with the results of the present study than with the Porcupine Plate hypothesis as originally formulated.

In conclusion, it is doubtful that Charlie-Gibbs Fracture Zone was a plate boundary after the time of anomaly 21. If it was a plate boundary before that, the sense of the motion localized there remains highly uncertain.

Acknowledgements

This study was undertaken while the first author was supported by NASA Fellowship NTG-30016. We are grateful to Kim Klitgord for making the data available; to Ted Chang advice on the use of his software, and to two anonymous referees for their comments.

References

Argus, D. F., Gordon, R. G., DeMets, C. and Stein, S., 1989. Closure of the Africa-Eurasia-North America plate motion circuit and tectonics of the Gloria fault, *J. Geophys. Res.* **94**, 5585–5602.

Chang, T., 1988. Estimating the relative motion of two tectonic plates from boundary crossings, *J. Am. Stat. Assn.* **83**, 1178–1183.

Chang, T., Stock, J. M. and Molnar, P., 1990. The rotation group in plate tectonics

and uncertainties of plate reconstructions, *Geophys. J. Int.* **101**, 649–661.

Hellinger, S. J., 1981. The uncertainties of finite rotations in plate tectonics, *J. Geophys. Res.* **86**, 9312–9318.

Jurdy, D. M. and Stefanick, M., 1987. Errors in plate rotations as described by covariance matrices and their combination in reconstructions. *J. Geophys. Res.* **92**, 6310–6318.

Kent, D. V. and Gradstein, F. M., 1986. A Jurassic to recent chronology, in P. R. Vogt and B. E. Tucholke (eds.), *Geology of North America, Vol.* M, 45–50 (Geological Society of America, Boulder, Colorado, 1986).

Kent, J. T., 1982. The Fisher-Bingham distribution on the sphere. *J. Roy. Stat. Soc.* **44**, 71–80.

Klitgord, K. D. and Schouten, H., 1986. Plate kinematics of the central Atlantic, in P. R. Vogt and B. E. Tucholke (eds.), *Geology of North America, Vol.* M, 351–378 (Geological Society of America, Boulder, Colorado, 1986).

Muller, R. D. and Roest, W. R., 1992. Fracture zones in the North Atlantic from combined Geosat and Seasat data, *J. Geophys. Res.* **97**, 3337–3350.

Olivet, J. L., LePichon, X., Monti, S. and Sichler, B., 1974. Charlie Gibbs Fracture Zone, *J. Geophys. Res.* **79**, 2059–2079.

Pilger, R. H., 1978. A method for finite plate reconstructions with applications to Pacific-Nazca plate evolution, *Geophys. Res. Lett.* **5**, 469–472.

Richardson, R. M. and Cole, G. L., 1991. Plate reconstruction uncertainties using empirical probability density functions, *J. Geophys. Res.* **96**, 10391–10400.

Roest, W. R. and Srivastava, S. P., 1991. Kinematics of the plate boundaries between Eurasia, Iberia, and Africa in the North Atlantic from the late Cretaceous to the present, *Geology* **19**, 613–616.

Sandwell, D. T. and Ruiz, M. B., 1992. Along-track gravity anomalies from Geosat and Seasat altimetry, *Marine Geophys. Res.* **14**, 165–205.

Srivastava, S. P. and Tapscott, C. R., 1986. Plate kinematics of the north Atlantic, in P. R. Vogt and B. E. Tucholke (eds.), *Geology of North America, Vol.* **M**, 379–404 (Geological Society of America, Boulder, Colorado, 1986).

Stock, J. M. and Molnar, P., 1983. Some geometrical aspects of uncertainties in combined plate reconstructions, *Geology* **11**, 697–701.

Vogt, P. R., 1986. Magnetic anomalies and crustal magnetization, in P. R. Vogt and B. E. Tucholke (eds.), *Geology of North America, Vol.* **M**, 229–256 (Geological Society of America, Boulder, Colorado, 1986).